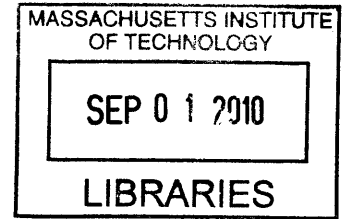# A System Dynamics Approach to User Independence in High Speed Atomic Force Microscopy

by

Daniel J. Burns

B.S., Mechanical Engineering (2001)
Arizona State University

S.M., Mechanical Engineering (2004)
Massachusetts Institute of Technology

Submitted to the Department of Mechanical Engineering
in partial fulfillment of the requirements for the degree of

Doctor of Philosophy in Mechanical Engineering

at the

MASSACHUSETTS INSTITUTE OF TECHNOLOGY

May 2010
[June 2010]

Author . . . .
Department of Mechanical Engineering
May 15, 2010

Certified by . . . .
Kamal Youcef-Toumi
Professor of Mechanical Engineering
Thesis Supervisor

Accepted by . . . .
David E. Hardt
Chairman, Department Committee on Graduate Students

A System Dynamics Approach to User Independence in High Speed Atomic Force Microscopy

by

Daniel J. Burns

Abstract

As progress in molecular biology and nanotechnology continues, demand for rapid and high quality image acquisition has increased to the point where the limitations of atomic force microscopes (AFM) become impediments to further discovery. Many biological processes of interest occur on time scales faster than the observation capability of conventional AFMs, which are typically limited to imaging rates on the order of minutes. Imaging at faster scan rates excite resonances in the mechanical scanner that can distort the image, thereby preventing higher speed imaging. Although traditional robust feedforward controllers and input shaping have proven effective at minimizing the influence of scanner distortions, the lack of direct measurement and use of model-based controllers has required disassembling the microscope to access lateral motion with external sensors in order to perform a full system identification experiment, which places excessive demands on routine microscope operators.

This work represents a new way to characterize the lateral scanner dynamics without addition of lateral sensors, and shape the commanded input signals in such a way that disturbing dynamics are not excited in an automatic and user-independent manner. Scanner coupling between the lateral and out-of-plane directions is exploited and used to build a minimal model of the scanner that is also sufficient to describe the source of the disturbances. This model informs the design of an online input shaper used to suppress components of the high speed command signals. The method presented is distinct from alternate approaches in that neither an information-complete system identification experiment, nor microscope modification are required. This approach has enabled an increase in the scan rates of unmodified commercial AFMs from 1-4 lines/second to over 100 lines/second and has been successfully applied to a custom-built high speed AFM, unlocking scan rates of over 1,600 lines/second. Images from this high speed AFM have been taken at more than 10 frames/second.

Additionally, bulky optical components for sensing cantilever deflection and low bandwidth actuators constrain the AFM's potential observations, and the increasing instrument complexity requires operators skilled in optical alignment and controller tuning. Recent progress in MEMS fabrication has allowed the development of a new type of AFM cantilever with an integrated sensor and actuator. Such a fully instrumented cantilever enables direct measurement and actuation of the cantilever motion and interaction with the sample, eliminating the need for microscope operators to align the bulky optical components. This technology is expected to not only allow for high speed imaging but also the miniaturization

of AFMs and expand their use to new experimental environments. Based on the complexity of these integrated MEMS devices, a thorough understanding of their behavior and a specialized controls approach is needed to guide non-expert users in their operation and extract high performance. The intrinsic properties of such MEMS cantilevers are investigated, and a combined approach is developed for sensing and control, optimized for high speed detection and actuation.

Thesis Supervisor: Kamal Youcef-Toumi
Title: Professor of Mechanical Engineering

Acknowledgments

I would like to express my deep gratitude to my advisor, Professor Kamal Youcef-Toumi for his guidance, expertise, and patience. Kamal instilled in me the idea that academic research should be about the *exploration* of important ideas, and to reach beyond what I think is possible—that is where real progress is made.

I am also deeply indebted to the thesis committee members, Professors David Hardt and Krystyn Van Vliet. Their suggestions, support and encouragement helped make a difficult process enjoyable. I am convinced that this thesis is better for having them involved.

I would like to thank Georg Fantner for sharing his immense expertise and many insightful discussions, for help with the construction of the high speed AFM, for the loan of his instruments, and most of all, for his friendship.

This thesis would not have been possible without the help of very dedicated and selfless individuals at MIT. First, I would like to thank my collaborators on the high speed AFM: Vijay Shilpiekandula, Kwang Yong Lim, Iman Soltani Bozchalooi, Vencislav Todorov, Andreas Schuh and Wiebke Shumann. Our many detailed discussions helped clarify important notions. Second, I have also enjoyed mentoring Kimberly SooHoo and Samuel Kesner and this work has directly benefited from their contributions. Third, I would also like to express my appreciation to my colleagues in the Mechatronics Research Lab: Pablo Valdivia, Khalid El Rifai, Mauricio Gutierrez, Xu Zhiguang, Sang-il Lee, Dimitrios Chatzigeorgiou and the hilarious Adam Wahab. Interactions with them have made my time in the lab a pleasure.

MIT has a wonderful tradition among the support staff of putting the needs of the students first. I cannot imagine my time here without the helpful and caring Leslie Regan, Joan Kravit, and Dick Fenner. Administrative tasks have always gone smoothly thanks to David Rodriguera and Marie Pommet.

I have met many lifelong friends during my tenure here, including Tom Bowers, Devin McCombie, Dariusz Golda, Alec Robertson, James Evans, Eric Wade, Manas Menon, Craig Forest, Kevin Duda, John Mills and Angry Dave Quinn. It makes all the difference to have friends who have struggled with and overcome the same difficulties I faced, and who are always ready to split a pitcher of beer.

I would also like to acknowledge all those who, in their own ways, provided me with

Contents

List of Figures

List of Tables

Chapter 1

Introduction

The resolving power and versatility of the atomic force microscope (AFM) has established it as an essential tool for nanotechnology, biological studies and semiconductor process characterization. Its unique ability to image nanoscale features in air, vacuum or liquid, and on conductive or insulating samples, makes the AFM often the only instrument capable of certain observation modalities. Its precision force detection capability merged with functionalization of the force probe has opened new fields of study (*i.e.*, molecular force spectroscopy, magnetic force microscopy, and topography and recognition imaging) and new and exciting uses of the AFM continue to produce dramatic results.

However, the primary disadvantage in AFM continues to be the limited speed at which images can be obtained. Scan speeds fundamentally limit most observations to static or quasi-static samples, which restrict the scientific observations that can be made. Many biological processes of interest occur on time scales faster than the observation capability of conventional AFMs, which are typically limited to imaging rates on the order of minutes. The thesis contributions here are aimed at addressing the speed limitations of AFM, and doing so in a way that reduces to the demands of the researcher or microscope operator.

1.1 AFM Description

1.1.1 Brief History of AFM Technology

Although its origins can be traced back to the scanning profilometers of 1929 [92], the invention of the atomic force microscope (AFM) is commonly attributed to Binnig and Quate in 1986 [9]. The AFM was developed as a response to the shortcomings of scanning tunneling microscopes (STM) for which Binnig and Rohrer shared the 1986 Nobel Prize in Physics [10]—the main shortcoming being that the STM requires samples that are electrically conductive and imaged in vacuum. Their first AFM demonstrated atomic scale images on a ceramic (insulating) sample (AL_2O_3) [9]. Interestingly, this first instrument measured deflection of a diamond-tipped gold foil cantilever using tunneling current from an existing STM current probe. Later developments used interferometry to measure cantilever deflection before settling on the optical lever detection method that uses a laser and photodiode.

1.1.2 Theory of Operation

An atomic force microscope has three main components as shown in Figure 1-1. The piezoelectric tube actuator is fixed at the bottom to the frame of the microscope and the top end is free and allows three-dimensional motion of the sample relative to the probe. The tube is quartered axially into four sections to allow for the bending that provides the displacement in the x- and y-directions, and an additional full cylindrical section of the tube provides z extension. Amplifiers provide the high voltage necessary to actuate the piezo tube. The sample is placed on the free end of the tube. Above the sample, a flexible cantilever is mounted to a small piezo stack actuator for oscillating the cantilever near its resonance (or one of its harmonics in advanced imaging modes). The end of the cantilever is fabricated with a sharp probe, which interacts with the sample and causes the cantilever to deflect. This deflection is measured by a laser and photosensitive diode.

The topography image is generated based on how the tube is commanded to extend in the vertical direction, z, in order to hold some property of the cantilever constant (commonly static deflection for so-called *contact mode*, and either RMS oscillation amplitude or phase
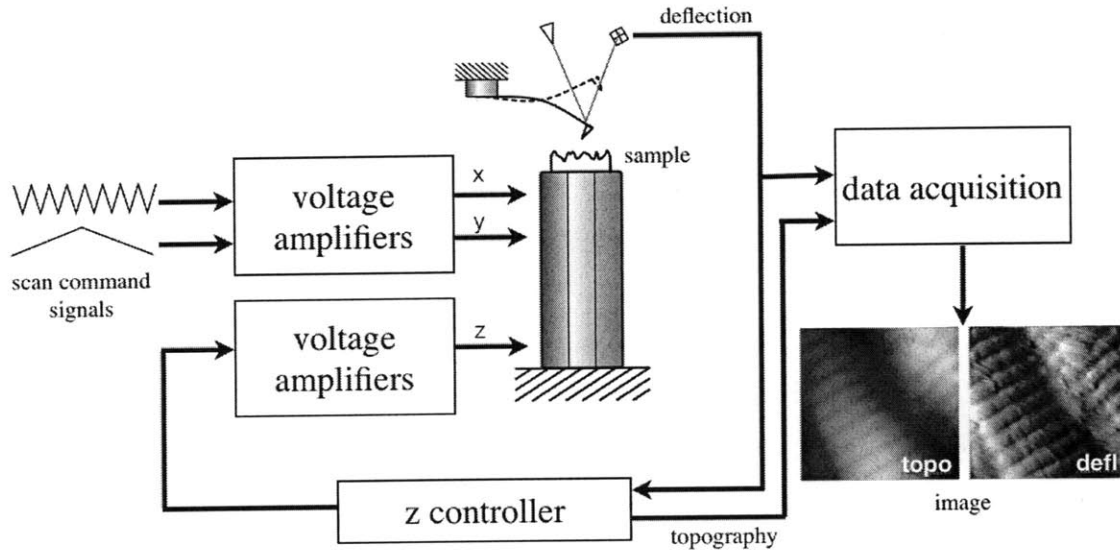
Figure 1-1: A. The principle components of a conventional scanned-sample atomic force microscope, consisting of (i) a piezo tube scanner, (ii) MEMS cantilever and optical lever detector, (iii) data acquisition system and (iv) feedback controller to regulate the tube extension. Triangular-shaped command signals are applied to the scanner in an open-loop fashion to achieve raster scanning.

relative to the tapping piezo excitation signal in *intermittent contact mode*). And often the error signal in that feedback loop, e, is also plotted in order to capture high spatial frequencies (sample details measured by the probe but not tracked by the feedback system). The images generated are $z(x,y)$ and $e(x,y)$ where $x(t)$ and $y(t)$ are the triangular scan command signals, which assumes that the piezo tube actuator follows those trajectories.

1.1.3 Optical Lever Detection

The core enabling technology that popularized the AFM is the mechanical cantilever that deflects due to interaction forces with the sample, and due to its critical role in AFM operation, special attention regarding the measurement of its deflection is required. As mentioned previously, initial AFM designs detect the cantilever deflection using the tunneling current between the conductive cantilever and a current probe, and later was replaced with optical interferometry. Ultimately, a much simpler approach was developed using a laser source reflected from the cantilever to photodetector (see Figure 1-1). This method is referred to as *optical lever detection*, and simple ray tracing indicates that the sensitive deflection mea-

surement is enabled by a double-angle amplification stemming from rotating the reflecting element. In other words, cantilever deflection causes a rotation at the free end of θ and this results in a change in the departing ray of 2θ. And with the photodetector located several centimeters away from the cantilever, deflections at the free end of the cantilever of less than a nanometer are amplified by the optical path and result in laser spot motion of several millimeters. Using this basic optical measurement technique, a wide variety of AFM studies have demonstrated the ability to measure topography with atomic resolution [68], ascertain the locations of single molecules [42], or characterize electrical [70], mechanical [94] or magnetic [70] material properties.

While this method has yielded precise measurements of the cantilever and in turn, the characterization of atomic interaction forces, the use of this optical lever detection method can be cumbersome and restrictive. As will be discussed, higher bandwidth imaging requires cantilevers with smaller physical dimensions, which demands more tightly focused and more precisely aligned optics. The cumbersome optics in conventional microscopes become increasingly difficult to manage when high speed applications require small cantilevers. Additionally, the laser and photodiode are bulky components that increase the physical size of the AFM. Elimination of the optical components will lead to reduced workloads by microscope users, and enable new operating scenarios for AFM, for example, as in disposable chemical sensors for clinical applications or for AFM imaging on Mars [2, 44, 43]—an otherwise untenable scenario if optical alignment is required.

The shortcomings of optical detection have long been recognized, and other researchers have examined alternate approaches. Quate et.al. at Stanford University has been pursuing batch fabricated self-sensed and self-actuated cantilevers for some time. Early work considered patterning piezoelectric actuators directly onto cantilevers in an effort to circumvent the slow piezo tube actuator [74, 73], and multi-cantilever arrays have been explored for parallel imaging [1, 3]. When coupled with nanomanipulation, a parallel arrangement of cantilever arrays that omit optical detection in favor of self-sensing is proposed for storing data in polymers by tip-localized heating and subsequent deformation sensing [95]. Elimination of the optical deflection sensing has enabled new innovation in AFM development that benefits high speed imaging while relieving the user of the management of optical elements.

1.2 The Need for High Speed Imaging

As progress in molecular biology and nanotechnology continues, demand for rapid and high quality image acquisition has increased to the point where the limitations of AFM imaging become impediments to further discovery [17, 18]. Many biological processes of interest occur on time scales faster than the imaging capability of conventional AFMs [5, 96], which are typically limited to image acquisition rates on the order of minutes [22]. Increasing the imaging rates of commercial AFMs enables new experimental observations, which in turn can lead to new discovery [36]. The ability to operate the AFM at higher rates without loss of image quality will facilitate new experimental scenarios including studying dynamical changes of material properties on a surface [52], the action of biological molecules [7, 4], or facilitate metrology studies for high volume manufacturing by reducing time to find a feature [35, 73].

Many exciting new discoveries in biology will be enabled by high speed AFM imaging. For example, recent work has focued on using components of high speed AFM to measure protein-protein interactions in real time [96]. Viani *et al.* demonstrated a prototype small cantilever AFM head to characterize the binding and dissociating of single molecules of *e. coli* GroES and GroEL proteins. Other studies of *e. coli* used conventional AFM to examine the time-dependent nature of antibiotic action during the killing phase. The antibiotics were diluted, and the *e. coli* were immobilized to accommodate the slow nature of AFM imaging [36]. Other work has focused on imaging the folding of proteins in real time, to better understand conformational diseases such as Alzheimer's, Huntington's and Parkinson's diseases [81]. Imaging protein conformation progression is key to designing effective treatment of these diseases, and while current generation AFMs can provide sufficient resolution for these studies, it operates too slowly to observe conformation changes in real time.

The demand for increased imaging bandwidth has long been acknowledged, and several research groups have worked to address the speed limitations of AFM, and selected results are summarized in the next section.[1]

---

[1]Note that several chapters in this thesis are written as standalone journal articles, and therefore have more detailed background and summaries of the state of the art in those chapters.

A.   B.
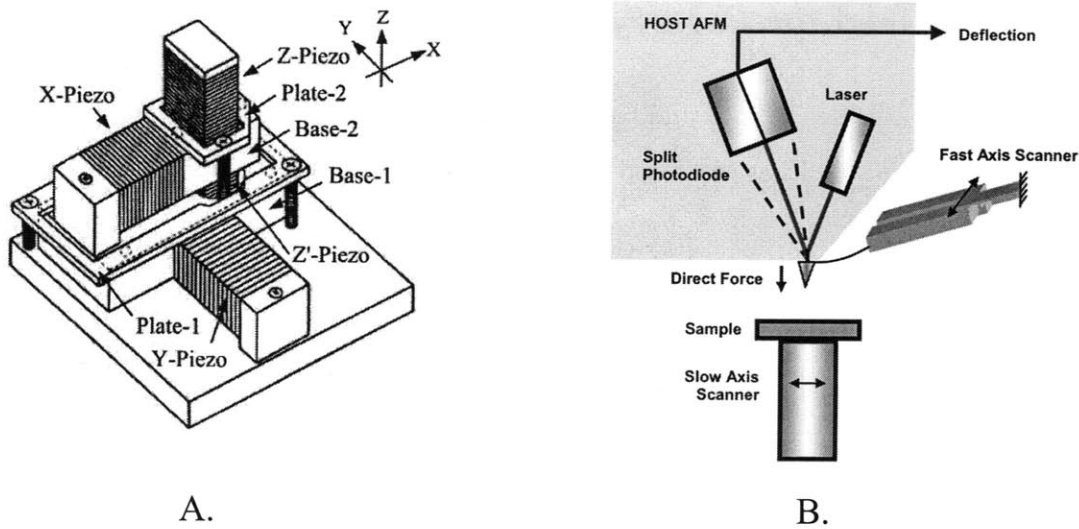
Figure 1-2: Existing approaches to high speed AFM. A. The high speed scanner developed by Ando, *et al.* has a very high first resonant frequency (60 kHz) and images at a line rate of 1.25 kHz. The imaging range of this AFM is limited to a few hundred nanometers [5]. B. Another approach to high speed AFM comes from Humphris *et al.*, and places a cantilever on a tuning fork for scanning at the fork's resonant frequency [49]. Here, a conventional piezo tube scanner is used for both the slow scan axis, and the z-axis topography tracking, although topography is not strictly tracked during a scan (most of the sample information is in the deflection signal).

1.3   State of the Art

The imaging rate limitation of conventional AFMs has been recognized for some time and several research groups have made progress toward high speed operation. One suggestion proposed by Manalis *et al.* is to add an actuator to the cantilever to provide small scale tip deflection and therefore relieve the piezo tube of low amplitude, high frequency adjustments [67]. This advancement allows the imaging bandwidth to be increased from 0.6 to 6 kHz. While this improvement enables higher topography tracking bandwidth, the scanning subsystem is not addressed. Further, the high voltage required to deflect these cantilevers preclude their use in liquid environments or on surfaces susceptible to strong electric fields like semiconductor wafers and photomasks.

More recently, several research groups have considered a bandwidth-motivated redesign of the AFM's actuation system. Researchers in Japan created a three-axis nested linear stage whereby the x and z-axis scanners are positioned by the y-axis scanner, and the

z-axis scanner is positioned by the x-axis scanner (see Figure 1-2A) [5]. Both x and y translation axes are guided by ball bearings. By eliminating the conventional piezoelectric tube actuator, the scanner's first resonnace was increased to 60 kHz for small scan areas (less than 250×250 nm^2), which allowed the system to study biologically active macromolecules in real time [4, 55]. In this nested design, bandwidth is limited by the inertia of the upper stages, and only simple feedback strategies such as PID control and active damping are employed [57]. However, the primary disadvantage of this approach is the limited range of the scanner.

Another approach comes from Humphris *et al.* [49], wherein the fast scan axis of the cantilever is achieved with a separate tuning fork actuator. The slow scan axis and topography tracking is still performed with a conventional piezo tube actuator (see Figure 1-2B). As will be covered in Section 2.3, a constant velocity scanner achieves the highest quality imaging in the shortest time. The sinusoidal scanning characteristic of resonance scanners, such as those based on tuning forks, forgoes constant velocity scanning, and their proponents argue that its primary benefit is the avoidance of excitation of detrimental vibrations. A scanner that achieves higher scanning velocity than the tuning fork method, while still exhibiting the preferred constant velocity scan, is presented in Chapter 5. This achievement is enabled with the use of an online system identification procedure and subsequent model-based controller applied to the lateral axes and described in Chapter 4. Further, the Humphris approach does not attempt to track topography with a z axis feedback controller. This approach, known as *constant height mode*, uses only the cantilever deflection to recreate the topography. In this mode of operation, the interaction force between the cantilever and the sample varies over the image area, and for certain samples (especially biological specimens), this uncontrolled interaction force could exceed levels that result in sample damage or cell rupture.

Finally, it should be noted that the high speed AFM described in Chapter 5 is an extension of the work by Hansma, *et al.* [38, 46, 37, 87, 53], with the present work providing improvements to the scanner and application of the indirect system ID and resonance compensator (see Chapter 4), which results in an additional order-of-magnitude scan speed increase. Here, the x and y piezo stacks are arranged in a perpendicular fashion in a plane

and position a central support disk. A counterbalanced z piezo stack is mounted on a frame on the support disk, and the central structure is further supported by an additional inner frame flexure to minimize vibration and increase stiffness in the vertical direction. This mechanical deign, when coupled with the automatic system identification and compensation of the lateral dynamics, is capable of recording 8 frames per second over a 512×128 pixel area using 14 bits per channel [37]. This high speed AFM constructed as part of this work has a much larger range than the Ando system, and does not suffer from the sinusoidal scanning or lack of topography tracking disadvantages of the Humphris system. Although lateral dynamics of this scanner previously limited its speed and ease of use, the work presented in Chapter 4 and Chapter 5 mitigates these issues, and enables scan rates as high as 1000 lines/second, over scan volumes of 15 $\mu m \times$ 15 $\mu m \times$ 4 μm.

1.4 Proposed Approach

In both conventional tube scanners and experimental flexure scanners, imaging at faster scan rates excite resonances that can distort the image, thereby preventing higher speed imaging. Although traditional robust feedforward controllers and input shaping have proven effective at minimizing the influence of scanner distortions, the lack of direct measurement and use of model-based controllers has required disassembling the microscope to access lateral motion with external sensors in order to perform a full system identification experiment, which places excessive demands on routine microscope operators.

This work represents a new way to characterize the lateral scanner dynamics without addition of lateral sensors, and shape the commanded input signals in such a way that disturbing dynamics are not excited in an automatic and user-independent manner. The method presented is distinct from alternate approaches in that neither an information-complete system identification experiment, nor microscope modification are required.

Resonances are excited when operating piezo tube scanners at higher speed, and ultimately distort the image. A novel algorithm is derived that extracts information about the lateral scanner dynamics from the deflection signal. In this manner, the ultimate metric of observation quality, the image, is used to judge whether lateral resonances are large

enough to corrupt the observation, and if so, a method is described to extract sufficient parameters to identify the scanner dynamics and design a compensator. This compensator successfully increases the imaging bandwidth of conventional AFMs from 1 line/second to 40 lines/second. This approach has the important feature of enabling a just-in-time scanner characterization that circumvents the previously required tradeoff between compensator performance and robustness to scanner dynamics variation—the performance benefits of an aggressive compensator are realized without the susceptibility to parameter variation. This ability to immediately identify the scanner dynamics can be done automatically and without modification to most commercial microscopes, providing a user-independent path to rapid imaging for most of the 15,000 AFMs installed worldwide. Further, this method is shown to be robust to even the most challenging topographies where sample periodicity could be mistaken for scanner artifacts. Recognizing that the scanner resonance is excited even at slow speeds, and using the time between scan lines to acquire information about the scanner dynamics, a strategy to separate spatial features from scanner resonances is described.

This automatic scanner identification and compensation approach has enabled an increase in the scan rates of unmodified commercial AFMs from 1-4 lines/second to over 100 lines/second and has been successfully applied to a custom-built high speed AFM, unlocking scan rates of over 1,600 lines/second. Images from this high speed AFM have been taken at more than 8 frames/second.

Additionally, bulky optical components for sensing cantilever deflection and low bandwidth actuators constrain the AFM's potential observations, and the increasing instrument complexity requires operators skilled in optical alignment and controller tuning. Recent progress in MEMS fabrication has allowed the development of a new type of AFM cantilever with an integrated sensor and actuator. Such a fully instrumented cantilever enables direct measurement and actuation of the cantilever motion and interaction with the sample, eliminating the need for microscope operators to align the bulky optical components. This technology is expected to not only allow for high speed imaging but also the miniaturization of AFMs and expand their use to new experimental environments. Based on the complexity of these integrated MEMS devices, a thorough understanding of their behavior and a specialized controls approach is needed to guide non-expert users in their operation and extract

high performance. The intrinsic properties of such MEMS cantilevers are investigated, and a combined approach is developed for sensing and control, optimized for high speed detection and actuation. The ultimate aim of this effort is improving the tracking bandwidth and understanding and eliminating potential obstacles to routine use with, for example, a half-frequency drive system that avoids undesirable low frequencyhigh frequency actuator coupling. These new cantilevers promise to eliminate many auxiliary components of the AFM infrastructure, including the (often slow) z actuator used for topography tracking, and the cumbersome optics assembly.

1.5   Document Layout

The thesis contributions here are aimed at addressing the speed limitations of AFMs, and doing so in a way that reduces the demands of the researcher or microscope operator. Toward that end, an effort is made to understand the fundamental limitations of scanning speed in Chapter 2. Using insight gained from the analysis, research is conducted on two primary bottlenecks in high speed operation: cantilevers and scanners. Work presented in Chapter 3 details a thorough characterization of a new kind of active cantilever that integrates actuation and sensing, with the ultimate aim of improving their bandwidth and understanding and eliminating potential obstacles to their routine use.

Chapter 4 describes resonances that are excited when operating piezo tube scanners at higher speed, and presents a novel algorithm that extracts information about the lateral scanner dynamics from the deflection signal. This method is shown to automatically correct for the limitations of tube scanners with no involvement from the microscope operator or modification to the AFM.

In Chapter 5, a prototype high speed AFM is designed and constructed by examining each of the main components in the system and replacing them with high speed versions. The resonance identification and compensation algorithm from Chapter 4 is applied, and the resulting instrument is shown to image at 8 frames/second.

Finally, concluding remarks and suggestions for future work are provided in Chapter 6.

Chapter 2

Analysis of Scan Speed Limitations

This chapter describes the effects and parameters that limit the scan rate in atomic force microscopy. First, contact mode imaging is modeled and limits are derived on the scan speed. It is shown that scan speed is limited by the mass of the cantilever and the damping coefficient, indicating that small cantilevers and higher damping leads in increased scan speeds. Second, tapping mode is analyzed and it is shown that while a large Q factor of the oscillating cantilever leads to good imaging sensitivity, it also impedes scan speed, and therefore a balance in the Q factor must be achieved. Finally, the scanning subsystem of AFMs is examined in order to understand how the current limitation of piezo tube scanners can be avoided with a redesigned component based on mechanical flexures.

2.1 Contact Mode Scan Speed Limitations

In this section, equations are derived that set limits on the scanning speed in contact mode AFM. Broadly, the purpose of the model is to understand the parameters that limit scan speed under the detectability constraint of a compliant sample with bounded spatial periods. The analysis that follows is based on [20].

In order to understand the parameters that limit contact mode imaging scan speed, a model is developed describing a cantilever interacting with a compliant sample. The sample is assumed to have surface stiffness k_s and whose topography $s(x)$ contains a sum of spatial frequencies
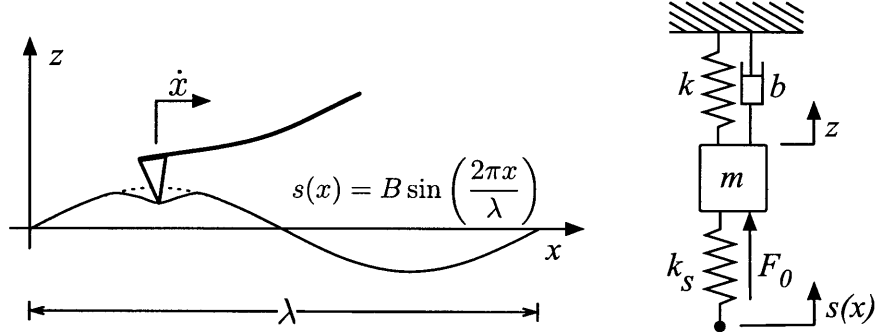
Figure 2-1: Model used to determine limits on scan speed in contact mode imaging. (Left) A cantilever with stiffness k and damping coefficient b deforms a compliant sample with highest spatial period λ and stiffness k_s. (Right) A lumped parameter model of the cantilever–sample interactions during imaging.

$$s(x) = \int_{-\infty}^{\infty} A(\nu)\cos(\nu x) + B(\nu)\sin(\nu x)dx. \tag{2.1}$$

To simplify the analysis, a single term is retained that represents the highest imaged spatial frequency (because all others provide less severe constraints on the dynamics and can be ignored) (see Figure 2-1).

$$s(x) = B\sin\left(\frac{2\pi x}{\lambda}\right) \tag{2.2}$$

A cantilever interacting with the compliant surface is governed by

$$m\ddot{z} = -b\dot{z} - kz - k_s z + k_s s(x) + F_0 \tag{2.3}$$

where m, b and k are the first modal mass, damping coefficient and stiffness of a lumped-parameter model, k_s is the sample stiffness, and F_0 is any external force acting on the cantilever that is not position dependent (van der Waals, adhesion, electrostatic, etc.). With Equation (2.2) the differential equation becomes,

$$m\ddot{z} + b\dot{z} + kz + k_s z - k_s \left(B\sin\left(\frac{2\pi x}{\lambda}\right)\right) = F_0. \tag{2.4}$$

Let the angular frequency be defined as $\omega = 2\pi\dot{x}/\lambda$, where $\dot{x}$ is the scan speed, and the

governing equation is finally

$$m\ddot{z} + b\dot{z} + (k + k_s)z = F_0 + k_s(B\sin(\omega t)) \tag{2.5}$$

Equation (2.5) is the equation for a damped harmonic oscillator with both constant and sinusoidal forcing, and has the general solution that is a sum of the transient response and the steady-state response

$$z(t) = ae^{(-\gamma t)}\sin(\omega_d + \phi) + \frac{F_0}{k + k_s} + c\sin(\omega t + \theta) \tag{2.6}$$

where a and ϕ are determined by the initial conditions, and the other parameters are given by

$$\gamma = \frac{b}{2m} \tag{2.7}$$

$$\omega_d = \sqrt{\omega^2 - \gamma^2} = \sqrt{\frac{k + k_s}{m} - \left(\frac{b}{2m}\right)^2} \tag{2.8}$$

$$c = \frac{k_s B/m}{\sqrt{\left(\frac{k+k_s}{m} - \omega^2\right)^2 + 4\gamma^2\omega^2}} = \frac{k_s B}{\sqrt{(k + k_s - m\omega^2)^2 + b^2\omega^2}} \tag{2.9}$$

$$\theta = \tan^{-1}\left(\frac{\frac{k+k_s}{m} - \omega^2}{2\gamma\omega}\right) = \tan^{-1}\left(\frac{b\omega}{k + k_s - m\omega^2}\right) \tag{2.10}$$

The second term in Equation (2.6), $F_0/(k+k_s)$, is the part of the response corresponding to equilibrium compression of the sample.

The first and third terms in Equation (2.6) provide two constraints on scan speed, the most stringent of which depends on the value of the damping coefficient as detailed in the following analysis.

The the first term in Equation (2.6) describes the influence of transients on the response of the cantilever. In order for sudden changes in topography or scan direction not to impact cantilever deflection (and therefore create imaging artifacts), the transient response must be negligible compared to the steady-state sinusoidal response. For this to be the case, the time to scan a feature $\lambda/\dot{x}$ must be much longer than the time constant in the exponential

$\gamma^{-1} = 2m/b$, or

$$\dot{x} \ll \frac{\lambda b}{2m} \tag{2.11}$$

The third term in Equation (2.6) describes the steady state motion of the cantilever tip to topographic spatial frequencies, and its parameters c and θ depend on ω. For low frequencies, the amplitude is given by $k_s B/(k + k_s)$ and the cantilever response z is proportional to topography B, which is important for imaging without artifacts. As ω is increased, c reaches a maximum at the peak frequency

$$\omega_p = \omega_n \sqrt{1 - 2\gamma^2/\omega_n^2} \tag{2.12}$$

$$= \sqrt{\frac{k + k_s}{m} - \frac{b^2}{2m^2}} \tag{2.13}$$

and above ω_p, B decreases and $\lim_{\omega \to \infty} B = 0$. For accurate and high quality imaging, it is assumed that the cantilever response should not depend on scan speed, and it must be proportional to the topography for imaging without artifacts. This is true when $\omega \ll \omega_p$, or

$$\dot{x} \ll \frac{\lambda}{2\pi} \sqrt{\frac{k + k_s}{m} - \frac{b^2}{2m^2}} \tag{2.14}$$

Therefore, we have that Equations (2.11) and (2.14) limit the scan speed, and the cantilever damping b determines which constraint is the most stringent. At the critical value for b

$$b_c = \frac{1}{\pi + 1/\sqrt{2}} \sqrt{m(k + k_s)} \tag{2.15}$$

the two constraints are equal. For $b < b_c$, Equation (2.11) sets the velocity constraint, whereas for $b > b_c$, Equation (2.14) limits the velocity, as summarized in Table 2.1.[1]

The essential consequence of the preceding analysis is that strict bounds can be placed on the scan speed of the cantilever relative to the sample in order to guarantee that spatial features are detectable by the cantilever deflection. (Whether cantilever detection is subsequently measured by the laser/photodiode and tracked by the z feedback controller and actuator is another matter outside the scope of the present analysis.) This section only con-

---

[1]Note that although Equation (2.14) suggest an infinite scan speed is possible for a perfectly rigid sample, this degenerate case will require a new cantilever model (*i.e.*, a fixed-supported, instead of a fixed-free beam model).

Table 2.1: Scan speed limits in contact mode imaging. Material properties of the cantilever and sample determine the fastest scan speed permitted such that topographic features with period λ are still measurable by the cantilever.

Low Damping $b < b_c$	$\dot{x} \ll \frac{\lambda b}{2m}$	(2.11)
High Damping $b > b_c$	$\dot{x} \ll \frac{\lambda}{2\pi} \sqrt{\frac{k+k_s}{m} - \frac{b^2}{2m^2}}$	(2.14)

siders the dynamics of the cantilever on scan speed in an effort to understand the theoretical limitations of scan speed as it is constrained by the cantilever. Many other practical factors such as scanner resonances can limit image fidelity in practice, as discussed in Section 2.3.

2.1.1 Discussion on Contact Mode Scan Speed Limits

The previous section provided understanding that the detectability of topographic features sets a constant, maximum velocity ($\dot{x}_{max}$, by Eqns. (2.11) and (2.14)), and this realization informs the design of the MIT High Speed AFM of Chapter (5). It is argued that constant-velocity scan speed is an important characteristic of high speed AFM where the majority of the imaging time is spent in operation at $\dot{x}_{max}$, and therefore the preferred high speed AFM is one that operates with constant velocity triangular scan command signals, and not sinusoidal signals where $\dot{x}_{max}$ is only occasionally achieved, as other researchers have proposed [49]. This issue is discussed in more detail in Section 2.3.

The preceding analysis also indicates how sample compliance limits scan speed. Specifically, the modeling indicates what many microscope operators find intuitive: that imaging compliant samples must be done slowly (and with cantilevers that are also compliant) in order to maintain reasonable image quality. Conversely, this indicates why it is easier to quickly scan a hard sample, which is why stiff samples such as mica and collagen are chosen in Chapter 4 to study the effect of scanner performance on image quality—it is desired in that chapter to eliminate the possibility that sample compliance was introducing an artificial restriction on imaging speed.

Further, it is not immediately clear that imaging in liquid necessarily leads to a lower

$\dot{x}_{max}$, as scanning in liquids will increase the values of both b and m as the liquid contributes to increased energy dissipation and hydrodynamic added mass [75]. The fundamental limits to high speed AFM imaging in liquid is still not fully understood and currently is an area of active research [99, 71, 6].

Finally, Equation (2.14) indicates that in order to enable higher scanning speeds in the presence of high damping, a stiffer cantilever might be used. However, stiff cantilevers are prone to damaging compliant samples such as biological specimens or polymers [16]. A preferable solution (and one that equally benefits both the low and high damping scenarios) is to decrease the mass of the cantilever. Decreasing the mass while maintaining suitable compliance provides a cantilever that is both gentle to the sample and sensitive at high scan speeds. However, to make smaller cantilevers while maintaining similar compliance properties poses difficult fabrication challenges, as cantilever thickness must be minimized. The following section discusses the need for small cantilevers in greater detail. These small cantilevers are essential for the MIT High Speed AFM described in Chapter 5, and are often used in this work even with conventional AFMs to ensure that cantilever bandwidth is not influencing image quality when using piezo tubes at high speed (Chapter 4).

2.1.2   A Need for Small Cantilever Probes

A discussion on the properties that affect contact mode imaging speed clearly point to the advantages of cantilevers with lower mass; and in Section 2.2, discussion on tapping mode speed limitations describes how the cantilever bandwidth can be increased by either decreasing the Q factor or by increasing the resonant frequency of the probe—this also requires reducing the mass.[2] This realization has lead a few cantilever suppliers to begin fabricating advanced small cantilevers.

Briefly, the targeted dimensional properties of small cantilever are revealed in the basic mechanics of a fixed-free beam model. Consider the stiffness of diving-board shaped cantilevers

$$k = \frac{3EI}{L^3} \tag{2.16}$$

---

[2]A reduction in the damping negatively affects the sensitivity of cantilevers in tapping mode, as will be addressed.
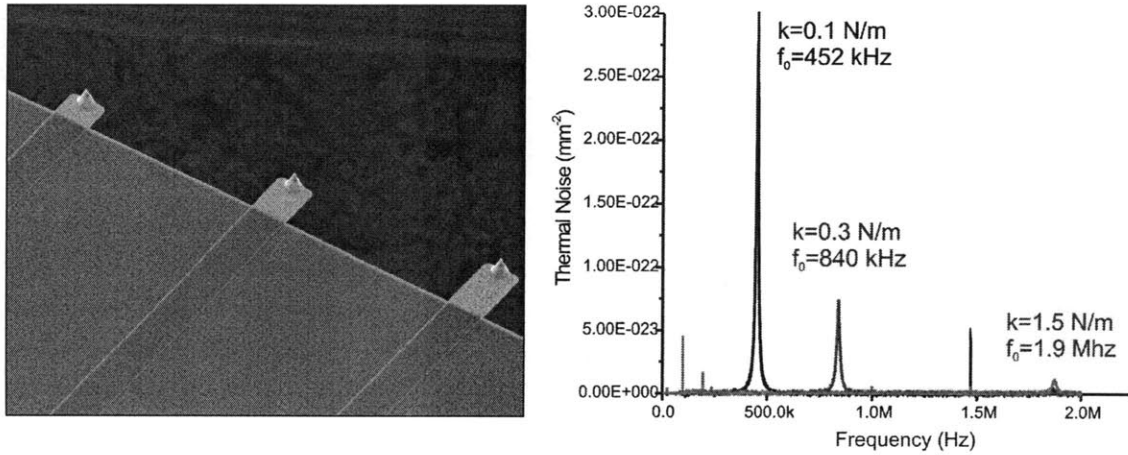
Figure 2-2: Small cantilevers can be fabricated with resonance frequencies up to 1.9 MHz and low stiffnesses [38]. These small cantilevers are essential for the MIT High Speed AFM discussed in later chapters, and are used even with conventional microscopes at high scan speeds to ensure that cantilever detection bandwidth does not introduce artificial speed limitations when exploring the limits of piezo tube actuators.

where the moment of inertia is given by

$$I = \frac{wt^3}{12L^3} \tag{2.17}$$

and

t...thickness $\qquad w$...width

l...length $\qquad E$...Young's modulus.

Therefore

$$k = \frac{Ewt^3}{4L^3}. \tag{2.18}$$

So by minimizing the width and especially the thickness, the cantilever stiffness can be reduced, and if the total mass of the cantilever is reduced, the result is a cantilever with a high resonance frequency and good sensitivity. Small cantilevers with these desirable properties have recently become available [38]. The devices have resonances as high as 1.9 MHz with stiffnesses comparable to conventional cantilevers while still providing a sharp probe for high resolution imaging (see Figure 2-2).
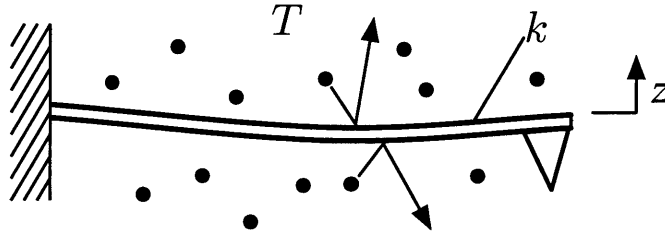
Figure 2-3: An AFM cantilever is modeled as a simple harmonic oscillator with stiffness k at thermal equilibrium in the surrounding gaseous environment. Random motion causes gas molecules at temperature T to impact the cantilever, resulting in cantilever deflection in the z direction.

Small Cantilever Noise Performance and the Equipartition Theorem

An additional benefit to small cantilevers is the demonstrated improvement in noise performance for sensitive measurement [97], which is derived from the Equipartition Theorem. At the length scale of AFM probes, measuring the cantilever deflection is limited by thermal noise.

The equipartition theorem, an important result in thermodynamics, statistical mechanics and kinetic theory, says that any variable z representing a degree of freedom and entering the Hamiltonian through a quadratic additive term z^2, has a mean thermal energy equal to $\frac{1}{2}k_B T$ where T is the temperature and k_B is the Boltzman constant [62].

Consider a cantilever modeled as a simple harmonic oscillator parameterized by stiffness k, and has a degree of freedom in the z direction (see Figure 2-3). The gas molecules from the surrounding environment impinge on the cantilever in all directions, but only the perpendicular component of the impacts contribute to cantilever motion (*i.e.*, motion in the z direction). Equating the kinetic energy of the gas molecules to the oscillator's potential energy for a system in thermal equilibrium, we have an expression for the mean-square free end displacement of the end of the cantilever

$$\frac{1}{2}k <\Delta z^2> = \frac{1}{2}k_B T. \tag{2.19}$$

Finally, since the modeled cantilever force is linear with displacement, we have the force

due to thermal noise:

$$<\Delta F^2> = k k_B T. \tag{2.20}$$

Equation (2.20) represents the minimum theoretical mean-square force detectable by deflection of the AFM cantilever. This sensitivity limit is governed by the stiffness of the cantilever at a given temperature. This analysis provides another motivation for the use of small cantilevers in high speed AFM imaging—with advanced fabrication techniques that minimize its mass and stiffness, the resulting cantilever is both fast and sensitive.

In addition to providing fast and sensitive imaging in contact mode, small cantilevers are shown to be important for tapping more imaging as well, as the following section on speed limitations in tapping mode imaging explains.

2.2 Tapping Mode Scan Speed Limitations

This section describes the phenomena which limit the scan speed in tapping mode operation. In particular, careful attention must be paid to the quality factor (Q factor) of the oscillating cantilever, and it is shown that the Q factor is a critical parameter that balances imaging sensitivity and scan speed. Additional considerations such as RMS-to-DC conversion time, and controller wind-up are also discussed as factors that impact scan speed in tapping mode.

As described in Section 1.1.2, AFM operation in tapping mode involves oscillating the cantilever near its resonant frequency ω_n, and servoing the sample height such that the oscillation amplitude is held fixed. To prepare the AFM for imaging in tapping mode, the magnitude response of the cantilever near its resonant frequency is obtained with the cantilever oscillating away from the surface (*i.e.*, its free-air magnitude response). In this free-air situation, the cantilever is adequately modeled as a simple mass-spring-damper with mass m, stiffness k, and damping coefficient b. For reasons that will become clear later, the cantilever is then driven to oscillate at a fixed frequency ω_L, which is less than the natural frequency, and that frequency is selected such that the free-air oscillation amplitude a_f is usually 70–80% of the amplitude at ω_n (see point (1) of Figure 2-4).

With the cantilever still oscillating at ω_L, the sample is brought closer to the cantilever. As the distance between the cantilever tip and the sample, δ, is decreased, surface interac-
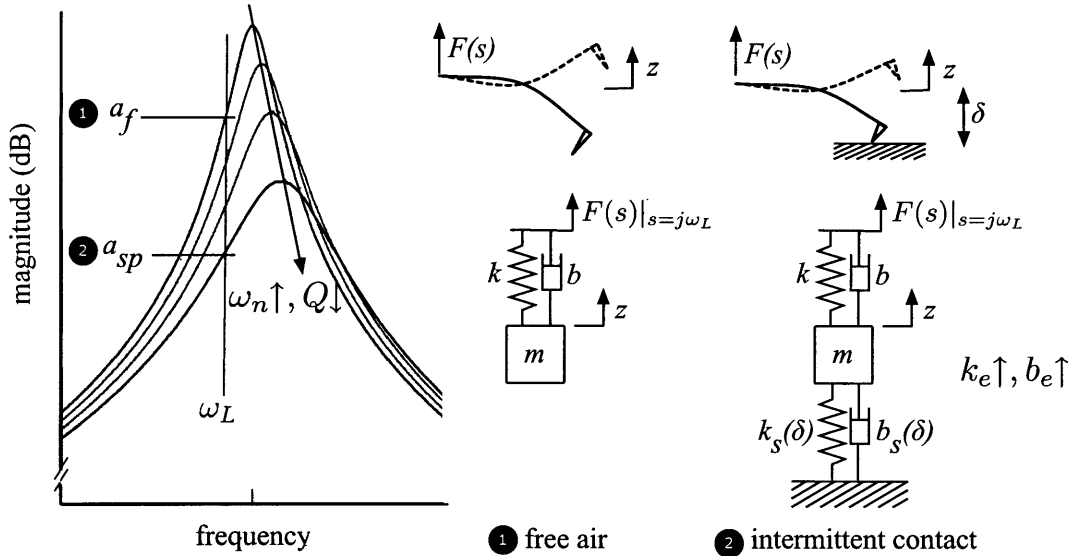
Figure 2-4: Sample interactions cause an increase in effective stiffness and damping of the oscillating cantilever as compared to the free-air situation. This manifests as a shift and distortion of the magnitude response. When oscillated at a fixed frequency $\omega_L < \omega_n$, this distortion is observed as a decrease in oscillating amplitude (from a_f to a_{sp}).

tions influence the dynamics of the cantilever. Specifically, additional stiffness is observed through the long-range interaction forces that can be modeled as position-dependent to a first-order approximation $(F_s = k_s(\delta)\delta + \mathcal{O}(2))$. This sample-induced stiffness $k_s(\delta)$ is a function of the separation between the oscillating cantilever and the sample. At the same time, air or liquid is squeezed out from between the cantilever and surface and causes additional damping $b_s(\delta)$, which is also separation-dependent. Therefore, interactions with the sample increase the effective stiffness $(k_e = k + k_s)$ and effective damping $(b_e = b + b_s)$ of the oscillating cantilever. This increased stiffness manifests as a shift in resonant frequency $(\omega_n = \sqrt{k_e/m})$ while the increased damping is reflected as a decrease in the resonator's Q factor $(Q = \sqrt{k_e m}/b_e)$. See Figure 2-4, point (2), and note how the sample interactions shift and distort the shape of the magnitude response.

In typical AFM configurations, the root-mean-square (RMS) oscillating amplitude is converted to a DC value in a lock-in amplifier. Lock-in amplifiers use the orthogonality of sinusoids to extract a signal of interest at a single frequency, even with signal-to-noise ratios as low as -60 dB. In tapping mode operation, lock-in amplifiers are used to determine the

oscillation amplitude at ω_L, and a control system regulates the separation distance such that the oscillation amplitude is held fixed at the setpoint a_{sp} (point (2) in Figure 2-4).

Because both k_s and b_s are functions of the cantilever-sample separation δ, changes in topography are detected indirectly through these parameters. Stated differently, variation in topography alters the stiffness and damping of the oscillating cantilever, which changes its resonant behavior (sampled only as an amplitude at ω_L) and by measuring the change in oscillation amplitude, changes in topography can be detected. However, the sensitivity with which they can be detected is directly related to the Q factor of the cantilever and discussed in the next section.

2.2.1 Q Factor and Sensitivity

As previously described, detection of topography is measured as a change in amplitude of the oscillating cantilever, where the sample interaction forces alter the magnitude response. Therefore, the amount of change in amplitude for a given change in topography determines how sensitive a cantilever is to sample topography. In other words, the slope of the magnitude response at ω_L determines the cantilever sensitivity. This characteristic is shown in Figure 2-5 for cantilevers with two different Q factors. It is noted that cantilever sensitivity clearly benefits from a high Q factor.

Whereas cantilevers with high Q factors lead to sensitive detection of interaction forces, they negatively impact scan speed as described in the following section.

2.2.2 Q Factor and Scan Speed

Obtaining scan speed limits for AFM operating in tapping mode is somewhat more complex than for contact mode, due to the coupling and interaction among microscope subsystems, including those interactions from the oscillating probe, feedback actuator bandwidth, error signal saturation, and RMS-to-DC conversion circuitry [58, 93]. This section describes the important parameters that limit scan speed in tapping mode, and particular attention is paid to the cantilever's Q factor.

A schematic of the step response of an AFM in tapping mode is shown in Figure 2-6. The figure illustrates how the oscillating cantilever, its measured RMS amplitude, the feedback
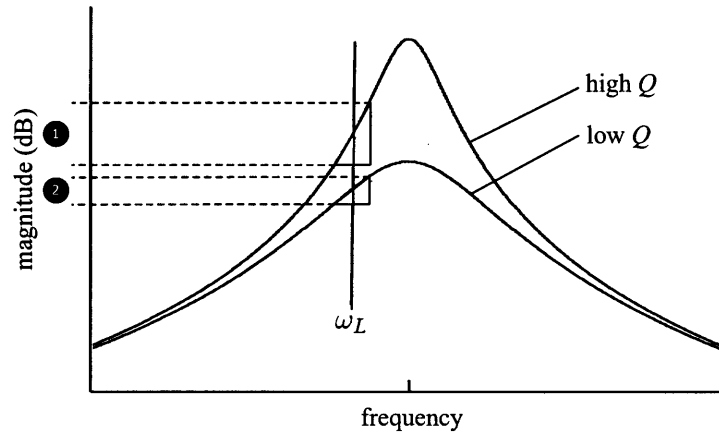
Figure 2-5: Q factor impact on imaging sensitivity in tapping mode. A high Q factor pro-
vides a larger change in oscillation amplitude (marker (1)) for a given change in topography,
compared to that for a low Q factor cantilever (marker (2)). Recall that topography change
manifests as a shift and distortion of the magnitude response of the cantilever oscillating at
ω_L.

error and controller output react to both a step decrease, and a step increase in topography.
While in intermittent contact with the sample, the feedback controller regulates the height
of the sample such that the oscillation amplitude of the cantilever is equal to the setpoint
amplitude a_{sp}, which is some fraction of the free-air oscillation amplitude a_f (typically
70–80%).

(Refer to Figure 2-6 for the following details.) At point (1), the scanning cantilever
encounters a step decrease in topography. Because cantilevers typically used in AFM have
large Q factors, the cantilever's oscillation amplitude does not quickly react to a loss of
sample contact.[3] This phenomenon is often termed the "ring up" of the cantilever and
describes the slow increase in oscillation amplitude (over a few periods) to the free-air am-
plitude a_f. The increase in oscillation amplitude follows an exponential with time constant
Q/ω_n, where ω_n is the natural frequency of the cantilever [72]. Additionally, due to typical
implementations of RMS-to-DC circuits, the RMS value is computed as a windowed aver-
age of several previous cycles, and therefore the increasing amplitude is not immediately
detected due to this measurement delay (point (2)). When this RMS-to-DC delay is com-

---

[3]Recall that the Q factor is often defined as the ratio of stored energy in an oscillator to the dissipated
energy per cycle. Thus for large Q oscillators, little energy is input per cycle and rapid changes of amplitude
are not possible [41]. In other words, it can take many periods for a high Q oscillator to "ring-up."
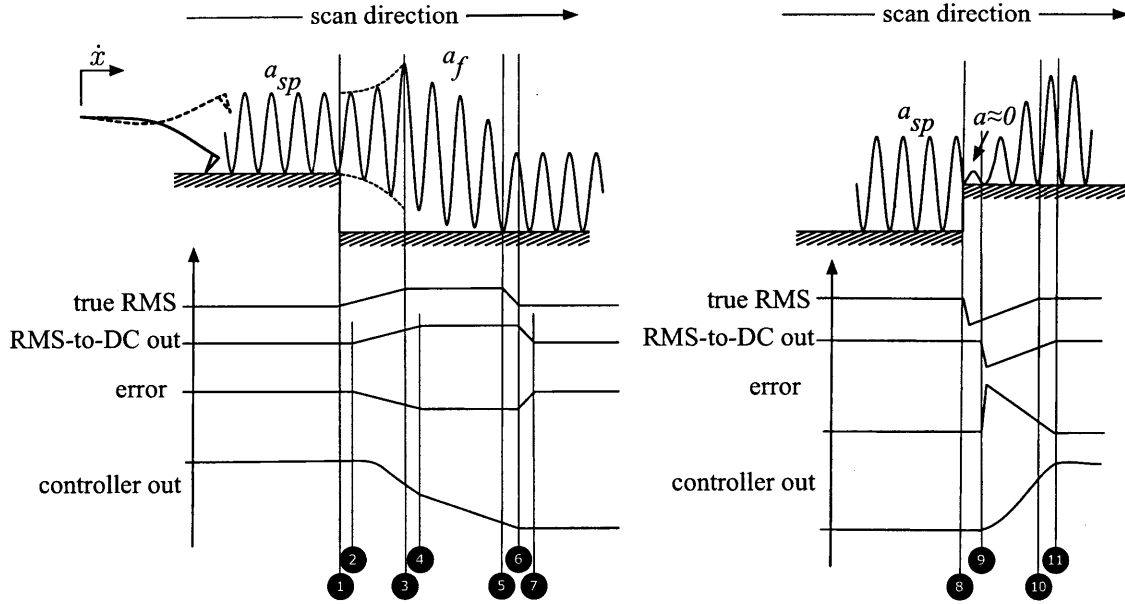
Figure 2-6: Model used to determine limits on scan speed in tapping mode imaging.

bined with the cantilever ring up, detection of the loss of topography by the controller is not immediate and can be as long as a millisecond for typical tapping mode cantilevers [93].

At point (3), the cantilever has reached its free-air oscillation amplitude a_f, and after another RMS-to-DC delay (point (4)) the error signal saturates at $e_{max} = a_{sp} - a_f$. Because the AFM is typically operated with a_{sp} at around 70–80% of a_f, the magnitude of the error signal saturates at a small value, *i.e.*, the error amplitude is strictly bounded. For linear controllers whose output scales with the magnitude of the input, this small-value error signal saturation is problematic for fast reaction to changes in topography.

With a small saturated error signal, the controller reacts linearly between points (4) and (6) and is associated with the integral action of the controller. This integrator action is typical of systems with saturation, and the slew rate is a function of controller gains and setpoint amplitude. This point also highlights how critical integrator anti-windup strategies are for z feedback controllers in tapping mode. It is noted that the feedback actuator bandwidth is often not the limiting subsystem here (although resonances excited at faster scan rates can be coupled to the z axis, for conventional controller structures and typical piezo tube scanners, the factors discussed here are dominant). The cantilever

approaches the surface until contact is made with the sample at point (5). Another delay associated with RMS-to-DC conversion is experienced between points (6) and (7), then the error signal returns to zero. The image that is generated from the controller output signal, and although it roughly has the same morphology as the true topography, the mechanical detection (cantilever ring-up) and electrical detection (RMS-to-DC conversion) contribute delays that cause loss of topographic information.

The right side of Figure 2-6 shows the response of an AFM is tapping mode to a step increase in topography. At point (8) the step is encountered, and if the step increase is sufficiently tall, the oscillation amplitude is quenched to zero. A short time later, (9) the RMS-to-DC converter registers the decreased amplitude. Note that here the error signal is not confined to as small a value as in the step decrease case, it can attain a value as large as a_{sp}, or nearly an order of magnitude greater than in the decreasing step case. Because the magnitude of the error is larger, the controller reacts with larger authority, and the response to a step increase is handled faster (between points (9) and (11)). Again, an RMS-to-DC conversion delay occurs between points (10) and (11) after the setpoint amplitude is actually reached.

While the previous discussion highlights the interaction of several parameters that influence scan speed in tapping mode imaging, we focus on the role of the cantilever Q factor, and the ring-up limitation it imposes. Mertz *et al.* [72] model the oscillating cantilever as a linear system with a simple transfer function. It has a low-pass frequency response with -3 dB bandwidth of

$$\Omega = \frac{\omega_n}{2Q} \tag{2.21}$$

This is in agreement with the time constant of the ring-up described earlier, and shows that high speed imaging benefits from a low Q factor and high resonant frequency. Understanding the role of the cantilever's Q factor on scan speed and senstivity has motivated the characterization and control of self-actuated cantilevers described in Chapter 3.

To the extent that cantilever ring-up limits detection and therefore scan speed, improvements in imaging speed can be made through active control of the Q factor, but the Q factor cannot be arbitrarily decreased without sacrificing sensitivity. This tradeoff is discussed in the next section.
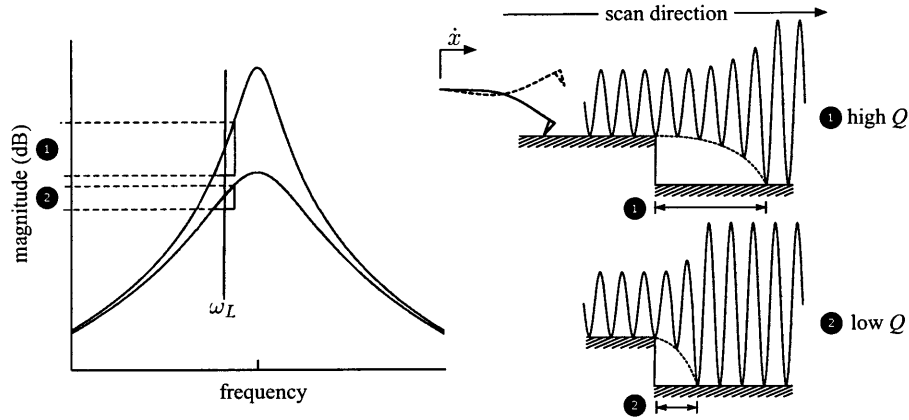
Figure 2-7: Q factor tradeoff between sensitivity and scan speed. (1) High Q cantilevers are sensitive to changes in interaction forces, but require longer times to react to a change in topography compared to (2) low Q cantilevers. Note that the Q factor can be interpreted as the number of periods required to react to a change in input energy of an oscillator, so while the two cantilevers in this figure oscillate at the same frequency, the cantilever labeled (1) takes more periods to react to the topographic change than that labeled (2).

2.2.3 The Tradeoff between Scan Speed and Sensitivity

There exists an inherent tradeoff in AFM operation associated with the Q factor of the cantilever. High Q cantilevers (labeled (1) in Figure 2-7) are sensitive to changes in topography (as evidenced by the large slope around ω_L in magnitude response of Figure 2-7) but due to the long ring-up time, require slower scan speeds. Conversely, low Q cantilevers (labeled (2) in Figure 2-7) are not as sensitive to changes in interaction forces, but react faster to changes in topography.

Working around the tradeoff between scan speed and sensitivity can be accomplished with two advanced cantilever technologies (i) small cantilevers, or (ii) active cantilevers with integrated actuators. Regarding the former, small cantilevers offer a way to increase the resonance frequency while maintaining the damping properties (refer to Section 2.1.2). The small cantilevers of Figure 2-2 have high resonant frequencies and similar Q factors to conventional tapping mode levers. These cantilevers react to topography in the same number of periods, but because of the higher resonance, topography detection occurs over a shorter distance, and therefore higher scanning speed is obtained with the same imaging results. This is illustrated in Figure 2-8, which compares a low Q and high Q cantilevers,
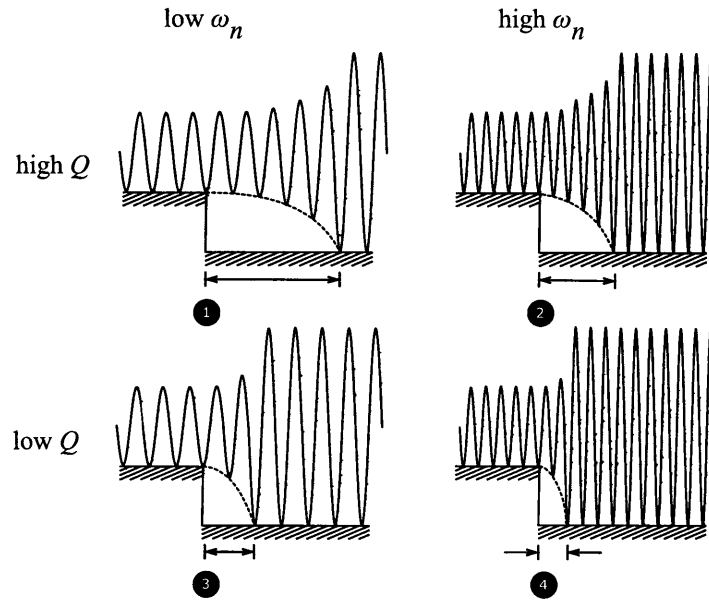
Figure 2-8: Increasing the resonant frequency of the cantilever shortens the response time to a step change in height for a given Q factor (*i.e.*, from (1) to (3) or from (2) to (4)). While increasing the natural frequency is not difficult, doing so without increasing the Q factor poses manufacturing challenges.

and conventional cantilevers (low ω_n) with small cantilevers (high ω_n).

A second approach to circumventing the scan speed/sensitivity tradeoff is one that takes advantage of a new kind of cantilever that incorporates integrated actuation [14]. Used in conjunction with the existing tapping piezo, a multi-actuator cantilever that allows adaptive, realtime control of the Q factor can balance these competing demands, alternating between high sensitivity while on interesting topography, and fast scanning operation otherwise. It has been shown that using active feedback techniques to control the cantilever Q factor leads to increased scan rates. [93]. And while there has been much attention paid recently to the *measurement* of higher cantilever harmonics [47, 85, 84, 86], *actuation* of higher harmonics is only recently addressed [100], and to the best of the author's knowledge, no researcher and has yet to discuss simultaneously controlling the Q factor around each of the higher resonant modes through the integrated actuators, which may be a fertile avenue for later work. Later sections of this thesis will focus on characterization of novel cantilevers with integrated actuators and control strategies that take advantage of additional input
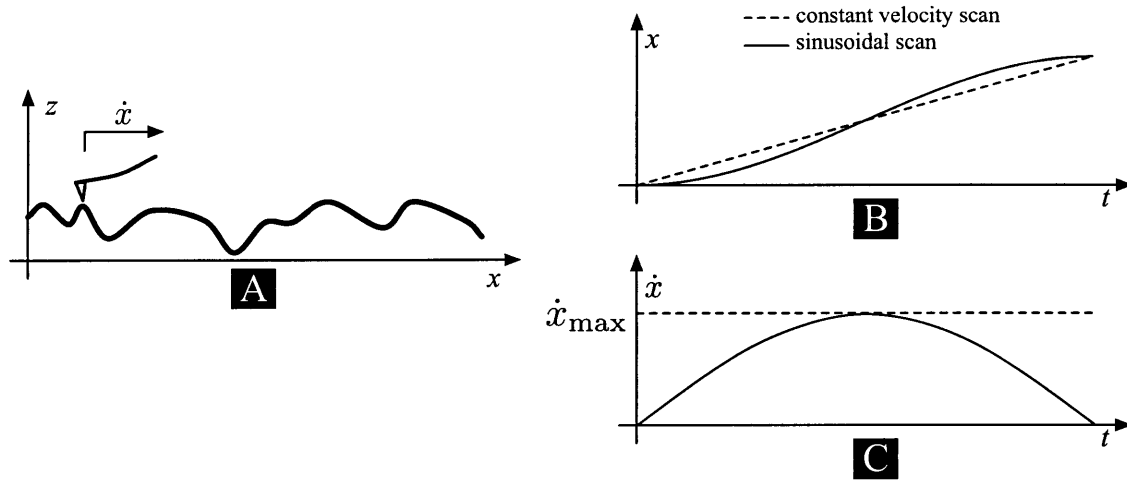
Figure 2-9: Preferred constant velocity scanning allows the AFM to be operated at $\dot{x}_{max}$ continuously while imaging, whereas sinusoidal scanning attains the maximum velocity only at a single point. A. The cantilever is scanned over topography with velocity $\dot{x}$. B. The position profile of the cantilever as a function of time shows the difference between constant velocity scanning and sinusoidal scanning. C. When considering the velocity of the two scanning strategies, it is apparent that sinusoidal scanning only achieves the maximum scan velocity, $\dot{x}_{max}$, at the center of the scan line, resulting in an inefficient strategy for high speed image operation.

authority afforded by integrated actuation. With the thorough characterization of the issues surrounding these active cantilevers presented in Chapter 3, the ultimate goal of adaptive, realtime Q control for balancing speed and sensitivity can be realized in future work.

2.3 Scanner Limitations set by the Cantilever

In later chapters, an automatic approach for dealing with positioning errors introduced by the AFM piezotube scanner is discussed (Chapter 4) and a prototype high speed AFM built at MIT is presented (Chapter 5). Both chapters require an understanding of the limitations to AFM imaging imposed on the scanning subsystem, which is described briefly in this section.

Section 2.1 modeled the cantilever dynamics in contact mode in order to understand the speed limitations of using scanned mechanical detectors for imaging. The main result indicated that the physical properties of the cantilever set a maximum value on the allowed

scan speed, denoted $\dot{x}_{max}$. For the custom-built microscope described in Chapter 5, it is desired to image as fast as possible while maintaining suitable image quality. Toward that end, maximum efficiency dictates that the microscope be operated at $\dot{x}_{max}$. This mode of operation requires constant velocity scanning (using triangular shaped scan command signals) and precludes the use of sinusoidal commands that achieve $\dot{x}_{max}$ only at a single point in the image (see Figure 2-9).[4] However, the Fourier components associated with the sharp turnaround nature of triangular scan commands (during the short transition from trace (right-to-left) to retrace (left-to-right)) excite scanner resonances that can corrupt the image. This issue is addressed in regard to conventional piezo tube scanners Chapter 4, and a suitable controls approach based on input shaping enables undistorted high speed imaging with the preferred constant velocity scan rate.

2.4   Chapter Summary

A first-principles model of the cantilever operting in contact mode and interacting with the sample revealed conditions that set the maximum scan velocity. These conditions point to an improvement in scan speed that can be realized with small cantilevers, and suggest that constant velocity scanning is desired for efficient operation of the MIT High Speed AFM, which is the subject of Chapter 5.

Additionally, an examination of cantilevers in tapping mode indicate the complicated interaction of cantilever resonance properties, RMS-to-DC conversion, and the z feedback controller bandwidth have on topography tracking and therefore scan speed. Further, analysis of the Q factor of the oscillating cantilever reveals a natural tradeoff between reaction time (scan speed) and sensitivity. It is suggested that by using feedback control to actively shape the Q factor of cantilevers at the fundamental and higher harmonics, could lead to a detector that achieves both the desired scan speed and sensitivity. Before that idealized instrument can be realized, novel cantilevers with embedded actuation and sensing must be fully characterized, which is the focus of the next chapter.

---

[4]Although scanner resonances may be avoided with sinusoidal imaging, because the maximum velocity is achieved at the center of the scan line, the worst detector performance is attained in the middle of the image—presumably the part of the image in which the user is most interested.

Chapter 3

Active Cantilevers for High Speed, User-Independent Imaging

The limitations of scan speed in AFM imaging explored in Chapter 2 indicate that for higher speeds to be reached while maintaining good imaging sensitivity, the Q factor must be carefully controlled. Toward that end, a new cantilever with integrated sensing and actuation is characterized, which has the potential of increased controllability and observability. The goal of this chapter is to obtain a thorough understanding of the active cantilever dynamics and its behavior, and using the analysis performed in Chapter 2, design a complete model-based controller that can be integrated into a high speed AFM system with minimal involvement from an expert user.

This chapter introduces a new type of active cantilever with integrated thermal actuation and piezoresistive deflection sensing. Experiments are performed to understand and characterize (1) its behavior near resonance, (2) the bandwidth of the thermal actuator, (3) the suitability of the integrated sensor, (4) the nature of a discovered actuator-sensor signal crosstalk, (5) the undesirable coupling at resonance between mean deflection and oscillation amplitude, and (6) evaluation of a model-based compensator designed to increase the thermal actuator bandwidth. Final experiments in this chapter use the integrated actuator for tracking topography while imaging, and demonstrate increased stability margins in the z feedback loop.

3.1   Introduction

The expansion of AFM technology to fields beyond traditional metrology, nano-scale materials science, and bio-molecular research has been hampered by several drawbacks inherent to conventional AFM. Its long imaging times of up to 20 minutes and optical alignment procedures require operators with both patience and skill. To address these two main constraints, ongoing research is exploring the fabrication of AFM cantilevers with integrated sensing and actuation [50, 51, 78, 79]. With regard to deflection sensing, complicated laser/photodiode alignment and bulky optical components characteristic of conventional AFM can be eliminated with a self-sensing cantilever. These ideas were recognized shortly after the introduction of batch-fabricated cantilevers [1, 3], and integrated detection methods developed include interferometric [83], capacitive [12] and piezoresistive [50, 51, 64, 67, 73] approaches.

Advances in cantilever actuation technology stem from an understanding of the limitations of the mechanical scanner systems used in AFM. Scanning the probe quickly excites resonances in the scanner which distort the image [89]. Also, the speed of the mechanical detection of the topography depends strongly on the resonant frequency and the Q factor of the cantilever (see Section 2.2.2) [93]. The dynamics of the cantilever, coupled with the dynamics of the scanner, impose a limit on the speed of the feedback loop which tracks sample topography and generates an image. The actuator that tracks the topography in the z direction must have a higher bandwidth $\omega_{\mathrm{bw},z}$ than the highest spatial frequency f_{max} in the imaged sample times the scanning speed $\dot{x}$.

$$\omega_{\mathrm{bw},z} \gg f_{\mathrm{max}} \times \dot{x} \tag{3.1}$$

For a conventional piezo tube with a resonance frequency around 2 kHz in the z direction and scanning a 10 $\mu m \times$ 10 μm image at 1 Hz linerate, the maximum spatial frequency that can be recorded is:

$$
\begin{aligned}
f_{\mathrm{max}} \quad &\ll \quad \frac{\omega_{\mathrm{bw},z}}{\dot{x}} \\
&= \quad \frac{2\ kHz}{10\ \mu m/s} = 200\frac{1}{\mu m}
\end{aligned}
\tag{3.2}
$$

This corresponds to a minimum imaged spatial period of $\lambda = 5$ nm. At this scanrate, a 10 $\mu m \times 10$ μm image takes 8.5 minutes. In order to reduce the imaging time, it is essential to increase the resonant frequency of the z actuator. Since the resonance frequency depends on the mass and stiffness, approaches have been developed to make the actuator support structure stiffer [38] and the actuators smaller [5, 53]. Whereas traditional AFM follows sample topography with actuators that have bandwidths in the z direction on the order of $0.5 - 2$ kHz, it is recognized that these bandwidths can be increased by directly actuating the cantilever for topography tracking. New actuation methods for directly bending the cantilever have been developed and include manipulation via: thermal bimorph effect [48, 50, 69], electrostatic [12] or electromagnetic [66] forces, or using piezo films [67, 73].

By using an actuator directly on the cantilever, one can take advantage of the small size and the high resonance frequency of the actuator [67]. Early work made use of actuators that consist of piezoelectric material on the back of the cantilevers, but require relatively high voltages and therefore make these cantilevers incompatible with imaging in liquids or inspection of semiconductor wafers. An alternative approach relies on the thermal bimorph effect, where materials with different coefficients of thermal expansion are used to fabricate the cantilever, and an integrated micro-heater introduces the small amount of heat necessary to induce deflection [50, 78].

These advances in cantilever technology eliminate the need for large portions of traditional AFM infrastructure, making nanoscale deflection sensing easier, more user-friendly, more compact, and faster. In doing so, these new features would expand the potential applications for AFM technology into the realm of inexpensive sensing for quality control, clinical testing, *in vivo* diagnostics of biological tissue, or parallel imaging with arrays of self-sensing/self-actuating cantilevers in inspection of microelectronic manufacturing.

In this chapter, the properties of a thermally-actuated, piezoresistive-sensed cantilever are investigated with the goal of understanding its dynamics to an extent that model based or Q control can be applied and the active cantilever can be incorporated into a high speed AFM system.
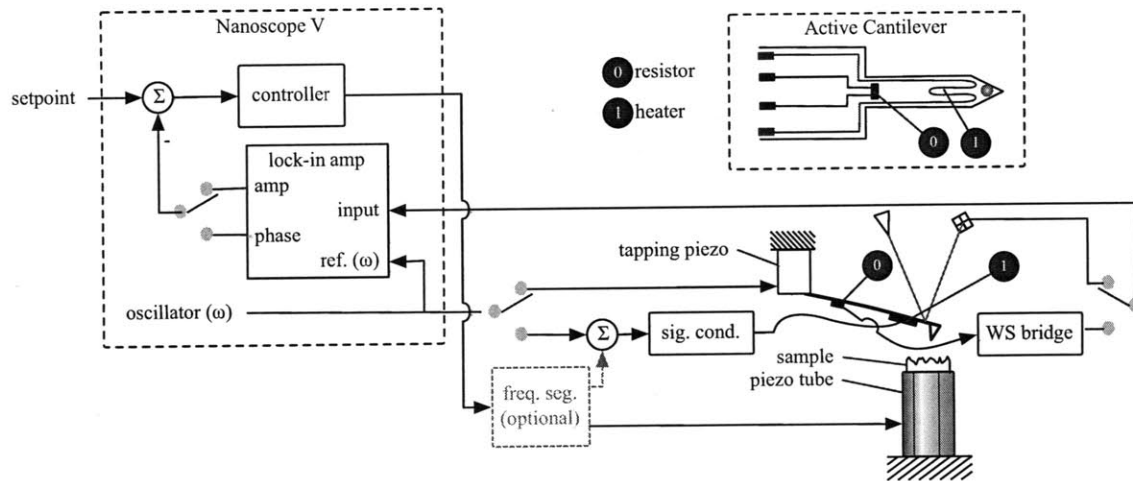
Figure 3-1: The active cantilever is integrated into an existing Multimode V AFM system using a custom cantilever holder that includes a tapping drive piezo and readout electronics. Switches select between conventional tapping piezo or thermal excitation, and between laser/photodiode or piezoresistor readout.

3.2   Description of Setup and Instrumented Cantilevers

The fabrication and basic characteristics of thermally driven cantilevers with integrated resistive readout has been described in detail previously [50, 78]. Briefly, we use silicon cantilevers 320 μm long, 110 μm wide and 3–5 μm thick to investigate the properties of the self-sensing and actuation mechanisms. The cantilevers have a piezoresistive element located at the base of the cantilever and thermal heating loops near the tip. Electrical contacts are made on the cantilever substrate and wire bonded to a printed circuit support chip. There are two contacts for the micro-heater ($R \approx 22\ \Omega$) and two for the piezoresistor ($R \approx 1\ k\Omega$).

A schematic of how the active cantilever is integrated into an existing AFM is shown in Figure 3-1. The cantilever is mounted on a custom cantilever holder (with integrated electronics and a piezo stack for exciting the cantilever near its resonant frequency) in a Multimode V AFM (Veeco Metrology) and connected to Nanoscope V AFM controller. The tapping signal from the Nanoscope V oscillator is switched between the tapping piezo stack (conventional AFM configuration) and the integrated micro-heater. When driving the micro-heater, additional signal conditioning is used to add a DC offset and limit the current

for reasons that will be discussed later. The cantilever deflection is measured with either the conventional laser and photodiode, or the integrated piezoresistor, and a switch is used to select between those outputs. The piezoresistor acts as a strain gage whose resistance is a function of deflection and its change in resistance is measured with a typical Wheatstone bridge circuit and subsequent amplification. The output of the Nanoscope V controller is directed to the piezo tube for conventional imaging, but in later experiments, imaging is conducted over both the piezo tube (for large displacements) and the thermal actuator (for high bandwidth displacements). When imaging using both actuators, the single control output is segmented in the frequency domain with a combination of low-pass and high-pass filters and connected to the two z axis actuators.

The configuration described here permits use of the cantilevers both in conventional AFM mode, as well as using self-sensing and self-actuating for oscillation at resonance and topography tracking.

3.3 Cantilever Behavior

3.3.1 Deflection Sensing

The deflection of the cantilever can be measured using the piezoresistor at the base of the cantilever. The piezoresistor is used as one leg of a Wheatstone bridge with a 2.048 V precision voltage source as bridge supply (Figure 3-6). The bridge signal is amplified with an AD8250 instrumentation amplifier (Analog Devices), and further amplification is occasionaly performed with an optional external operational amplifier. Figure 3-2 shows the deflection force curves of the self sensing cantilever measured (A) with the optical lever detection and (B) with the sensing resistor. The gain of the final amplification stage in the resistor readout circuit is adjusted such that the deflection sensitivity of the resistor readout approximately matches the optical deflection sensitivity.[1]

---

[1]It should be noted here that the optical deflection sensitivity depends strongly on the alignment of the laser on the cantilever. Therefore, the optical deflection sensitivity will be somewhat different each time the laser is readjusted on the cantilever before imaging.
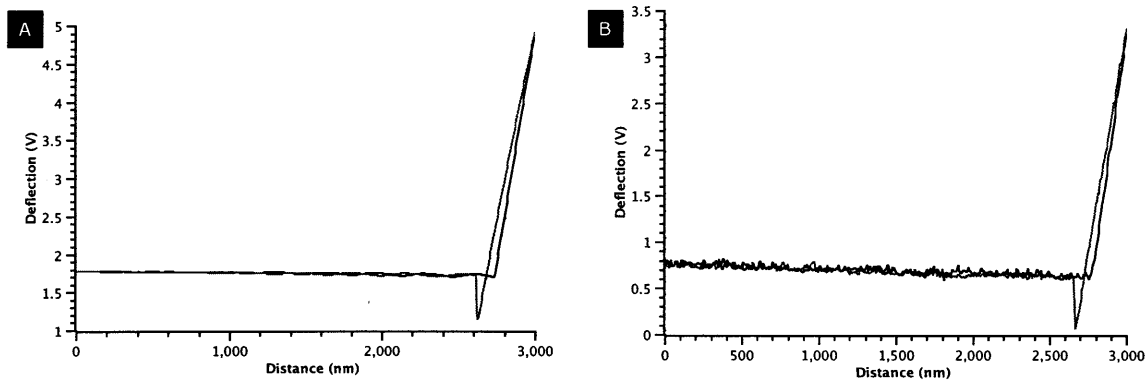
Figure 3-2: Contact mode approach curves with deflection measured by A) the standard laser and photodetector and B) integrated piezoresistor. The gain of the sensor resistor readout electronics is adjusted to match the deflection sensitivity of the optical lever detection.
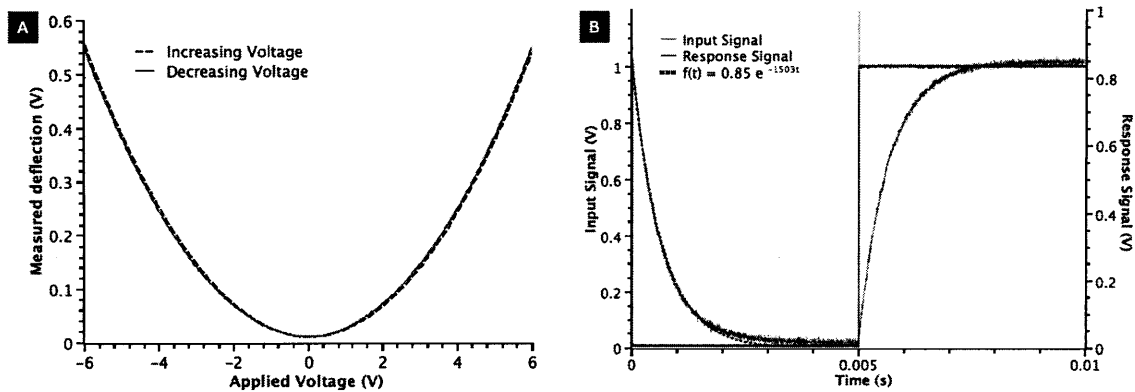
Figure 3-3: Low frequency behavior of cantilever actuator. A) Deflection of the cantilever for a given applied DC-voltage. B) Step-response of heater actuation with laser readout.

3.3.2 Thermal Actuation

For AFM imaging in tapping mode, it is necessary to excite the cantilever around its resonant frequency as well as control the distance between cantilever and sample to track the topography. Using the actuated cantilevers in a conventional AFM setup allows comparison between the traditional means of cantilever actuation and the new integrated thermal actuator.

The cantilever actuation uses either the thermal bimorph effect with the micro-heater on the cantilever or standard mechanical actuation with a piezo mounted into the cantilever

holder. The mechanical actuation with the piezo can only be used for driving the cantilever in tapping mode around its resonance. However, the actuator on the cantilever can be used to drive the cantilever in resonance as well as deflect the cantilever at lower frequencies off-resonance—this below-resonance actuation can be used to track topography more quickly than with conventional actuators. When a DC voltage is applied to the micro-heater, the cantilever bends as shown in Figure 3-3A. Since the cantilever deflects with a change in temperature (due to differences in coefficients of thermal expansion), the deflection is proportional to the temperature change ΔT, which is in turn proportional to the dissipated electrical power P in the micro-heater. The dissipated power is the square of the applied voltage $(P = V^2/R)$, and therefore the cantilever deflection changes quadratically with the input voltage. Figure 3-3B shows the step response of the cantilever from thermal actuator to deflection. The time constant fit to a first-order exponential is 1503 s^{-1}, and is problematic for tracking topography at high imaging rates. This issue is addressed in Section 3.4.

Actuation around the resonant frequency of the cantilever can be achieved both with the micro-heater on the cantilever as well as the piezo built into the cantilever holder. Figure 3-4 shows the frequency response of the cantilever to a sinusoidal sweep, where the first and second resonances of the cantilever can be clearly seen.

3.3.3 High Frequency Behavior

To investigate the behavior of the thermal actuation around the resonant frequency, we compare the four combinations of actuation and sensing. Figure 3-5 shows the the cantilever behavior at its first resonance as excited with mechanical (piezo) actuation and thermal (heater) actuation and measured with laser readout and sensing resistor readout, respectively. The curves are recorded using a sinusoidal frequency sweep (Nanoscope V controller, Veeco Metrology). Qualitatively, the spectra of Figure 3-5 A, B and C show the same behavior, with more noise on the traces in case of the sensing resistor readout. Figure 3-5D, however, shows a less pronounced resonance peek and phase lead before the resonance. The phase change is also significantly less in magnitude (note the different phase axis in Figure 3-5D). Since this behavior only occurs when using both the thermal actuation
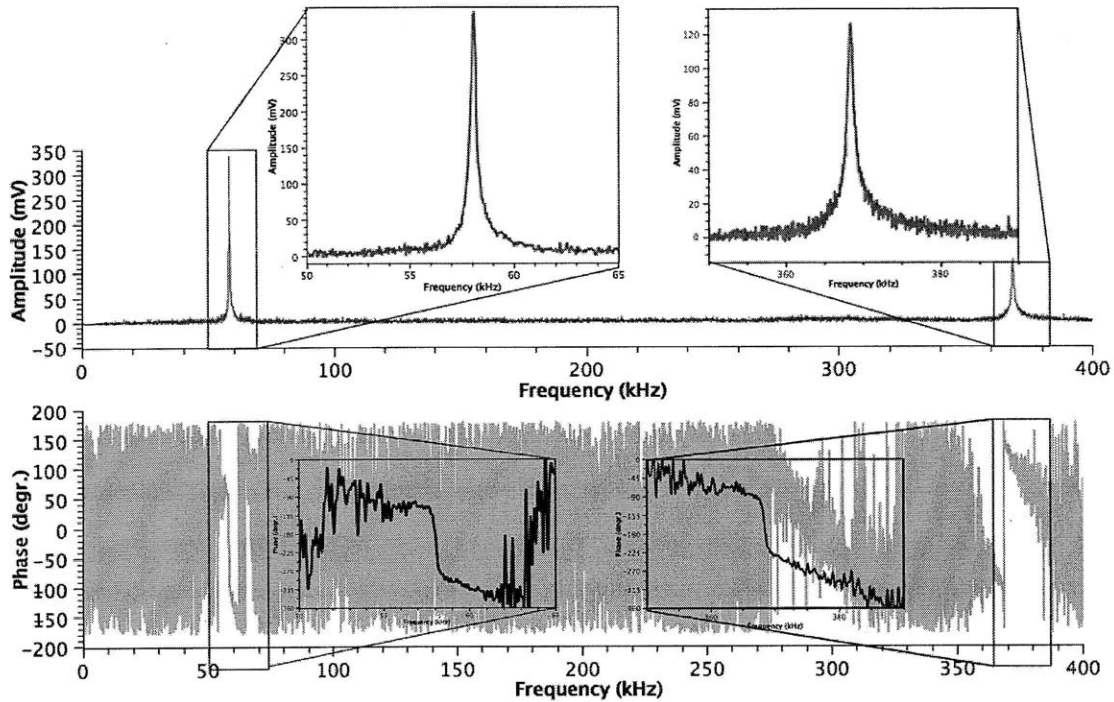
Figure 3-4: Sinusoidal frequency sweep over the first two resonant modes. Excitation with micro heater, readout with optical lever detection.

and the resistive sensing, it is proposed that this is not a physical property of the cantilever, but rather an artifact from the measurement. A similar behavior has been reported [23, 40] for accelerometers and we attribute this behavior to crosstalk between the actuator and the sensor.

Three types of crosstalk are possible between the thermal actuator and sensing resistor: capacitive, inductive, and thermal crosstalk. In general, capacitive crosstalk in electronic devices is dominant at higher frequencies, whereas inductive crosstalk is associated with lower frequencies. The thermal crosstalk is strongly dependent on the distance between the thermal actuator and the sensing resistor (in our case about 200 μm). Thermal crosstalk can be divided again into a low frequency and a high frequency component. A low frequency change in overall temperature of the cantilever will result in a mechanical bending of the cantilever due to the bimorph effect [50], as well as a change in the resistance of the sensing resistor due to its thermal coefficient. Both of these effects will change the voltage measured
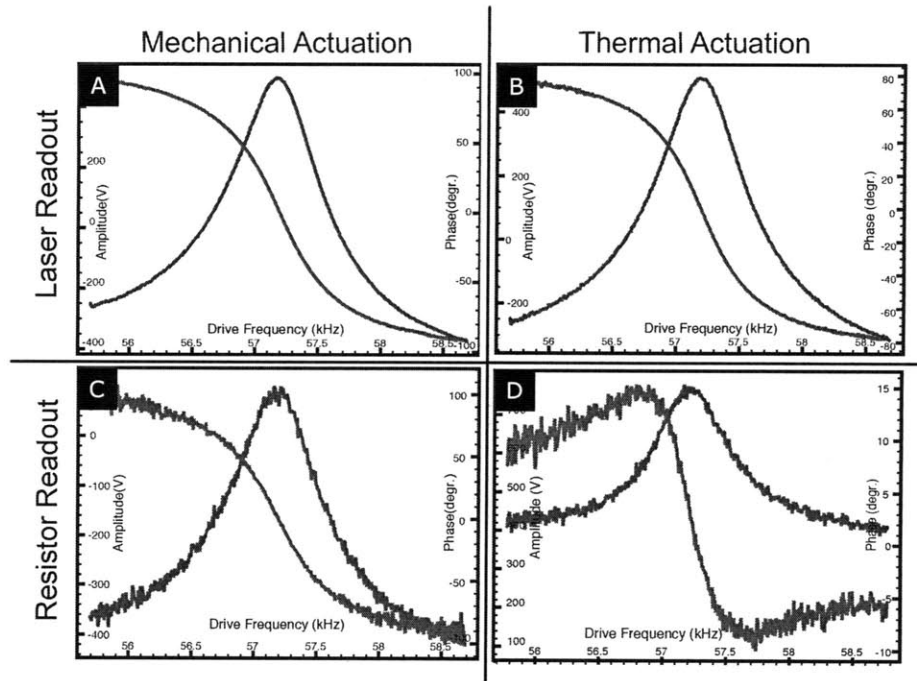
Figure 3-5: Swept sine wave tuning curves of active cantilever using optical deflection readout, sensing resistor readout, tapping piezo actuation and heater actuation. A) Optical lever detection and tapping piezo actuation (classical AFM setup). B) Optical lever detection and heater actuation. C) sensing resistor readout and tapping piezo actuation. D) sensing resistor readout and heater actuation.

at the output of the Wheatstone bridge, but only the first effect is due to an actual bending of the cantilever. Therefore this effect manifests as a shift of the mean value of the sensor signal over time. This is less problematic for tapping mode imaging, because the lock-in amplifier removes any offset in the sensor signal. However, it is still desirable to minimize this effect, because a large shift in the mean value can result in saturation of the preamplifiers. Therefore, the cantilever should be oscillated at its resonant frequency for a while before measurements are started in order to reach thermal equilibrium.

At higher frequencies (e.g. at the cantilever resonance), the amount of heat that reaches the sensing resistor is attenuated significantly [40]. The direct thermal crosstalk, which changes the resistor value due to its thermal coefficient, is negligible given the distance between the actuator and the sensor. Hence, at high frequencies the thermal influence of the drive signal on the sensor signal is reduced to the actual mechanical bending of the

cantilever (as is desired).
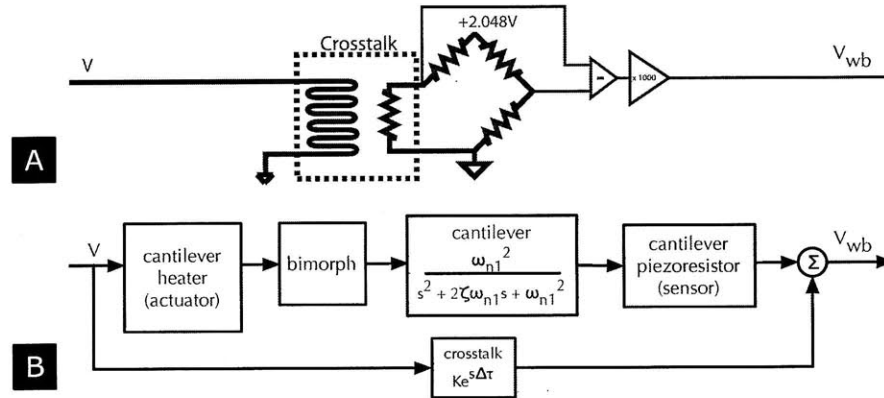
Figure 3-6: Model of the crosstalk using A) an electrical schematic and B) a block diagram. Connection of thermal actuator and sensing resistor with description of crosstalk between heating signal and resistor sensing signal.
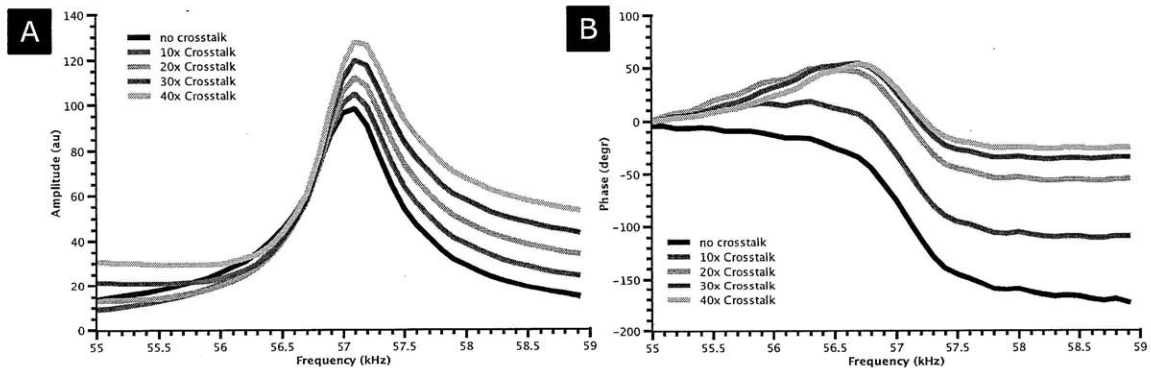
Figure 3-7: Simulated swept sine A) magnitude and B) phase response of the active cantilever using the sensing resistor readout and heater actuation. The individual traces represent different cross-coupling gains. Simulations with gains 30 and 40 show qualitatively the same behavior as in Figure 3-5D.

It is proposed that the crosstalk between the thermal actuator and the sensing resistor is due to a superposition of the input signal onto the resistor bridge signal (see Figure 3-6). The behavior of the cantilever is modeled during the swept sine measurement by simulating the cantilever dynamics with LabVIEW Simulation Interface Toolkit (National Instruments). The resulting data is shown in Figure 3-7. The individual lines represent simulations with different crosstalk gains. With zero gain ($K = 0$) in the crosstalk block, the amplitude and

the phase behavior is that of a harmonic oscillator. As the crosstalk gain is increased, the starting amplitude shifts up and the phase increases, sharply decreases, then flattens out with a final phase lag of less than 180°. This behavior is most pronounced in the curves with crosstalk gain at 30 and 40, which appear very similar to the tuning curve in Figure 3-5D when using the thermal actuator and the resistor sensor.[2] We therefore conclude that the reduced phase and amplitude transition is an artifact from the measurement. Although it is not necessary for imaging, this measurement error could be compensated electronically to obtain higher sensitivity.

3.3.4 Low frequency–High frequency Coupling

In regular feedback operation, the thermal actuator will be used for both exciting the cantilever in resonance as well as applying the feedback signal for topography. Any coupling between the low frequency signals used for topography tracking and the high frequency sinusoidal command used to resonate the cantilever can result in a distortion of the detection or even instability of the feedback loop. In this section, coupling is characterized between low frequency (topography tracking) and high frequency (resonance drive) components present in the cantilever deflection command signal, and by modeling this effect, a workaround is suggested.

Figure 3-8 shows the influence of a low frequency signal added to the thermal actuator on the mean value, the amplitude and the phase of the cantilever oscillating in resonance. For these experiments, the cantilever is driven with an input voltage, $V = A\sin(\omega t) + B(t)$, that consists of a high frequency sinusoidal component, added to a low frequency offset voltage. The cantilever's oscillation amplitude, phase, and mean oscillation amplitude value (also called *tapping mode deflection*) are measured optically using a digital lock-in amplifier (Nanoscope V). These measurements were repeated with different sinusoidal excitation amplitudes ($A = \{100\ mV, 200\ mV, 400\ mV, 800\ mV, 1600\ mV, 3200\ mV\}$).

Figure 3-8A shows the frequency spectra of an active cantilever driven with thermal actuation at different oscillation amplitudes (here the offset term is held fixed at $B = 5\ V$,

---

[2]The absolute value of the gain in this simulation does not describe the direct coupling in the actual device, because the simulation does not take into account gains from the heater, bimorph, or cantilever. A crosstalk gain is therefore physically possible.
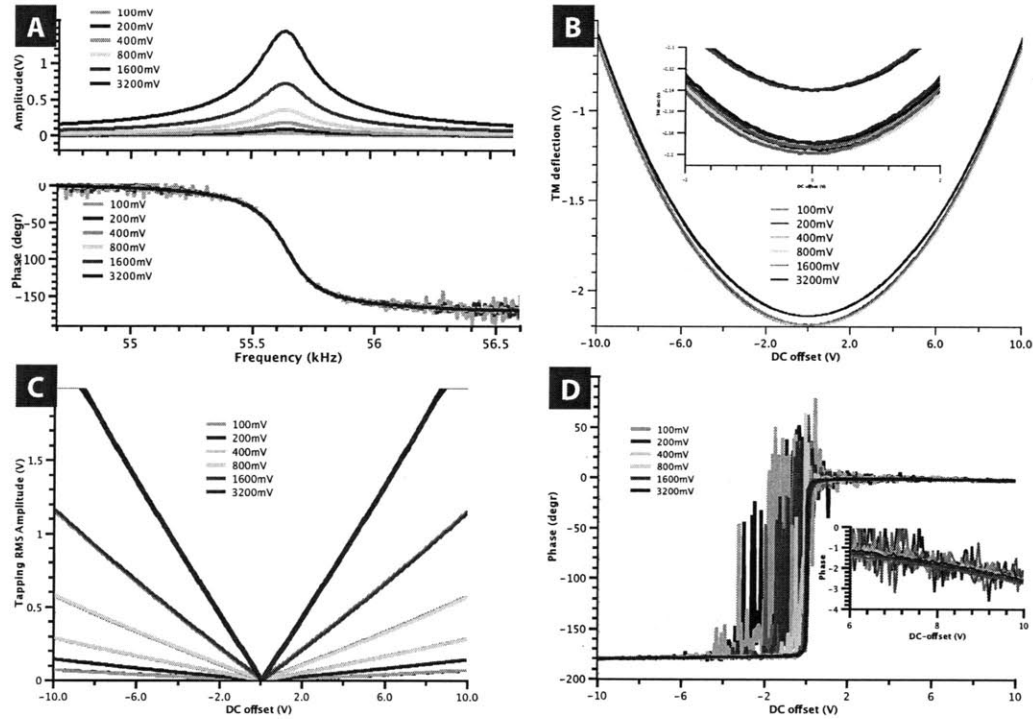
Figure 3-8: Influence of DC offset on AC behavior. A) Frequency sweep of cantilever measured with laser and driven by thermal actuator at multiple drive amplitudes. B) Tapping mode deflection as function of DC offset. The DC offset is ramped from -10 to $10\ V$ and the mean value of the oscillating cantilever is measured. (Insert is zoom in around zero DC voltage). C) RMS amplitude of oscillating cantilever as function of DC offset. D) Phase of cantilever oscillation as function of DC-offset. (Insert shows flat region between 6 and $10\ V$.)

and deflection is readout with the laser/photodiode). The amplitude response of the active cantilever scales with the sinusoidal drive amplitude as expected.

For the experiments in Figures 3-8B–D, the offset term is ramped with a $1\ Hz$, $10\ V$ triangular wave (*i.e.* $B(t) = 10\,\mathrm{tri}(2\pi t)$). Figure 3-8B shows the expected parabolic behavior of the static deflection on the applied voltage as the deflection is determined by the heat generated according to $P = V^2/R$. The tapping mode deflection does not change significantly as the amplitude is increased from $100\ mV$ to $1600\ mV$. Raising the amplitude to $3200\ mV$ results in an additional deflection of $0.06\ V$. This graph shows the inherent nonlinearity of the thermal actuator. Up to $1600\ mV$ drive amplitude, the actuator sensitivity does not change significantly with drive amplitude. At $3200\ mV$ the deflection shift with

drive amplitude manifests as a lower actuator sensitivity which has to be taken into account when measuring absolute topography data.

Figure 3-8C shows the tapping RMS amplitude as a function of the offset voltage. The measured amplitude is highly dependent on the offset signal applied to the actuator. In addition, the coupling is dependent on the drive amplitude with a coupling constant between 0.01 for 100 mV drive amplitude and 0.225 for 3200 mV drive amplitude. In most AFM applications, the tapping amplitude is used as a measure for the surface topography, and therefore this coupling is problematic. Since the coupling appears linear with the offset voltage, this effect could be compensated in the feedback controller. Another way to feedback on the topography is using the tapping mode phase as the sensor signal. Figure 3-8D shows the change in phase for different offset voltages. The phase curve is the same for all drive amplitudes and only changes strongly around the zero offset value due to noise in the phase detection (because of the low resonance amplitudes at low offset voltages, see Figure 3-8A). The phase signal above 1 V DC offset is nearly constant (less than 0.5 degrees per V) with respect to the DC voltage. This makes the phase signal a better choice for feedback than the amplitude with these actuated cantilevers. However, phase signals are often much noisier, especially with low drive amplitudes.

We can describe the coupling between the low frequency offset voltage and the oscillation amplitude by calculating the cantilever deflection $d(t)$ resulting from an applied voltage $V(t)$. Since the thermal actuator bends as a result of heating, the deflection of the cantilever will be proportional to the power dissipated $P(t)$.

$$
\begin{aligned}
d(t) &\propto P(t) \\
P(t) &= \frac{V(t)^2}{R}, \qquad \text{with } V(t) = A\sin(\omega t) + B \\
P(t) &= \frac{A^2}{R}\sin^2(\omega t) + \frac{2AB}{R}\sin(\omega t) + \frac{B^2}{R} \\
P(t) &= \frac{A^2}{2R}(1 - \cos(2\omega t)) + \frac{2AB}{R}\sin(\omega t) + \frac{B^2}{R}
\end{aligned}
\tag{3.3}
$$

Where Equation (3.3) makes use of the double-angle trigonometric identity.[3] This describes

---

[3]Also note that because the low frequency voltage-displacement relationship is not one-to-one (see Figure 3-3A), the applied voltage to the thermal actuator must include an offset term such that the applied

the deflection of the thermally-actuated cantilever as a function of the applied voltage frequency, amplitude and offset. Convolving the expression for dissipated power with a transfer function representing the bimorph effect (from applied power to deflection) yields an equation for the deflection.

$$d(t) \;=\; \left(\underbrace{\frac{2AB}{R}\sin(\omega t)}_{(1)} - \underbrace{\frac{A^2}{2R}\cos(2\omega t)}_{(2)} + \underbrace{\frac{A^2/2 + B^2}{R}}_{(3)} \right) \otimes h(t) \tag{3.4}$$

$P(t)$...electrical power $\qquad\qquad$ $V(t)$...drive voltage $(= A\sin(\omega t) + B)$

R.....thermal actuator resistance $\qquad$ A.....drive amplitude voltage

ω.....drive frequency $\qquad\qquad\qquad$ B.....DC-offset voltage

$d(t)$...cantilever deflection $\qquad\qquad$ $h(t)$...mechanical transfer function

Equation (3.4) accounts for the four parts of Figure 3-8. In particular, we note the coefficients of the three terms and begin to see the effect of applied voltage amplitude A and offset B on cantilever deflection when sinusoidally actuated. Specifically, Figure 3-8A, which shows that the amplitude of the magnitude response near resonance is a linear function of the drive amplitude A, can be seen mathematically in term 1 of Equation (3.4). (When driven near ω_n, only term 1 excites the cantilever.) Also in term 1, it is noted that the drive amplitude is a linear function of the offset term. This is shown in part C of Figure 3-8. This term also explains the phase response in part D of Figure 3-8: the phase experiences a 180° transition due to the change in sign of the offset.

From term 3, deflection amplitude is shown to be a quadratic function of the offset, which explains the behavior shown in part B of Figure 3-8.

Of particular interest is the argument of the cosine in the term 2. Recall that for accurate imaging, the actuator that tracks topography should be linear with applied voltage. In conventional AFM, topography is followed by the extension of the piezo tube, and recreation of the topography relies on a linear voltage-to-extension transfer function. If we are to use the integrated thermal actuator to track topography, it must be also exhibit a linear response for accurate imaging. Driving the active cantilever at its resonant frequency with

---

voltage is never negative as this negative voltage would cause positive deflection. (Not crossing the 0 V point avoids a rectifying nonlinearity which introduces unnecessary complexity.)

a command signal that is also at the resonant frequency will reveal all of the nonlinearities shown in Figure 3-8. Instead, the second term in Equation (3.4) implies that when driven at half the resonant frequency, the cantilever will not be influenced by the offset term used to track topography. Therefore, the offset can be modulated to track topography faster than is possible with conventional actuators and still produce accurate images. We can generalize Equation (3.4) to the case where the offset term is used to follow topography.

$$d(t,\omega) \;=\; \left(\frac{2AB(t)}{R}\sin(\omega t) - \frac{A^2}{2R}\cos(2\omega t) + \frac{A^2/2 + B(t)^2}{R}\right) \otimes h(t) \qquad (3.5)$$
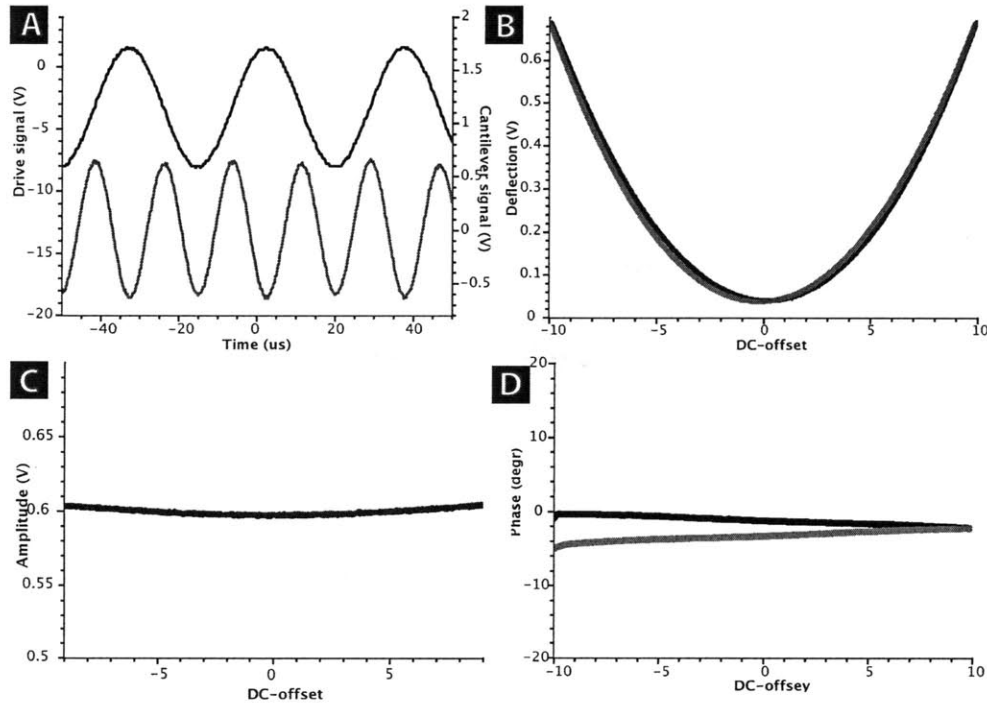
Figure 3-9: Influence of DC offset on AC behavior when driven at half the resonant frequency. A) Time domain signals. The excitation signal is shown on top, and the response on the bottom. B) Tapping mode deflection as function of DC offset. The DC offset is linearly ramped from -10 to $10\ V$ and the mean value of the oscillating cantilever is measured. C) Tapping amplitude as function of DC voltage. D) Tapping phase as a function of DC voltage.

As long as $B(t)$ has no spectral components in the vicinity of ω_n or $\omega_n/2$, the feedback signal will not disturb the amplitude of the cantilever oscillating at resonance when driven with a signal of frequency $\omega_n/2$. To demonstrate this, Figure 3-8 is recreated with the

actuation at $\omega_n/2$ and shown in Figure 3-9. Time domain drive and response signals are shown in Figure 3-9A, and the same quadratic dependence of tapping amplitude on offset is shown in part B (term 3 of Equation (3.4) is not drive frequency-dependent). Importantly, Figure 3-9C shows a flat response for the relationship between tapping amplitude and DC offset—*i.e.* the DC offset term does not affect the tapping amplitude, and this permits topography tracking with these active cantilevers. The phase response is shown for completeness in part D of Figure 3-9 and also shows very little deviation, because term 1 of Equation (3.4) does not influence the phase response when driven at $\omega_n/2$.

In practical implementation, using either the phase signal for feedback or exciting the cantilever at $\omega_n/2$ will simplify the control scheme significantly. However, most commercial AFM controllers measure the tapping amplitude with a lock-in amplifier around the excitation frequency and will therefore not detect the resonance at ω_n when exciting at $\omega_n/2$. Imaging with active cantilevers may require more flexible lock-in amplifiers.

3.4 Model-Based Thermal Compensation

Active cantilever step responses shown in Figure 3-3 demonstrate a response that is too slow to meet the targeted high speed imaging objectives. In order to alleviate this behavior, a compensator is designed from a frequency domain model obtained by system identification techniques.

3.4.1 Actuator Dynamics Characterization

In order to characterize the cantilever dynamics up to (but not including[4]) the first resonant mode with sufficient spectral resolution, a custom system identification program is written for data acquisition and analysis in LabVIEW (National Instruments). A band-limited random binary signal of $\{0, 1\}$ V is applied to the thermal actuator, providing a rapid means to gather wide-band frequency data with sufficient spectral resolution (a swept sine approach would yield too much data for tractable processing and subsequent parameterization).

---

[4]The purpose of this system identification effort is to characterize the cantilever response in the frequency band over which mean deflection will track topographic changes, see Equation (3.1), and not to characterize the resonance behavior. Measurements of the resonance modes are provided in Figures 3-4 and 3-5.

The cantilever deflection $d(k)$ is recorded with the optical lever sensor, and the input signal $V(k)$ is retained for processing (k is the discretized time variable corresponding to a sample rate of $f_s = 200\ kHz$). Means are subtracted from the input and output signals to remove DC offsets and facilitate linear system identification. The input autocorrelation $R_{VV}(\tau)$ and input–output cross-correlation $R_{Vd}(\tau)$ is computed from

$$
\begin{aligned}
R_{VV} &= \frac{1}{N} \sum_{k=0}^{N-\tau-1} V(k+\tau)V(k) \\
R_{Vd} &= \frac{1}{N} \sum_{k=min(\tau,0)}^{N-max(\tau,0)-1} d(k+\tau)V(k)
\end{aligned}
$$

Note that number of data points available to compute R_{VV} and R_{Vd} decreases as the lag τ increases, causing the correlations to be biased in regions of small signal overlap, and when converted to the frequency domain, causes spectral leakage. To minimize this effect, a Hanning window $w(\tau)$ is applied such that the weighted correlations approach zero for large lag. Longer window lengths reduce bias because more of the signals overlap. However, a given data record that is divided into fewer, longer windows reduce the number of estimates of $H(e^{j\omega})$, which are then averaged together, increasing the variance of the frequency estimation. We found that window lengths of approximately 5% of the sample record balances bias with spectral variance.

The windowed correlations, $R_{VV}w(\tau)$ and $R_{Vd}w(\tau)$ are converted into spectral densities through Fourier transforms, Φ_{VV} and Φ_{Vd}. The cross-spectral density is divided by the auto-spectral density to give a nonparametric frequency domain model.

$$
H(e^{j\omega}) = \frac{d(e^{j\omega})}{V(e^{j\omega})} = \frac{\Phi_{Vd}(e^{j\omega})}{\Phi_{VV}(e^{j\omega})} \tag{3.6}
$$

This method of finding $H(e^{j\omega})$ reduces the influence of noise and other effects not associated with the system input-output behavior, because it minimizes outputs not correlated to the input [65].

The model obtained in Equation (3.6) is parameterized using nonlinear minimization techniques to fit the coefficients of an Output-Error model. The order of the model is

selected using the Minimum Description Length principle [82]. The parameterized model of the active cantilever from thermal actuator voltage to deflection is:

$$H(s) = \frac{d(s)}{V(s)} = \frac{1,560(s + 95,900)}{(s + 1,465)(s + 684,100)} \tag{3.7}$$

Note that while the gain depends on laser spot alignment, Wheatstone bridge amplification, heater resistance and other factors, our experience with several cantilevers indicate that the pole and zero locations are repeatable over time. Additionally, we found that these pole and zero locations vary minimally among the different cantilevers tested.

Model validation is performed by comparing the dominant pole determined with system identification techniques at $1,465 \ s^{-1}$ to the time constant fit to the step responses $1,503 \ s^{-1}$ (Figure 3-3B). This agreement in low frequency behavior indicates that dynamics in this range are dominated by a single pole we attribute to heating and bimoprh actuation of the cantilever deflection. Once the cantilever dynamics are satisfactorily modeled, an open-loop filter or *thermal compensator* is designed (see Figure 3-11 for a block diagram of the system with thermal compensation).

3.4.2 Compensator Design for Increased Bandwidth

In order to compensate for the relatively slow dynamics identified in Section 3.4.1, and facilitate AFM image reconstruction from scaled controller outputs, an open-loop model-based compensator is used. This open-loop approach is similar to conventional AFM operation in which it is assumed that the z actuation (typically the piezo tube extension) behaves linearly up to its resonance, and reconstructing topography is then an inversion of the actuator's scalar transfer function (i.e., the gain from applied voltage to extension). In order to facilitate AFM image reconstruction from scaled controller outputs, actuator transfer functions should be constant in magnitude over the frequency range of operation. Here, we design the compensator to extend the constant magnitude region of the frequency response to frequencies higher than typical piezo tubes. For the active cantilevers described, actuation bandwidth is targeted at 10 kHz.

A model-based open-loop compensator is designed using loop shaping techniques such
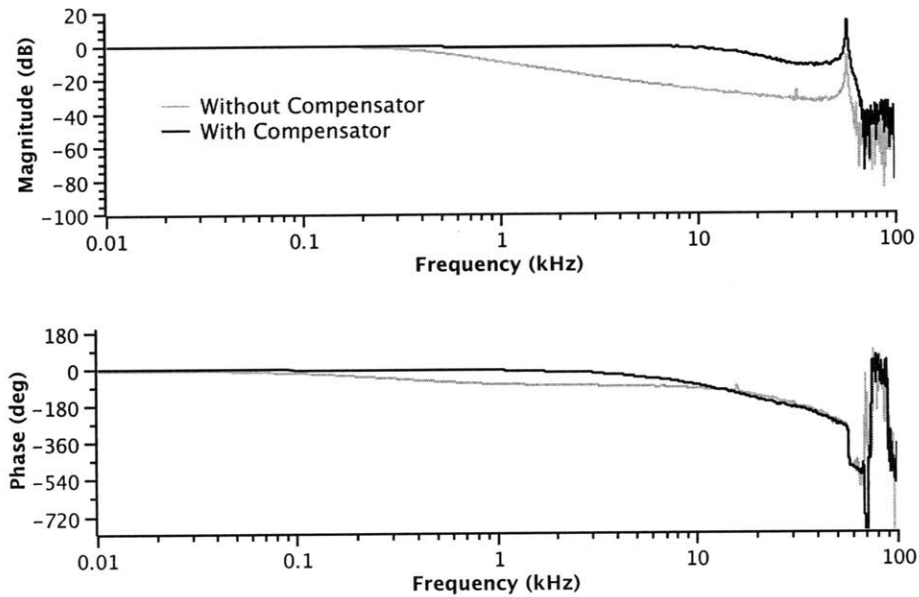
Figure 3-10: Frequency response of the thermally-driven cantilever with and without compensation. Deflection is measured with the AFM laser and photodiode. Compensation provides a flat frequency response up to 10 kHz.

that actuator frequency response is flat in magnitude and has minimal phase lag up to the actuation bandwidth. Additional high frequency poles are added for realizability and noise rejection, and the compensator transfer function is discretized using a standard bilinear transformation. The compensator is implemented on an FPGA at 100 kHz loop rate using the Digital Filter Design Toolkit for LabVIEW (National Instruments).

The measured frequency response of the thermal actuator with and without compensation is shown in Figure 3-10. Bandwidth of the thermal actuation is increased from approximately 0.4 kHz to 11 kHz, using 3 dB criterion. This increase in actuator bandwidth observed here is necessary for accurate imaging at reasonable rates. When we tried increasing the actuator response further, we observed unacceptable noise performance and output saturation of the FPGA due to high compensator gain in the passband. Further increases in actuator performance will likely require a inner loop feedback structure where the issue of realtime mean cantilever measurement is addressed.

Because our thermal actuator drive electronics conservatively limit cantilever deflection

to 750 nm, the piezo tube actuator is required for larger displacements necessary to cover topographic variation or sample tilt. Therefore, a feedback control strategy that separates controller outputs to two actuators is required and described in the following section.

3.4.3 Segmented Control

In order to take advantage of the thermal actuator's high bandwidth and circumvent its limited range, a segmented control strategy is employed to separate controller outputs. The output of the controller is filtered such that high frequency, low amplitude signals are directed to the thermal actuator and low frequency, large amplitude signals are sent to the piezo tube. In this manner, a single controller can be used, reducing complexity and minimizing the number of free parameters that must be tuned for imaging. Refer to Figure 3-11 for a block diagram of the system used for imaging.

To construct an image from the controller outputs, the signals sent to the two actuators (V_a and V_b in Figure 3-11) must be appropriately scaled and combined. This requires identification of the actuator transfer functions from applied voltage to displacement ($G_{V_a\delta}$ and $G_{V_b\delta}$). The z piezo transfer function is easily obtained through standard AFM calibration procedures that typically involve imaging a known standard, providing $G_{V_b\delta}$. To obtain $G_{V_a\delta}$, the cantilever is brought in contact with the sample, and the piezo is extended by a known amount to calibrate the laser and photodiode. Finally, with the sample retracted, voltage is applied to the thermal actuator V_a and the mean cantilever deflection is recorded from the photodiode.[5]

More sophisticated dual-input, single-output (DISO) control strategies have been extensively developed in hard disk drive head servo systems, and may be applicable here [54]. More recently, DISO controllers are being explored in AFM imaging and have demonstrated improvements in imaging speed (see [27] for a recent review). The method used here is similar to commercially available dual-stage AFM controllers (e.g. Veeco FastScan capability) and is sufficient to demonstrate the principle. Future work will focus on adapting more sophisticated approaches to the present work.

---

[5]The mean cantilever deflection $D = \langle d \rangle$, changes with applied voltage V_a, but because the sample is retracted and piezo extension does not influence the cantilever ($z = 0$), the transfer function to δ is obtained (see Figure 3-11).
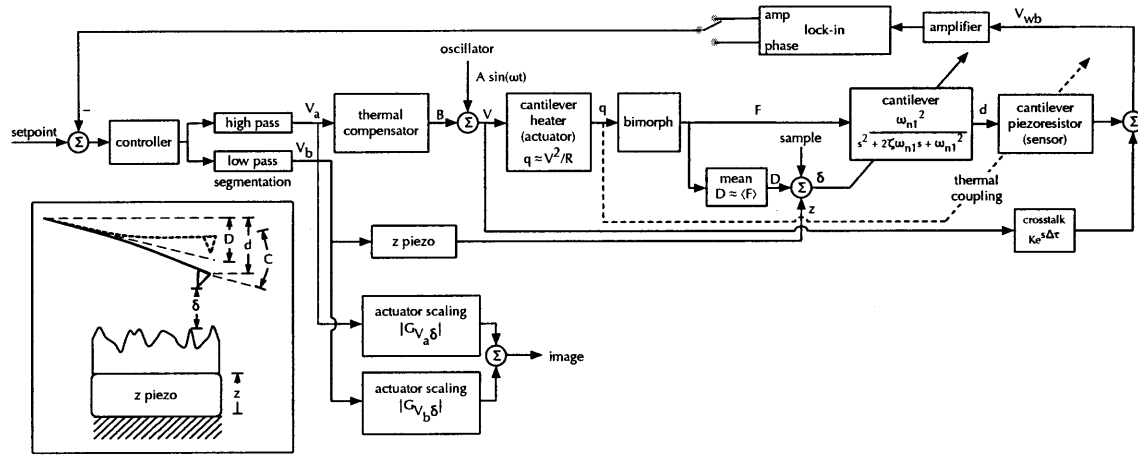
ω......tapping frequency

$\Delta\tau$.... crosstalk delay

V......heater input voltage $(V = A\sin(\omega t) + B)$

$G_{V_a\delta}$...thermal actuator transfer function

$G_{V_b\delta}$...z piezo transfer function

C..... cantilever oscillation amplitude

V_{wb}....Wheatstone bridge readout voltage

ω_{n1}...first resonant frequency

K.... crosstalk gain

F.... bimorph force

d.....cantilever deflection

D.... mean cantilever deflection

δ.....tip-sample distance

R.... heater resistance

Figure 3-11: Block diagram describing the relationship between all the components.

The segmented control approach allows separation of the displacement duties of the imaging system into tasks for which the respective actuators are best suited. In this manner, high frequency commands are processed by the thermal actuator and large displacements are tracked with the piezo tube, and this will ultimately enable higher imaging rates from systems with active cantilevers.

3.5 Discussion

Using actuated and self-sensing cantilevers investigated in this chapter reveal several differentiating aspects from the cantilevers generally used in AFM. The combination of actuation and sensing integrated into one MEMS device without requiring additional hardware such as lasers or piezos allows for the use of AFM in many more areas than conventional AFM.[6] The high integration density of the cantilevers however adds additional aspects that have

---

[6]For a recent paper where these cantilevers were used in liquid at rapid scan speeds, see [39].
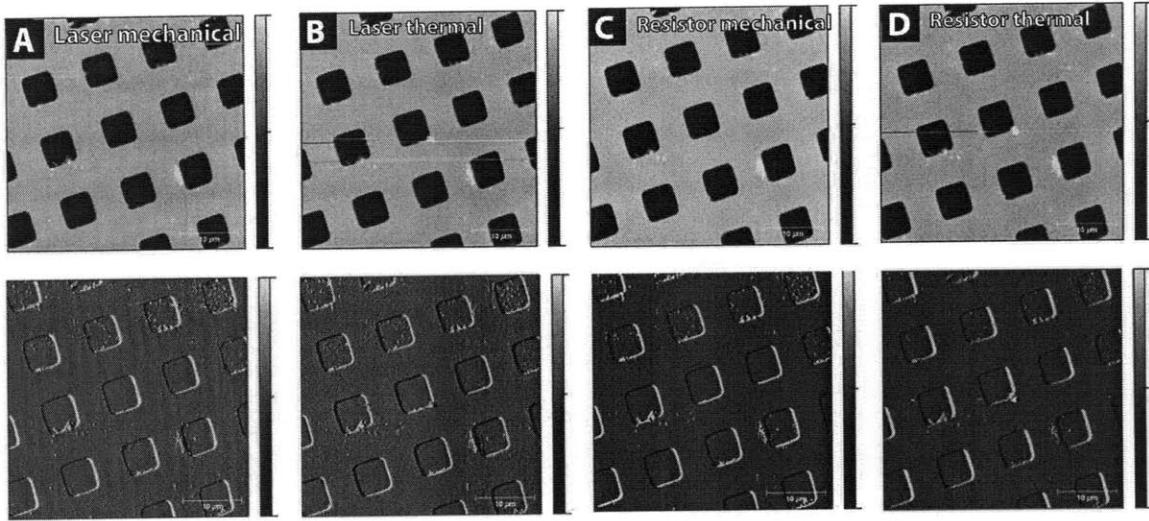
Figure 3-12: Image quality dependent on sensor/actuator combination. A) sensor: laser, actuator: mechanical (standard AFM configuration). B) sensor: laser, actuator: thermal. C) sensor: resistor, actuator: mechanical. D) sensor: resistor, actuator: thermal

to be taken into account when using these cantilevers for high quality and high speed AFM applications. Figure 3-11 shows the block diagram of the system describing the cantilever dynamics, crosstalk, coupling and feedback schemes.

As described in the measurements in Section 3.3 and Figure 3-12A, the cantilevers can be used in regular AFM mode with mechanical tapping actuation and laser readout. In addition, images with good quality can be achieved using any combination of traditional methods and the resistor readout and the thermal tapping actuation (Figure 3-12B-D). This is consistent with the tuning behaviors of Figure 3-5A-C which are very similar to each other. Even though the tuning curves in Figure 3-5D are fundamentally different, using both the thermal tapping actuator and the resistive readout showed no significant decrease in image quality on the calibration gratings (see Figure 3-12D)[7]. The z-feedback actuation in these images is done using the regular piezo tube.

It should be noted here however, that due to the relative large size (110 μm wide and 320 μm long) and short tip height (3–5 μm), significant damping of the cantilever oscillation occurs due to displacing the air between the cantilever and the surface. This results in very

---

[7]We use a calibration grating to have a standardized sample to compare the performance with other measurements. However a sample with smaller topography might show more differences in the behavior using the different actuation and sensing schemes.

low Q factors of the cantilever oscillation near the surface ($Q \approx 20$) and reduced sensitivity to surface features but increased speed performance (as can be seen in Figure 3-13). This is apparent when the scanning speed is stepwise increased from one line per second in Figure 3-12D to 78 lines per second in Figure 3-13. Figure 3-13D shows distortions in the image due to the use of a conventional 130 μm tube scanner for x, y and z motion.

Using the integrated thermal actuator for z-feedback actuation however proved to be more challenging. In this case, the thermal coupling between the feedback signal applied to the thermal actuator and the actual amplitude with which the cantilever oscillates (see Figure 3-8 and the thermal coupling in Figure 3-11) results in a more complex situation for approach and feedback control. This effect has been also observed for instrumented accelerometers by Ferrari *et al.* and Corman *et al.* [23, 40]. Ferrari *et al.* propose an active electronic compensation on the piezoresistor signal. Following an equivalent approach in case of the thermally driven AFM cantilevers could be implemented by subtracting a scaled and phase shifted signal to counteract the crosstalk block in Figure 3-11 ($Ke^{s\Delta\tau}$). This compensation circuit would have to be tuned for each cantilever (since the coupling is not equally strong due to manufacturing differences). Corman *et al.* counteract this crosstalk by exciting the accelerometer in *burst*-mode, where they switch between excitation and detection sequentially. It would be more difficult to adapt this method for use in AFM applications, since this requires a relatively high Q oscillator and increases the required detection time.

In addition, we only use 750 nm of thermal actuation (of the 2–3 μm predicted to be possible) due to a fixed current limit added in series with the thermal actuator to prevent it from failure via excessive heat. This makes imaging samples with larger topography variations with only the actuated cantilever impossible. To circumvent this problem, the segmented control scheme described in Section 3.4.3 is used, whereby the thermally-driven cantilever is used to track sample topography, and oscillated near resonance with the piezo integrated into the cantilever holder. This should be distinguished from other experiments discussed earlier in this section where control is performed over the z piezo only, and the cantilever oscillated thermally or with the integrated cantilever holder piezo. For the large changes in topography, we use a conventional piezo tube for very low frequency tracking of
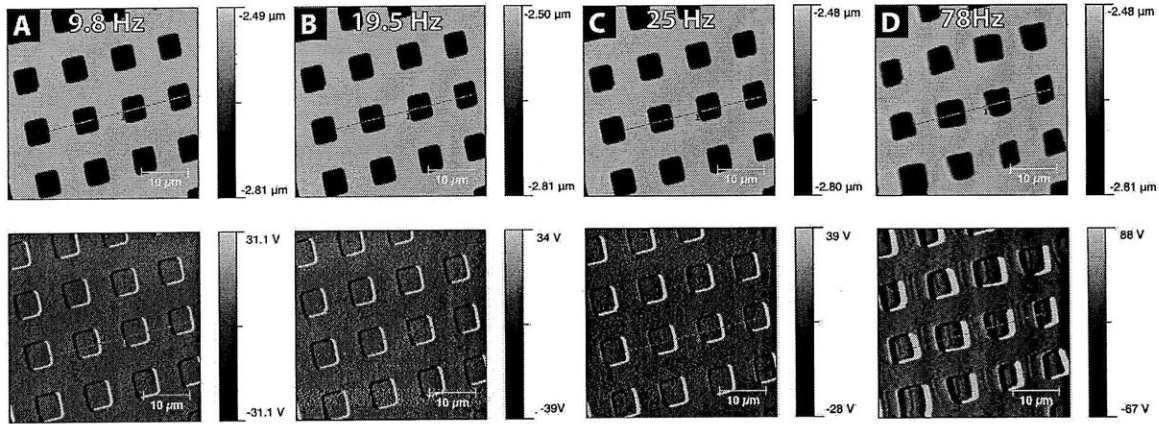
Figure 3-13: Quality of AFM image in tapping mode at different scanspeeds. A) 9.8 Hz linerate, B) 19.5 Hz linerate, C) 25 Hz linerate and D) 78 Hz linerate.

the sample topography. For this purpose, the feedback signal coming from the PID controller is low-pass filtered at as low as 10 mHz and applied to the scanner (the segmentation part in Figure 3-11).

A 4 μm scan of a 1 μm–pitch silicon grating is imaged at 4 Hz line rate, and scan lines from the image are shown in Figure 3-14 with a section of the image inset. The image is created by linearly combining the outputs of the high-pass and low-pass filters, scaled by the inverse of the actuator transfer function gains (see Figure 3-11). With the thermal compensator in the loop, controller gains are tuned to provide the best tracking (and further increased slightly to induce borderline oscillatory behavior). The upper two-thirds of the inset figure is taken with the compensator in the loop, then the compensator is bypassed, resulting in large amplitude oscillations and destabilizing the feedback loop. This illustrates the stability improvement of the closed loop system under thermal actuator compensation due to increased phase margin shown in Figure 3-10.

Examining scan lines with and without the thermal compensator demonstrates that the uncompensated actuator with the lower phase margin causes the feedback loop to destabilize with large amplitude oscillations at $f_1 = 175$ Hz, while the compensated actuator shows only minor ringing beginning $f_2 = 524$ Hz.

As shown in Figure 3-9, the problem with coupling between the lower frequency feedback signal and the tapping amplitude signal can be circumvented by exiting the cantilever with
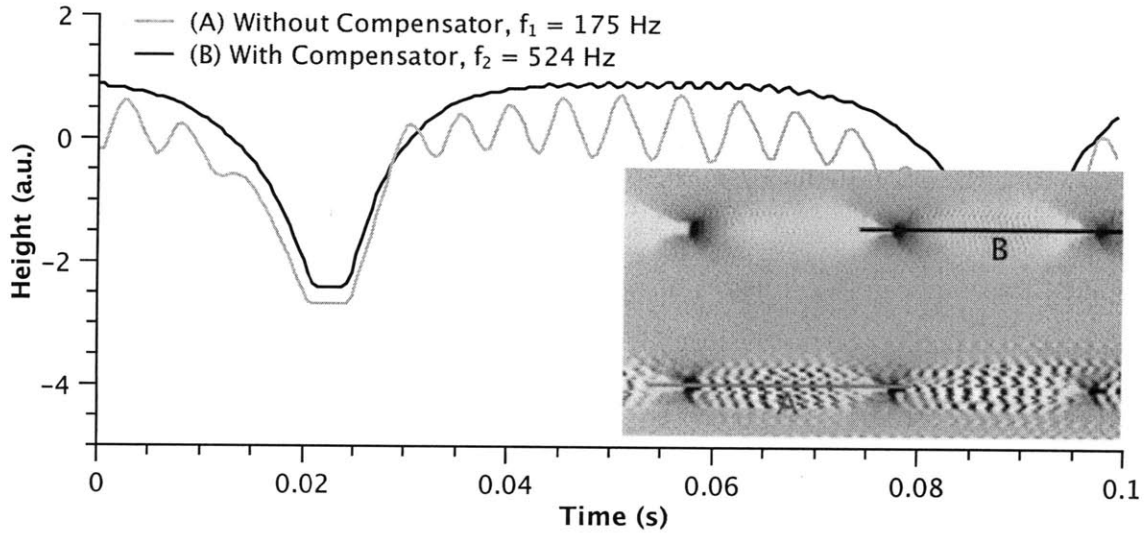
Figure 3-14: Scan lines taken during imaging demonstrate increased stability of the thermal actuator under compensation. For the same imaging parameters (controller gains, scan speed, etc.) the frequency of parasitic oscillation is increased from 175 Hz to 524 Hz and the amplitude is dramatically reduced, indicating better closed-loop stability margins. Inset: AFM image from which the scan lines are taken.

a signal at half of its resonant frequency. A higher driving amplitude is necessary to excite the cantilever in this mode than when driving directly at the resonant frequency, this corresponds well with the derived formula in Equation (3.4). However, we were not able to test this mode of operation during imaging due to limitations in our AFM controller. An additional lock-in amplifier which locks in on double the drive frequency would be required for feedback in this mode. An alternative is to excite the cantilever at its resonant frequency and perform the feedback over the phase rather than the amplitude, which is a common feature in most recent AFM controllers.

3.6 Conclusions

In this chapter we have investigated fully actuated and self sensing cantilevers for their mechanical and electrical characteristics as well as their controllability use in tapping mode Atomic Force Microscopy. It is found that the cantilevers can be successfully used for high resolution and high speed imaging, however several issues have to be taken into account to utilize the cantilevers full potential. One such issue is the crosstalk of the tapping drive signal

and the deflection signal measured with the integrated resistor which distorts the measured amplitude and frequency response used for topography feedback. This crosstalk can be minimized by feeding back on the tapping phase signal or by compensating electronically. When using the integrated actuator for feedback actuation as well as tapping actuation, the amplitude of the resulting cantilever osculation depends linearly on the applied feedback signal. Two ways are identified to prevent this effect from generating distortions in the image or instabilities of the feedback loop: exciting the cantilever oscillation with a sine signal at half the resonant frequency of the cantilever, or feeding back on the tapping phase rather than the tapping amplitude. Using a model-based compensator, actuation bandwidth is increased from 0.4 kHz to 11 kHz, which is essential for high speed AFM imaging. The achievable cantilever deflection was enough to image samples with low topography variations, but for samples with large height changes, a second, slow actuator extends the range significantly without impairing speed performance. Overall, it is shown that the self-sensing and self-actuated cantilevers are very promising for extending the capabilities of AFM in terms of imaging speed and increased usability. This technology is expected to help transform AFM from a tool used in research setting or high tech industry to use in everyday quality control and clinical diagnostics.

Chapter 4

Lateral Resonance Detection and Compensation

4.1 Introduction

Shortly after its invention by Binnig and Quate [9], the atomic force microscope (AFM) became a vital tool in the study of micro and nanoscopic features and has since demonstrated its usefulness through many important scientific contributions. Its unique ability to record extremely high resolution images without regard to sample conductivity and its ability to be operated at standard laboratory temperatures and pressures distinguish it from other imaging techniques such as electron microscopy. Direct imaging of nanoscale features on living biological samples are routinely performed (see Figure 4-1). Recently, the AFM has been used in molecular biology as a tool to study interactions between single molecules [13, 45, 76], and it continues to facilitate discoveries in the semiconductor, MEMS and life science fields [80, 59, 63, 60]

As progress in molecular biology and nanotechnology continues, demand for rapid and high quality image acquisition has increased to the point where the limitations of AFM imaging become impediments to further discovery [17, 18]. Many biological processes of interest occur on time scales faster than the imaging capability of conventional AFMs [5, 96], which are typically limited to image acquisition rates on the order of minutes [22]. Increasing the imaging rates of commercial AFMs enables new experimental observations, which in turn
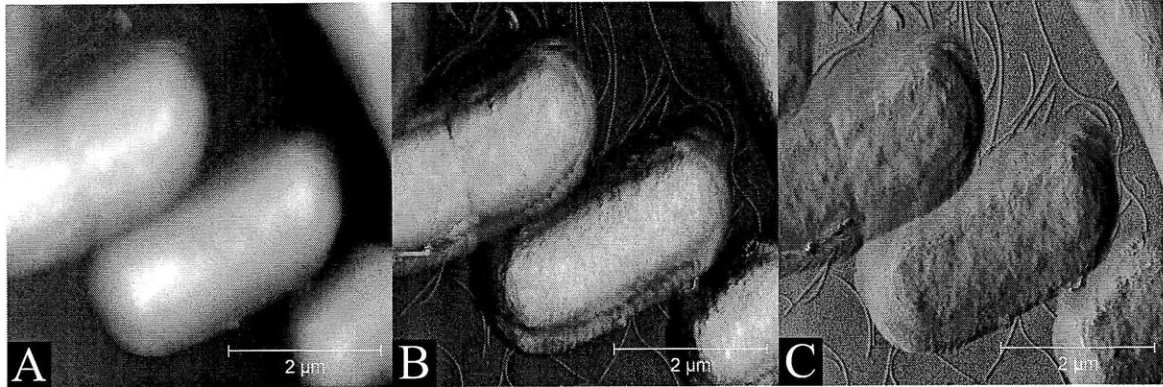
Figure 4-1: AFM is capable of high resolution imagery at the nanoscale as shown in the (A) topography, (B) phase and (C) error images of *e.coli*. But this image, taken in liquid in tapping mode at 2 lines/second, required several minutes to obtain, making observation of cellular dynamics difficult. Figure courtesy G. E. Fantner.

can lead to new discovery [36]. However, operating standard AFMs at higher scan rates by increasing the frequency of the commanded input signals, excite resonances in the lateral (in-plane) axes of the scanner that lead to image artifacts (see Figure 4-2).

Effective strategies for addressing the source of the resonances have been proposed [101, 26], and typically rely on input shaping or filtering the command signals using feedforward model inversion [25, 22, 98], or robust or optimal control [91, 29, 31, 30, 24]. While these approaches have demonstrated marked improvement in the performance of the nanopositioning system and have lead to higher imaging speeds, the difficulty in designing and implementing these approaches have kept the benefit out of reach of routine users of the microscope. In particular, these model-based approaches require direct measurement of the scanner lateral dynamics via external sensors (very few AFMs have lateral sensing), and a dedicated system identification experiment in order to develop a model that informs the compensator design [90]. To date, the specialized knowledge required to dismantle the microscope to access the lateral scan directions, perform a system identification experiment, and design and implement a model-based filter has restricted the applicability of this approach to those AFM operators experienced with system dynamics and controls.

This chapter presents a novel way to indirectly identify the dynamics of the scanner without requiring modification of the microscope or performing a separate system identification experiment, and uses the characterization to automatically shape the commanded input
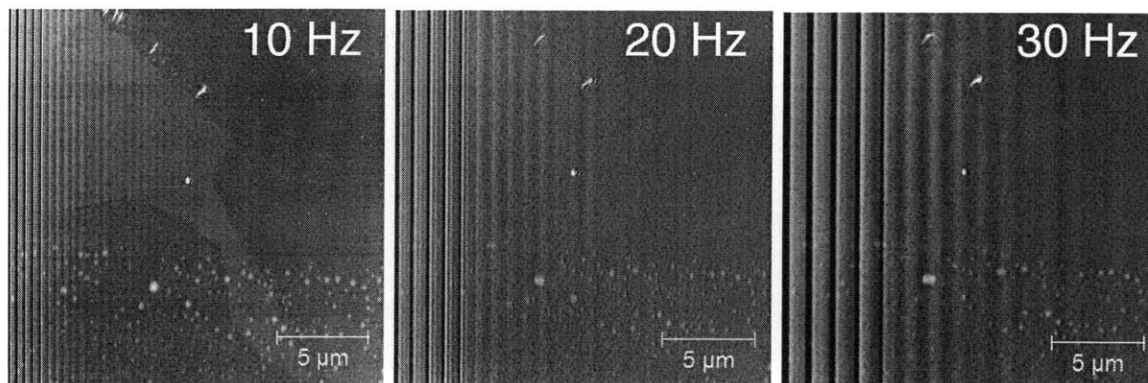
Figure 4-2: As the scan rate is increased from 10 lines/sec to 30 lines/sec, the lateral scanner resonances disturb the sample positioning and introduce more prominent banding or striping artifacts via dynamic coupling between the lateral and vertical positioning axes. The disturbances cover a large portion of the image at 10 lines/second, and completely overwhelm the underlying topographical information at 30 lines/second. These deflection images are taken with a Veeco AFM consisting of a 'Type J' piezo tube scanner (lateral range 125 μm) and a NanoScope IIIa controller.

signals such that the disturbing resonances are not excited. Because the lateral scanner dynamics can be quickly measured without the associated penalty of previous approaches, a just-in-time strategy of characterization allows the design of aggressive model-inversion filters that do not have to accommodate the wide variability of possible dynamics traditionally associated with robust control. This indirect scanner characterization has also enabled an iterative compensation method whereby secondary disturbing effects (*i.e.*, from higher scanner vibrational modes) are compensated in the feedforward filter after the effect of the primary source is eliminated. Further, this automatic identification and compensation approach has the potential to be implemented on the majority of existing commercial microscopes via only software updates, so that the dramatic improvement in imaging rates can be realized by non-expert users and without hardware modification of most AFMs.

The rest of this chapter is organized as follows: Section 4.2 describes the main components of the AFM and how the signals required for characterization and filtering are processed. Section 4.3 presents a model of the scanner dynamics and the algorithm for automatically identifying those dynamics. The compensator design strategy, including a novel iterative approach is described in Section 4.4. Section 4.5 includes results of the automatic compensator applied to a commercial system, and Section 4.6 discusses various aspects of

the approach including a strategy to deal with the pathological case of topography that masks as scanner disturbances.

4.2   System Description

An atomic force microscope has three main components as shown in Figure 4-3A. The piezoelectric tube actuator is fixed at the bottom to the frame of the microscope and the top end is free and allows three-dimensional motion of the sample relative to the probe.[1] The tube is quartered axially into four sections to allow for the bending that provides the displacement in the x- and y-directions, and an additional full cylindrical section of the tube provides z extension. Amplifiers provide the high voltage necessary to actuate the piezo tube. The sample is placed on the free end of the tube. Above the sample, a flexible cantilever is mounted to a small piezo stack actuator for oscillating the cantilever near its resonance (or one of its harmonics in advanced imaging modes). The end of the cantilever is fabricated with a sharp probe, which interacts with the sample and causes the cantilever to deflect. This deflection is measured by a laser and photosensitive diode.

The topography image is generated based on how the tube is commanded to extend in the vertical direction, z, in order to hold some property of the cantilever constant (commonly static deflection for so-called "contact mode," RMS oscillation amplitude or phase relative to the tapping piezo excitation signal in "intermittent contact mode"). And often the error signal in that feedback loop, e, is also plotted in order to capture high spatial frequencies (sample details measured by the probe but not tracked by the feedback system). Strictly speaking, the images typically generated are $z(x_d, y_d)$ and $e(x_d, y_d)$ where $x_d(t)$ and $y_d(t)$ are the desired triangular-shaped command signals applied to the piezo, and for imaging it is assumed the actual displacement of the actuator tracks that reference signal.[2] When operating the AFM at higher scan speeds (e.g., $x_d(t) > 10\ Hz$ for typical piezo tubes), the actual displacement of the tube does not track the desired triangular shape due to

---

[1]This section describes a scanned-sample configuration of an AFM, however scanned-probe versions are also available, and the method described in this work applies equally well to either configuration.

[2]This description omits the hysteresis compensation that pre-warps the $x_d(t)$ and $y_d(t)$ scan command signals so that the actual tube displacement at low speed is triangular for undistorted imaging. Hysteresis effects are not scan speed dependent, and do not pertain to the scanner resonance issue emphasized herein.
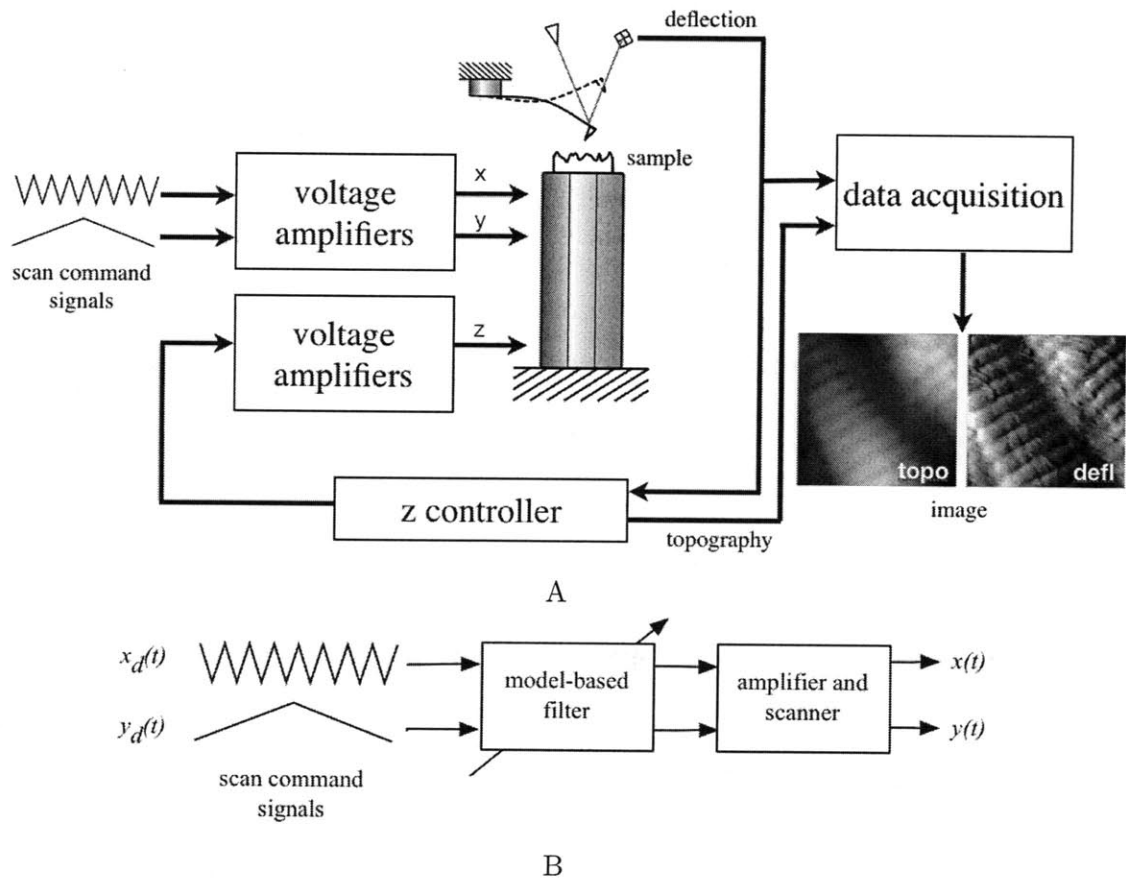
Figure 4-3: A. The principle components of a conventional scanned-sample atomic force microscope, consisting of (i) a piezo tube scanner, (ii) MEMS cantilever and optical lever detector, (iii) data acquisition system and (iv) feedback controller to regulate the tube extension. Triangular-shaped command signals are applied to the scanner in an open-loop fashion to achieve raster scanning. B. In this work, the scan command signals are filtered with a model-based input shaper implemented on an FPGA. This FPGA is programmed to implement a single-input, single-output difference equation with variable coefficients. By updating only the coefficients, the compensator can be reprogrammed without incurring the long compile time traditionally associated with FPGAs.

resonances that are excited in the tube.

In order to compensate for the natural tendency of the scanner to resonate, the scan command signals are processed by a model-based input shaper that implements an inversion of the scanner's lateral dynamics with suitable roll-off (see Figure 4-3B). The scanner dynamics are anticipated to vary with sample mass, experiment type, and over time as the environment of the piezo changes, so a reprogrammable filter is required for implementation. A field programmable gate array (FPGA) is selected for its ability to quickly process high speed signals (National Instruments, Austin, Texas, USA). However, compile times required for programming these devices are typically more than 20 minutes, which is not compatible with the rapid updates this automated method requires. To address this issue, a general filter structure is programmed once onto the FPGA that executes a single-input, single-output sixth order difference equation $G(z^{-1})$, where the full difference equation is factored into three second-order-sections, with each section implemented as a Direct-Form II structure [77].

$$G(z^{-1}) = K \prod_{j=1}^{3} 2^{g_j} \frac{b_{0j} + b_{1j} z^{-1} + b_{2j} z^{-2}}{1 + a_{1j} z^{-1} + a_{2j} z^{-2}} \qquad (4.1)$$

However, the coefficients (a_{ij}, b_{ij}) and gains (K, g_j) of this filter are left as variables that can be quickly updated via a network-connected computer. In this manner, recompiling the FPGA is avoided, and the filter equation can be updated in only a few milliseconds.

For the stated problem of lateral resonance identification and compensation, additional consideration should be made of the (x, y) positioning system. The lateral positioning system in most AFMs is open loop, because direct measurement of scanner displacement is cumbersome and expensive, and calibration of slow speed effects (*i.e.,* hysteresis) is usually effective for practical operation. However, at high speed, triangular scan command signals excite vibrations in the piezo tube, which cause poor tracking of the assumed triangular shape (Figure 4-4A) and distort the deflection image (Figure 4-4B). In particular, the Fourier components associated with the sharp turnaround of triangle wave scanning excite scanner resonances.[3] As can be seen in Figure 4-4, the lateral resonance (measured directly

---

[3]This realization has lead to some researchers to build microscopes based on sinusoidal scanning [49],
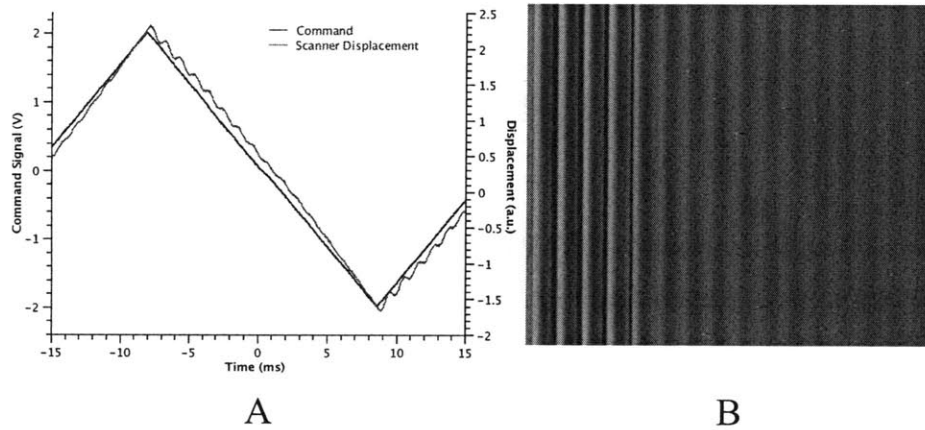
Figure 4-4: A. When scanning at higher rates, Fourier components associated with the sharp features of the triangle command signals excite lateral scanner resonances. Directly measuring the scanner lateral displacement (obtained here using an external interferometer) show that the response of the scanner follows the triangle wave with an additional sinusoidal response. B. The small amount of ringing shown at the left strongly couples into the vertical axis as repetitive disturbances that manifest as streaks over the deflection image, which is shown at the right. Both subfigures were acquired using a Veeco 'Type J' piezo tube scanner at 30 Hz line rate.

in Fig. 4-4A) couples into the vertical axis and is detected by the cantilever deflection signal (Fig. 4-4B), making this disturbance appear as topographic features. If the z feedback control bandwidth is high enough, the piezotube will attempt to track this plant output disturbance, and the same artifacts will corrupt the topography signal as well—making this a disturbance that corrupts both the deflection and topography images. For the present work, the deflection signal is measured with an external data acquisition system (USB-6251, National Instruments, Inc., TX, USA) and processed with a minimal system identification algorithm using MATLAB (The Mathworks, Inc., Natick, MA).

It is the realization that the coupled nature of the scanner allows detection of lateral disturbances through the deflection signal that enables the characterization algorithm described in the next section.

---

however that approach comes at the expense of preferred constant velocity scanning in which the most spatial details are detected by the cantilever [19]. Additionally, the aim of this work is to be broadly applicable and enable a user-independent means of addressing scanner distortion, and toward that end, a solution that filters the triangle command signals inherent to all existing commercial systems is preferred.

4.3   Scanner Model and Identification Algorithm

4.3.1   Modeling Scanner Coupling

As mentioned in the previous section, the essential consequence of lateral positioning distur-bances is observed through the cantilever deflection signal.[4] Coupling exists in the scanner whereby in-plane distortions disturb the out-of-plane direction. This coupling can originate from two primary sources: (i) through topographic variation or (ii) dynamic coupling of scanner. The primary source of coupling is the latter, while the former could be a minor contributor, as follows: If the topography of the sample is parameterized by a height vari-able z as a function of the lateral position (x, y), then any disturbances in x and y will be measured through the slope of the topography.

$$z(x + \Delta x, y + \Delta y) \quad = \quad z(x,y) + \frac{1}{k!}\frac{\partial^k z}{\partial x^k}\bigg|_{x+\Delta x}(\Delta x) + \frac{1}{k!}\frac{\partial^k z}{\partial y^k}\bigg|_{y+\Delta y}(\Delta y) \qquad (4.2)$$

Or just considering the disturbance as a positioning error:

$$\Delta z \quad = \quad z(x + \Delta x, y + \Delta y) - z(x,y) \qquad (4.3)$$
$$= \quad \frac{1}{k!}\frac{\partial^k z}{\partial x^k}\bigg|_{x+\Delta x}(\Delta x) + \frac{1}{k!}\frac{\partial^k z}{\partial y^k}\bigg|_{y+\Delta y}(\Delta y) \qquad (4.4)$$

which can be interpreted as the difference in the height of the topography between the assumed position (x, y) and the disturbed position $(x + \Delta x, y + \Delta y)$. The scanner position-ing errors cause the probe to interact with a different location on the sample, and if the topography has large enough slope such that the change in height is on the order of the lateral positioning error, then the (x, y) resonances will cause a measurable disturbance in the z direction, and hence lateral disturbances couple into the vertical direction.

The more prominent source of lateral disturbance, however, stems from the dynamic coupling inherent to the positioning actuator—in other words, lateral ringing is measurable in the vertical direction by virtue of the fact that the piezotube positioning axes are not

---

[4]In contact mode imaging, the disturbance is sensed through the cantilever deflection, whereas in in-termittent contact mode operation, the disturbance is measured in the RMS amplitude signal (usually the magnitude output of the microscope's lock-in amplifier) provided the cantilever and subsequent RMS calcu-lation has sufficiently high bandwidth.
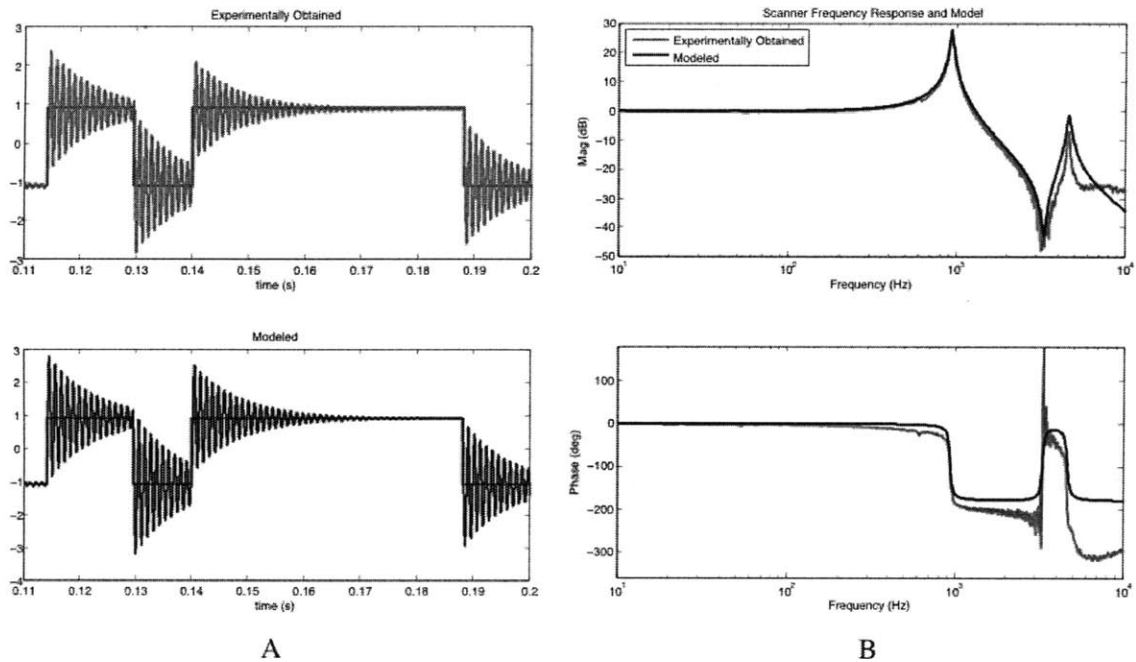
Figure 4-5: System Identification is performed on a Veeco "Type J" scanner. A. Time domain step response data is experimentally obtained (top) using an optical interferometer positioned to directly measure scanner displacement. This data is fit to a low order model and the same input is applied to the model for validation purposes (bottom). B. Frequency domain representation for both the experimentally measured scanner (red) and the model (black) showing 94% variance accounted for (VAF).

orthogonal [32]. In order to understand this coupling, a traditional system identification experiment is performed. In this experiment, the cantilever and optical components of an AFM were removed (MultiMode AFM, Veeco, CA), and an laser interferometer (SIOS, Ilmenau, Germany) is oriented to measure the lateral scanner displacement. The scanner's x direction is excited with a random series of binary inputs of -40 or 40 V applied to the piezo tube. Random binary input is a rapid means to excite all the dynamics in a linear time-invariant system and a complete model of the scanner dynamics can be obtained [65]. The results of the system identification experiment are shown Figure 4-5. The time domain measured step response is shown in Fig 4-5A (top), and in the frequency domain in Fig. 4-5B in red. By inspection, a low order model structure is selected, consisting of two pairs of

complex poles, and a pair of complex zeros, with a term to match the DC gain.

$$P(s) = \frac{\left(\frac{\omega_{p1}\omega_{p2}}{\omega_{z1}}\right)^2 \left(s^2 + 2\zeta_{z1}\omega_{z1}s + \omega_{z1}^2\right)}{\left(s^2 + 2\zeta_{p1}\omega_{p1}s + \omega_{p1}^2\right)\left(s^2 + 2\zeta_{p2}\omega_{p2}s + \omega_{p2}^2\right)} \tag{4.5}$$

When the coefficients of Equation (4.5) are fit to the non-parametric frequency response, the resulting low-order model accounts for 94% of the variance of the obtained data. The remaining unmodeled dynamics include a transmission delay (manifested as increased phase lag at high frequency), and a nonlinear spring-like effect associated with the second vibration mode. The resulting model step and frequency responses are plotted in Figures 4-5A (bottom) and B, respectively. The same input used for data acquisition (Fig. 4-5A (top)) is applied to the low order model (Fig. 4-5A (bottom)) as model validation. This selected model structure has proven to capture the dominant dynamics of all scanners we have encountered, including four types of tube scanners (Veeco Type J, E, BioScope, and Quesant Type 11) and many custom-built prototype flexure scanners developed for high speed applications [38].

The model structure in Equation (4.5) suggests a two-mass model where the applied force is non-collocated with the measured displacement. This model is shown in schematic form using lumped mass, spring and damper elements in Figure 4-6A. It is well known that piezo actuators relate charge to mechanical displacement, hence current to velocity, and therefore force to voltage. So assuming amplifier is a strong voltage source (*i.e.*, is not loaded by the capacitive nature of piezos at high frequencies) is equivalent to assuming an idealized force source—in other words, the modeling piezo-electric transduction effect is not required. The compensation strategy described later in this section, aims to keep the vibration modes of this model from being excited by shaping in the applied force, $F(t)$.

If coupling between the lateral x and vertical z directions are considered, the resulting lumped parameter model is shown is Figure 4-6B. A brief mathematical analysis of this model is provided in order to demonstrate the observability of the lateral resonance when measured with a vertical sensor. (Refer to Figure 4-6B for some parameter definitions, other
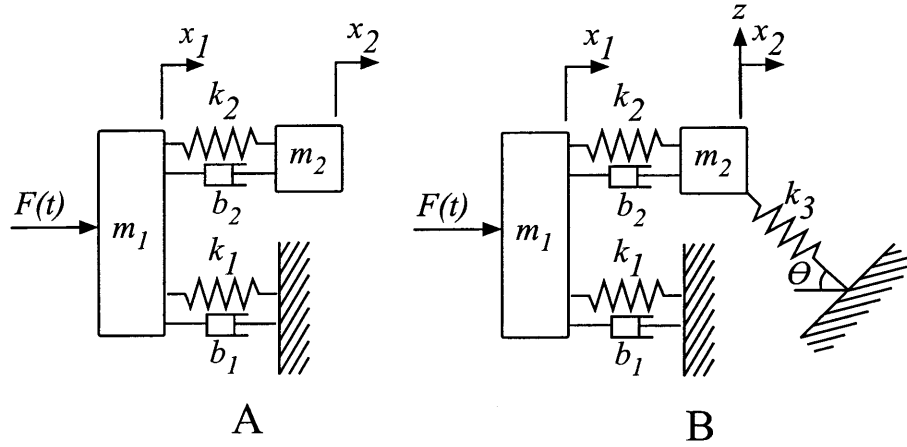
Figure 4-6: Lumped parameter model of the scanner coupling dynamics. A. Initial model of the single degree-of-freedom system based on the frequency response in Figure 4-5 (from input $F(t)$ to output $x_2(t)$). B. An additional element is added to capture coupling between the x and z axes.

notation is self-evident.)

$$m_1 \dot{v}_1 = F - k_2(x_1 - x_2) - b_2(v_1 - v_2) - k_1 x_1 - b_1 v_1$$

$$m_2 \dot{v}_2 = k_2(x_1 - x_2) + b_2(v_1 - v_2) - k_3 x_2 \cos(\theta)$$

$$m_2 \dot{z} = k_3 x_2 \sin(\theta) \tag{4.6}$$

It is convenient to gather into matricies.

$$
\begin{bmatrix} m_1 & 0 & 0 \\ 0 & m_2 & 0 \\ 0 & 0 & m_2 \end{bmatrix}
\begin{bmatrix} \ddot{x}_1 \\ \ddot{x}_2 \\ \ddot{z} \end{bmatrix}
=
\begin{bmatrix} 1 \\ 0 \\ 0 \end{bmatrix} F(t) -
\begin{bmatrix} k_1 + k_2 & -k_2 & 0 \\ -k_2 & k_2 + k_3 \cos(\theta) & 0 \\ 0 & 0 & -k_3 \sin(\theta) \end{bmatrix}
\begin{bmatrix} x_1 \\ x_2 \\ z \end{bmatrix}
$$

$$
-
\begin{bmatrix} b_1 + b_2 & -b_2 & 0 \\ -b_2 & b_2 & 0 \\ 0 & 0 & 0 \end{bmatrix}
\begin{bmatrix} \dot{x}_1 \\ \dot{x}_2 \\ \dot{z} \end{bmatrix}
$$

Using matrix notation, the previous equation can be expressed more compactly.

$$\mathbf{M}\dot{\mathbf{v}} = \mathbf{S}F(t) - \mathbf{K}\mathbf{x} - \mathbf{B}\mathbf{v} \tag{4.7}$$

So the state equations become

$$\dot{\mathbf{x}} = \mathbf{v} \tag{4.8}$$

$$\dot{\mathbf{v}} = \mathbf{M}^{-1}\mathbf{S}F(t) - \mathbf{M}^{-1}\mathbf{K}\mathbf{x} - \mathbf{M}^{-1}\mathbf{B}\mathbf{v}. \tag{4.9}$$

Expressed in traditional state space notation (where the number of states, n is 6):

$$\begin{bmatrix} \dot{\mathbf{x}} \\ \dot{\mathbf{v}} \end{bmatrix} = \underbrace{\begin{bmatrix} \mathbf{0}_{3\times 3} & \mathbf{I}_{3\times 3} \\ -\mathbf{M}^{-1}\mathbf{K} & -\mathbf{M}^{-1}\mathbf{B} \end{bmatrix}}_{\mathbf{A}} \begin{bmatrix} \mathbf{x} \\ \mathbf{v} \end{bmatrix} + \underbrace{\begin{bmatrix} \mathbf{0}_{3\times 1} \\ -\mathbf{M}^{-1}\mathbf{S} \end{bmatrix}}_{\mathbf{B}} F(t) \tag{4.10}$$

$$z = \underbrace{\begin{bmatrix} 0 & 0 & 1 & 0 & 0 & 0 \end{bmatrix}}_{\mathbf{C}} \begin{bmatrix} \mathbf{x} \\ \mathbf{v} \end{bmatrix} \tag{4.11}$$

In this form, the computation of the observability matrix is straightforward and we find that

$$\text{rank}(\mathbf{O}) = \text{rank}\left(\begin{bmatrix} \mathbf{C} \\ \mathbf{C}\mathbf{A} \\ \vdots \\ \mathbf{C}\mathbf{A}^5 \end{bmatrix}\right) \tag{4.12}$$

$$= 6. \tag{4.13}$$

So we see that the observability matrix is full rank and therefore the lateral resonances are indeed coupled into the z axis and measurable through the deflection sensor.

The modeling provided in this section demonstrates both good agreement with experiments, and a thorough understanding of the origin of the kind of disturbances exhibited in Figure 4-2. The low-order model of Equation (4.5) is sufficient to describe 94% of the variation in the frequency domain, and this model structure is found to be an effective structure for the basis of compensation, as will be discussed in Section 4.4. Moreover, since this lateral disturbance clearly couples into the vertical direction, an opportunity exists to indirectly measure the lateral dynamics, which is a prerequisite for the model-based com-

pensation strategy. Details of this sensor-less way to measure lateral dynamics is presented in the next section.

4.3.2 Minimal Identification Algorithm

Since an appropriate model structure is identified with high confidence, and it is realized that information about the lateral dynamics is observable in the deflection signal, the challenge becomes extracting enough information from the deflection signal to fit the parameters in Equation (4.5). This problem is difficult because the deflection signal includes information from multiple sources including (i) sample topography, (ii) controller artifacts (refer to Fig. 4-3A), (iii) sensor noise and nonlinearity, and (iv) scanner disturbances as described in Section 4.3.1. The problem requires isolating the latter from all other sources mixed into the deflection signal. Recently, other researchers have looked at extracting scanner dynamics from the image [21], however, these approaches require imaging a test sample with known regular spatial features, and since this necessarily requires imaging a different sample and therefore different scanned mass, the scanner dynamics will likely change.

If determination of all the parameters of Equation (4.5) is required, identification of lateral dynamics through the deflection signal might not be possible because both the input and output signals are not ideally suited to an information-complete system ID in the following ways: The input signal is a triangular waveform that does not strictly meet the persistence of excitation criteria [65]. And as mentioned above, the output signal is indirect, noisy, and mixed with other sources. However, if we allow a less-than-complete identification of Equation (4.5) (*i.e.,* identify only the parameters in that equation that are required for compensation), then the problem is solvable using the algorithm described below.

The following algorithm extracts from the deflection signal only the part due to the repetitive scanner resonances, and fits that signal to a low-order model. Refer to Figure 4-7A–F for a visual representation of the outcome of each of the following steps.

Step A. With the AFM scanning any sample fast enough to induce scanner resonances, K scanlines of trace and retrace data are recorded as individual vectors.

$$\begin{bmatrix} \vec{z}_1 & \cdots & \vec{z}_K \end{bmatrix} \tag{4.14}$$

Step B. These scanlines are separated into two sets: traces and retraces. (Fig. 4-7B and C shows only the set of trace data for clarity.)

$$\begin{bmatrix} \vec{z}_1 & \cdots & \vec{z}_P \end{bmatrix} \begin{bmatrix} \vec{z}_2 & \cdots & \vec{z}_{K-P} \end{bmatrix} \tag{4.15}$$

Step C. For both sets, the cross-correlation between adjacent scanlines is computed,

$$\forall \vec{z}_i$$

$$R_{z_i, z_{i+1}}(m) = \frac{1}{N} \sum_{n=0}^{N-m-1} z_{i,n+m} \cdot z_{i+1,n} \quad m \geq 0 \tag{4.16}$$

where m denotes correlation lag.

Step D. All the scanlines in both sets of cross-correlated data are averaged together, yielding one signal, $t(m)$.

$$t(m) = \frac{1}{K-1} \sum_{i=1}^{N-m-1} R_{z_i, z_{i+1}}(m) \quad m \geq 0 \tag{4.17}$$

Step E. The dominant frequency f_n of $t(m)$ is identified using a discrete-time Fourier transform. This frequency is used as the starting point for a nonlinear parameter estimator in Step F in order to avoid local minima and therefore erroneous convergence.

$$T(f) = \sum_{m=0}^{N-1} t(m) e^{-j2\pi f m/N} \tag{4.18}$$

$$f_n = \operatorname*{argmax}_{f} T(f) \tag{4.19}$$

Step F. Using f_n as an initial condition in the solution space, and bounding other parameters to positive, real values, the parameters of a damped sinusoid $s(m)$ are fit to $t(m)$.
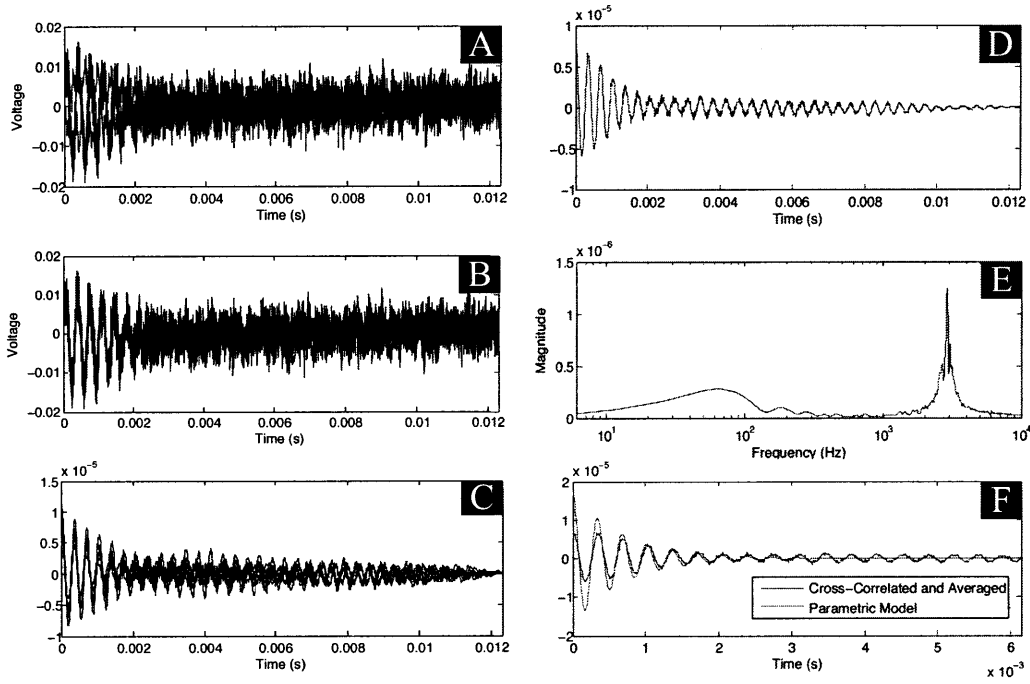
Figure 4-7: The output of each step in the minimal system identification algorithm. A. K trace and retrace signals overlaid. B. Only the trace signals overlaid. C. Trace signals cross-correlated. Notice that noise and topography influences are suppressed at this stage. D. The cross-correlated traces are averaged to yield a single, smoothed signal used for curve fitting. E. The dominant frequency from D is identified for use in the nonlinear minimization algorithm. E. Results from the curve fitting overlaid with the cross-correlated trace from D.

$$s(m) = Ae^{-2\pi f\zeta m} \cos(2\pi f\sqrt{1 - \zeta^2}m + \phi) \qquad (4.20)$$

$$\min_{A,f,\zeta,\phi} \sum_{m=0}^{N} (s(m) - t(m))^2 \qquad (4.21)$$

$$\longrightarrow \{A, f, \zeta, \phi\} \qquad (4.22)$$

The fitting methodology is Levenberg-Marquardt which is an algorithm designed to find the parameters that minimize a function, in this case the sum of squared error, Equation (4.21). This step yields the parameters (A, f, ζ, ϕ), which are the amplitude, undamped frequency, damping coefficient and phase of $s(m)$.

The outcome of the preceding algorithm are the time-domain coefficients of the dominant part of the frequency-domain model in Equation (4.5) (multiple identification iterations, discussed in Section 4.4, fit the equivalent of the full model given by Equation (4.5)). Early versions of this algorithm attempted to fit in the frequency domain directly, but proved to be less successful due to the lack of a frequency domain cross-correlation analog. Stated differently, the repetitive nature of the scanner disturbances scanline-to-scanline make them well suited to isolation via cross-correlation. The algorithm is successful because the disturbances are repetitive and synchronous and therefore correlated, whereas noise and topography generally are not correlated between scanlines. For the unusual case where this assumption of uncorrelated topography is not valid, and a useful workaround, see the discussion in Section 4.6.

Although the algorithm provides four parameters (A, f, ζ, ϕ), not all of these parameters are required for compensation, and relaxing the requirement for an information-complete estimation of the full system increases the likelihood that the minimal system ID experiment produces useful results in the presence of a strictly under-excited system whose output is measured indirectly. This method is denoted "minimal identification" to distinguish it from the traditional information-complete system identification that strives to account for the maximum variation in the recorded input-output data of an unknown system. By admitting a less-than-complete system description, a much less onerous experiment is required to identify lateral dynamics, while still providing sufficient information about the scanner to inform the design of a low-order model-based compensator.

Specifically, the amplitude A and phase ϕ of the input-output model $s(m)$ are not required for compensation—only the damped natural frequency ω_d and Q factor of the scanner resonance are needed, and therefore good estimation for only the undamped frequency f and the damping ratio ζ are used from this identification algorithm. Because this method has been shown to work despite the use of triangular waveforms as inputs (as opposed to the preferred step or impulse inputs), this minimal identification strategy can be performed while operating the AFM in its natural imaging state and without hardware modification. The outcome of this identification strategy is enough information (f and ζ for each iteration of the identification algorithm) to design model-based compensators, which is described in

the next section.

4.4   Compensation Strategy

As described in the previous section, information about the lateral dynamics of the scanner can be obtained from the image and used to build a minimal model that is sufficient for model-based compensation. This section describes the compensation strategy employed for mitigating scanner resonances.

The overall goal of the compensator is to ensure a flat magnitude response in the frequency domain through both the low frequency signals associated with the fundamental scan command signals and importantly, the higher frequencies associated with the scanner resonance. This ensures that the scanner trajectory is as close to triangular as possible, and therefore achieves constant velocity scanning through the majority of the scan area. The process of indirect scanner identification and subsequent compensator design can be applied iteratively, as described in below.

4.4.1   Iterative Identification and Compensation

Broadly, the compensation approach taken here is to identify the largest image disturbance with the indirect method described previously, attribute that disturbance to scanner resonances, and compensate via feedforward model inversion. Then, if scanner disturbances continue to corrupt the image (for example, from a higher mode or modeling errors in the first iteration) a second identification experiment is applied with the first feedforward filter running to identify residual scanner disturbances. That second disturbance is used to design an inversion compensator and appended to the that of the first. Practical considerations such as detectability constraints and FPGA resources have limited the effectiveness of the approach to two iterations. Details of controller structure for both iterations are as follows.

Information from the scanner resonance (specifically, the natural frequency f and the damping ratio ζ) is used to fit to the damped natural frequency ω_d and Q factor of a second-order resonator. This frequency domain model is then inverted so as to attenuate an equal amount of energy from the input signal as is amplified by the resonating scanner.

Additional high-frequency roll-off is added to the compensator to make the transfer function strictly proper and hence realizable by traditional causal filters.[5] Frequency responses of the modeled plant $P(s)$ (based on Equation (4.5)), the compensator $G(s)$, and the cascaded system $G(s)P(s)$, are shown in Figure 4-8A for the first iteration.

Should a second iteration be required (if for example, the higher mode at around 6 kHz be large enough in magnitude and Q factor so as to corrupt the image), another identification experiment is performed. The same underdamped sinusoid model is used, and the natural frequency and Q factor are identified. The poles of this second mode are inverted and appended to the compensator designed from the first iteration. High frequency roll-off is added to the compensator to make the compensator realizable, as shown in Figure 4-8B.

The continuous-time compensator is then converted to discrete time via bilinear transform and factored into second-order-sections for implementation on the FPGA. The outputs of this operation are the filter coefficients and gains necessary for execution (*i.e.,* the (a_{ij}, b_{ij}, g_j, K) terms from Equation (4.1)). Additionally, the a_{ij} coefficients set the pole locations in the complex z plane, which determines the filter's stability properties and therefore deserve consideration.

There are well-known stability implications for simple inversion-dynamics compensators that must be addressed. Specifically, inverting right half plane zeros that are characteristic of non-minimum phase systems results in unstable filters. However, these scanners necessarily must not exhibit non-minimum phase properties to satisfy open loop imaging performance. Otherwise, duplicate-imaging distortions would be present near the edges of the image as the scanner "doubled-back" on its scan path when the scan command signal changes directions. Piezotube scanners are designed not to exhibit this kind of distortion, and therefore inversion based compensators will not be unstable.

Lateral resonance cancellation via feedforward input shapers has proved effective at allowing higher imaging rates while maintaining image quality, see for example work by Schitter, Zou and El-Rifai [101, 25, 22, 91, 29]. Each of these methods may differ in the

---

[5]Commercial microscopes often include the option to "round" the scan command signals, which is equivalent to low-pass filtering . Historically, this method has not been effective as the Q factor of these scanners are often so high, that even low-pass filtering is not sufficient attenuation around the resonance to completely remove its effect.

A   B
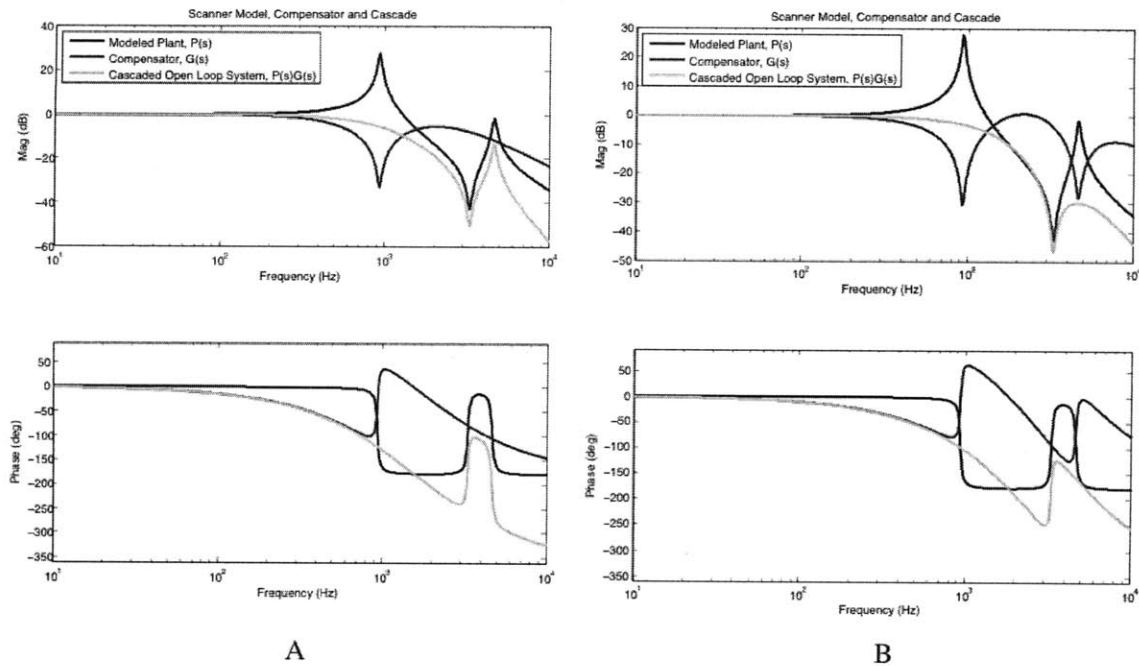
Figure 4-8: Frequency response plots used to visualize the compensator at both iterations, with the plant $P(s)$ shown in black, the compensator $G(s)$ in blue, and the cascaded system $G(s)P(s)$ shown in green. A. For the first iteration, the largest resonance is determined from the indirect system identification algorithm and simply inverted in a feedforward input shaping filter, with the addition of high frequency roll-off for realizability. B. During the second iteration, another mode is identified and appended to the compensator from the first iteration.

details of the controller design paradigm (*e.g.,* robust vs. optimal), but all are predicated on some model for the lateral scanner dynamics. For the situation where scanner dynamics vary (i) over time, (ii) with sample mass, or (iii) with experimental environment (humidity, imaging in air or liquid, etc.), these control strategies must make allowances for reasonable scanner variation, and typically tradeoff performance for robustness to parameter variation. The method presented here is simple in principle, but makes no such performance tradeoff— an up-to-date model of the scanner observed in the current experimental environment allows for high-performance compensators while still adequately suppressing the resonance.

4.4.2 Q Factor and Damping in Scanner Compensation

In order to understand the limits of compensation and when these scanner disturbances will be problematic for the user, it is helpful to decompose the triangular scan command signal $x_d(t)$ into Fourier components.

$$x_d(t) = \frac{8}{\pi^2} \sum_{n=1,3,5,\ldots}^{\infty} \frac{(-1)^{(n-1)/2}}{n^2} \sin\left(\frac{n\pi t}{L}\right) \tag{4.23}$$

Although the fundamental scan command frequency for unperturbed AFM imaging is typically around 2 Hz (*i.e.* $\pi/L \approx 2$), and the disturbances become apparent in the image at around 10 Hz (Fig. 4-2), the higher Fourier components present in triangle waveforms excite the main scanner resonance, which is around $f = 1000\ Hz$ (depending on the scanner type). For most implementations of commercial microscopes, it is common for there to be several hundred terms in Equation (4.23), so that the energy associated with the terms around 1000 Hz ($n \approx 300$) in the scan command signal excite the resonance.

In fact, scanner resonances are excited even at the low scan speeds of 2 Hz traditionally associated with non-distorted images (Fig. 4-9C). At low scan speeds, these disturbances do not pose an imaging problem because the amplitude of the disturbance has decayed before the first couple imaging points are obtained (Fig. 4-9D). This point highlights the importance of the Q factor in scanner design—a high Q factor is associated with low damping, which causes the scanner to ring for many periods once excited. According to Equation (4.20), the impulse response for these scanners is enveloped by a decaying exponential $B(t)$, and the decay rate is set by the natural frequency f and the Q factor as follows (Fig. 4-9A):

$$B(t) = Ae^{-2\pi f \zeta t} \tag{4.24}$$

$$= Ae^{-\frac{\pi f}{Q} t} \tag{4.25}$$

A high Q factor describes an oscillator that takes many periods to decay, and this lengthy ring-down causes distortions to appear in the image at lower than necessary scan speeds. It is the interaction between the scanner resonant frequency, the Q factor, and scan velocity

that determines whether distortion corrupts the image (Fig. 4-9A). It is the author's opinion that in SPM positioner design, too much attention is paid to simply increasing the frequency of the first resonance of the scanners at the expense of too little damping [53]. The resulting trend is very high resonance scanners with little damping that fundamentally limit lateral scanner performance. If there were simply more damping associated with the resonances in these SPM positioners, much of the present effort at mitigating their excitation would not be necessary.
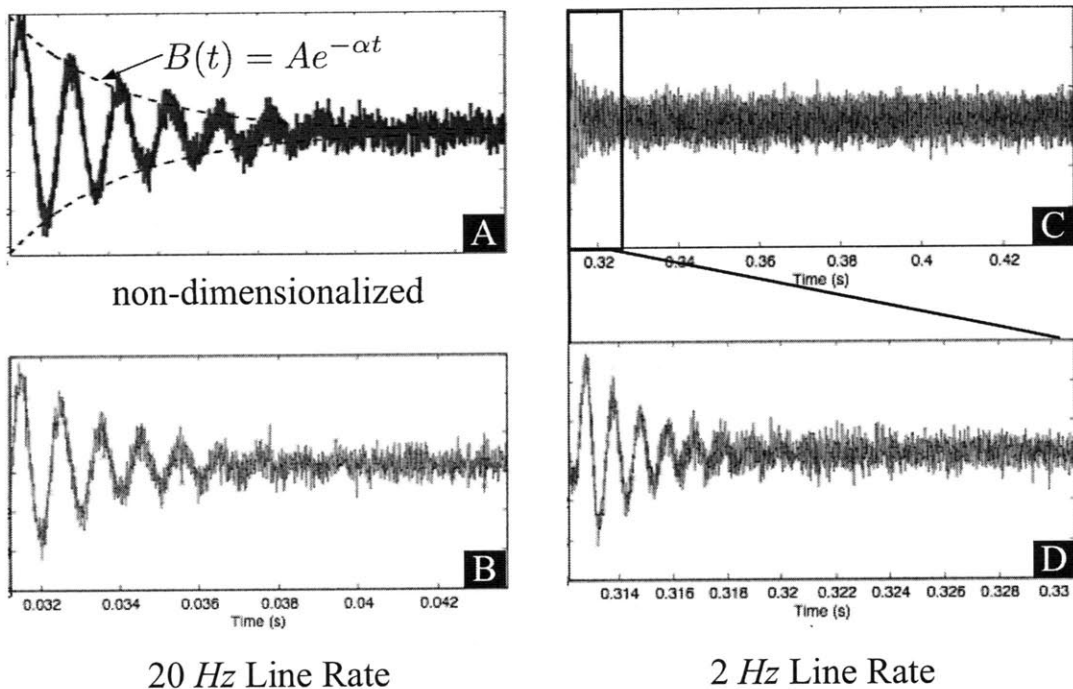
Figure 4-9: A. The impulse response for piezotube actuators demonstrate an underdamped response that rings according to the natural frequency f and Q factor. The enveloping function that describes the decay properties is $B(t) = Ae^{-\alpha t}$ where $\alpha = \pi f/Q$. This is a time-invariant property of the scanner and how this disturbance gets mapped into the image is then a function of the scan rate. B. For fast scan rates like 20 Hz, the disturbance can be a substantial fraction of the total scan line. C. For slower scan rates like 2 Hz, the impulse response is always excited, but is a smaller fraction of the scan line and will often decay before disrupting the image quality. D. Zooming in on the initial part of the scan line during slow scanning shows the scanner disturbance is still evident.

4.5   Results

Using the indirect identification procedure of Section 4.3.1 and the compensation strategy of Section 4.4, experimental data of the applied method is presented here, including compensation effectiveness in the lateral direction, and imaging results.

In order to demonstrate the effectiveness of the model inversion input shaping, a Veeco "Type J" piezo tube scanner is set to track triangular command signals with and without model inversion compensation. Displacement of the free end of the tube in the lateral direction is measured directly with an external laser interferometer. The results are shown in Figure 4-10 for a 40 Hz scan command signal (black). The natural response of the uncompensated displacement (red) shows excessive ringing, while the compensated version (blue) largely tracks a triangular shape. Note that the compensated version is shifted due to the sampling delay and group delay of the filter. While this delay manifests as a horizontal translation in the image, the amount is repeatable and can be pre-computed in the image plotting routines of the AFM control software without loss of data. Additionally, it is noted that the compensated blue signal exhibits a slight bowing due to piezo hysteresis, which was not attempted to be corrected with calibration for these experiments.

Whereas Figure 4-10 shows the effectiveness of model-based compensation directly measured in the lateral direction, the impact on high speed image quality must be ultimately demonstrated and is shown below. Figure 4-11 (top) shows an image where the full identification and subsequent compensation is automatically run. A scratch in mica is imaged at 30 Hz line rate using a Veeco "Type E" tube scanner, starting from the top of the frame and recording a left-to-right scan. Initially, scanner disturbances are larger than the topographic variation and overwhelm the image. At the top of the frame, the indirect system identification algorithm is initiated, and over several scanlines, a model of the resonating piezo tube is developed. The first itertion of a model inversion compensator is automatically designed and downloaded to the FPGA approximately 25% through the image. Once the compensator is applied, the imaging artifacts associated with scanner resonance no longer is apparent and nanometer-level precision is obtained at high scan rates. Section traces are extracted for comparison and shown in Figure 4-11 (bottom) and demonstrate removal of
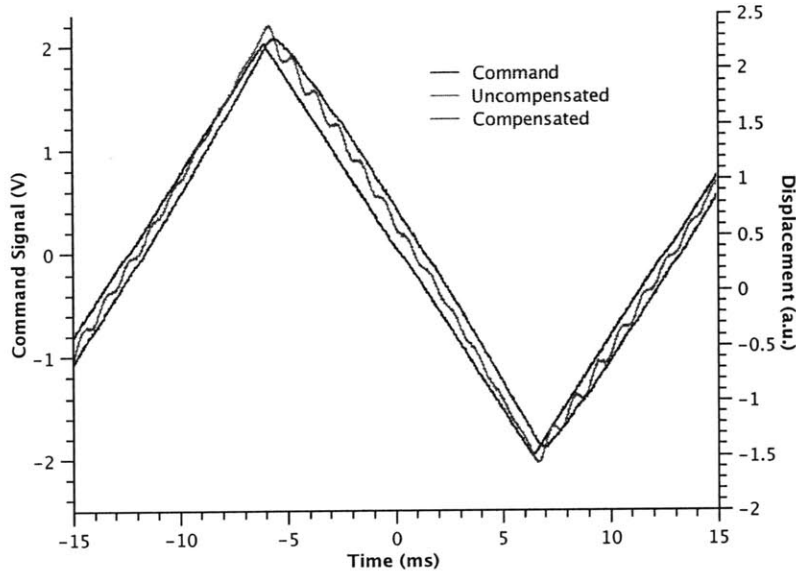
Figure 4-10: A Veeco "Type J" piezo tube scanner is commanded to track a 40 Hz triangle wave with and without feedforward compensation. Without compensation, excessive ringing causes substantial deviation from the desired triangular shape, while the compensated scanner shows no such effect. The sampling and group delays are evident as a shift in the compensated signal, but this effect is constant and can be undone with simple image translation.

the ringing in the out-of-plane z direction by filtering the x command signal. Again, the group delay of the filter is evident as a small shift in the image when the compensator is applied. The identification and compensation process shown in Figure 4-11 is completely automatic—no user interaction was required to achieve these imaging results.

As discussed in Section 4.4, the indirect identification of scanner dynamics enables real-time scanner characterization while configured for experimental operation (*i.e.* immediately before imaging). This low barrier to identification and ability to immediately shape input signals has opened the possibility for iterative compensation. Because the indirect method for characterization is not ideally suited for an information-complete system ID, perfect compensation is not always possible with one pass. In this situation, a first iteration at identification and compensation is applied and if the scanner continues to distort the image (due to modeling or identification errors, or the presence of a second mode not captured in the first pass) another iteration is applied. This is shown on atomically flat mica where the residual dynamics of a second mode is most apparent in Figure 4-12. In this experiment,
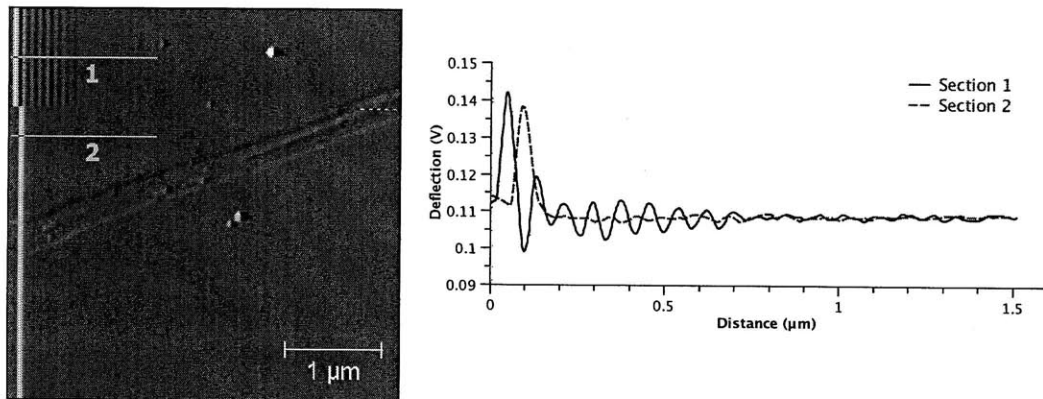
Figure 4-11: This deflection image (left) of scratched mica taken with a Veeco Type E scanner at 30 lines/second shows distortion during the first 25% of the image, while the indirect characterization and compensator design algorithm is running. However, once the feedforward filter is designed and downloaded to the FPGA, these distortions are eliminated. Section traces (right) show the result of compensating for the resonances on the deflection trace. Section 1 shows the resonance coupling into the z direction before compensation, whereas Section 2 shows this disturbance is largely avoided once compensation is applied. It is important to note that this identification and compensation process was applied completely automatically and without any involvement from the microscope operator.

data is taken at 30 lines/second using a Veeco "Type J" scanner. Deflection images are recorded with no compensation (Iter. 0), after the first iteration is applied (Iter. 1) and after the second iteration (Iter. 2), and improvements at both iterations are evident. The final image shows an irregular lower spatial frequency disturbance, which is attributed to optical interference from the multiple paths that laser light takes to the deflector (either reflecting from the cantilever or from the sample). It should be noted that this minor distortion is not observable without compensation because scanner resonance distortions dominate the topography; whereas with two iterations of compensation, previously negligible effects become limitations to image quality at high speed.

Image data shown in this section were taken without performing a separate full system identification experiment that is required with other approaches [22, 98, 91] and the compensator design and implementation is fully automatic. This novel detection approach has enabled a way to achieve fast scanning without loss of precision as demonstrated on mica samples, and places no assumption on the skill level of the microscope operator. In this
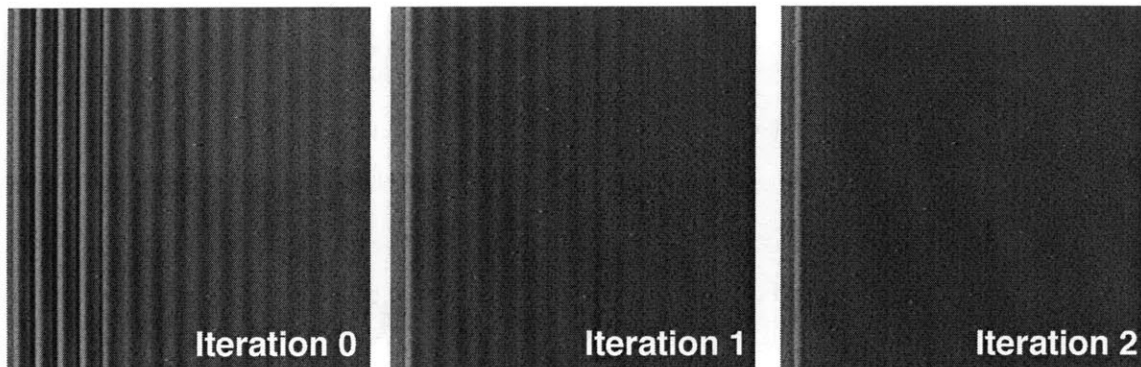
Figure 4-12: Iterative compensation is enabled by indirect scanner characterization as evident in these deflection images. Imaging mica at 30 Hz line rate, scanner resonance dominate the uncompensated image (Iter. 0), but are largely reduced after the first iteration (Iter. 1). A second pass at identifying residual scanner dynamics that corrupt the image reduces the distortions due to the scanner completely (Iter .2), revealing other sources of imaging error (in this case optical interference).

manner, rapid scanning is made available to a wide audience of researchers who can focus their attention on experiment design.

An additional benefit to the indirect characterization method is the ability to easily measure the scanner dynamics before imaging. This becomes important for extracting the most performance from the scanner as changes in sample mass and damping can influence compensator effectiveness. This topic is discussed in more detail in the next section.

4.6   Discussion

This section discusses the virtues of the indirect scanner characterization algorithm, and in particular the novel ability to perform a just-in-time style identification which allows the immediate design of aggressive compensators. Additionally, the fundamental assumption in the algorithm of uncorrelated sample topography is addressed, and in the case where it is found to be violated, a workaround is proposed.

4.6.1   Just-in-Time Scanner Characterization

One of the main obstacles to higher performance in lateral feedforward filters is the accommodations that must be made for scanner variation. In the case of robust control strategies,

a scanner model is obtained and used to solve the robust synthesis controller problem with attempts to anticipate all the ways in which the scanner dynamics can change and derive a single controller for the worst-case combination of parameter variation.

In the case of sampled-scanned microscopes, the mass of the sample and imaging medium (*i.e.* air or liquid) dramatically affects the scanner dynamics. The robust controller must accommodate all situations and often results in a conservative controller that roll-off actuator bandwidth before uncertain resonances can cause distortion. This ultimately impacts performance. Simple model inversion compensators do not suffer from this performance tradeoff, but are notoriously susceptible to modeling errors [25]. However, the indirect identification approach taken here provides up-to-date scanner information thereby reducing the likelihood of modeling errors and allows the use aggressive filters with good disturbance rejection properties.
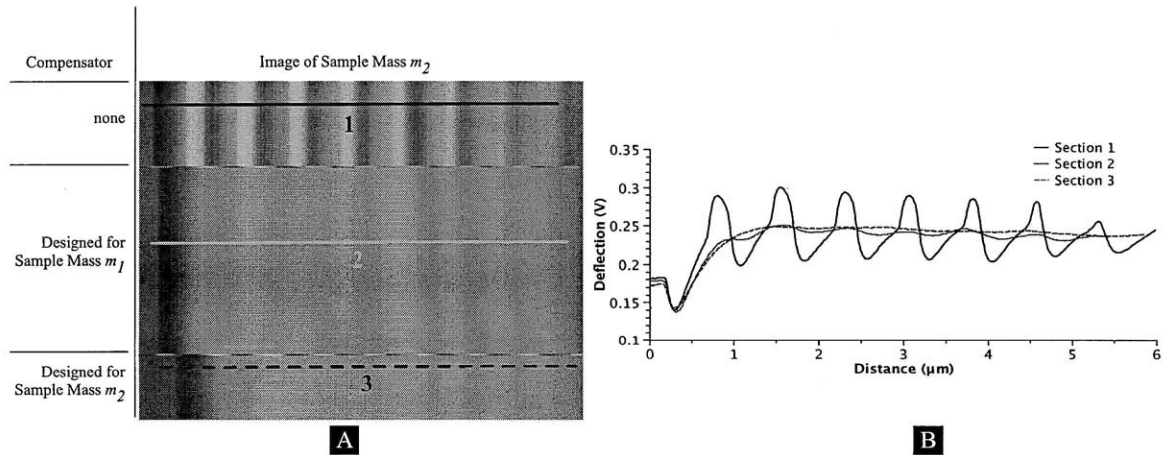
Figure 4-13: A. A sample with mass $m_2 = 1.5\ g$ is imaged with no compensator applied, a compensator designed for another sample $m_1 = 1.0\ g$, and a properly designed compensator. Only in the case where the compensator is specifically designed for the correct sample mass does good scanner resonance avoidance occur. B. Sections from the image show the high level of scanner rejection that is obtained at high speed when an appropriate compensator is used. (Note that the section traces have been shifted slightly to eliminate the influence of the filter's group delay and facilitate comparison.) This highlights the need for a system that can quickly identify the scanner dynamics in a just-in-time manner so that recent information is used in the compensator design.

In order to illustrate the need for up-to-date scanner information, consider the image data shown in Figure 4-13. Initially, a sample of mass $m_1 = 1.0\ g$ is loaded onto the

microscope and imaged at high speed so the indirect identification and compensator design algorithm can be run, and satisfactory compensation is achieved. The compensator used for m_1 is retained. Then another sample of mass $m_2 = 1.5$ g is loaded onto the microscope and a compensator for this mass is similarly designed. However, when the compensator designed for mass m_1 is applied to the scanner that contains mass m_2 and imaged, less than satisfactory results are obtained (see Figure 4-13). This experiment mimics the scenario where a single feedforward controller is universally applied to all samples and demonstrates that a more advanced approach is required that uses current information of the scanner dynamics.

Until recently, the user must make a tradeoff between lower performance imaging or cumbersome system identification experiments for each new sample or imaging environment, with most researchers simply choosing to operate their microscopes at low speeds. With the approach described here, high speed imaging is available to any microscope operator regardless of training, and high performance results are made widely available.

4.6.2 Sample Topography Correlated between Scanlines

In Section 4.3.2, the minimal system identification algorithm is described to be based on the notion of cross-correlation. It is assumed that of all the sources that influence the deflection signal, only scanner disturbances are correlated between scanlines. For the majority of AFM operation this assumption holds, however there are a few cases where that assumption may not be valid and further attention is required.

Specifically, consider the case where sample topography has spatial periods that for some scan speeds occur with similar periodicity to scanner disturbances. An example of this situation is collagen fibrils that happen to be oriented predominantly along the fast scan axis as in Figure 4-14A. In this situation, it is possible for the 67 nm banding pattern of collagen to produce deflection traces that are highly correlated due only to sample features. This could cause the algorithm of Section 4.3.2 to attribute this regular pattern to scanner dynamics. Specifically, the section traces from Figure 4-14A are shown in Figure 4-14C with Section 1 showing a scanner disturbance and Section 2 showing the periodic banding of collagen fibril. When effective input shaping is applied, only the part from the scanner disturbances
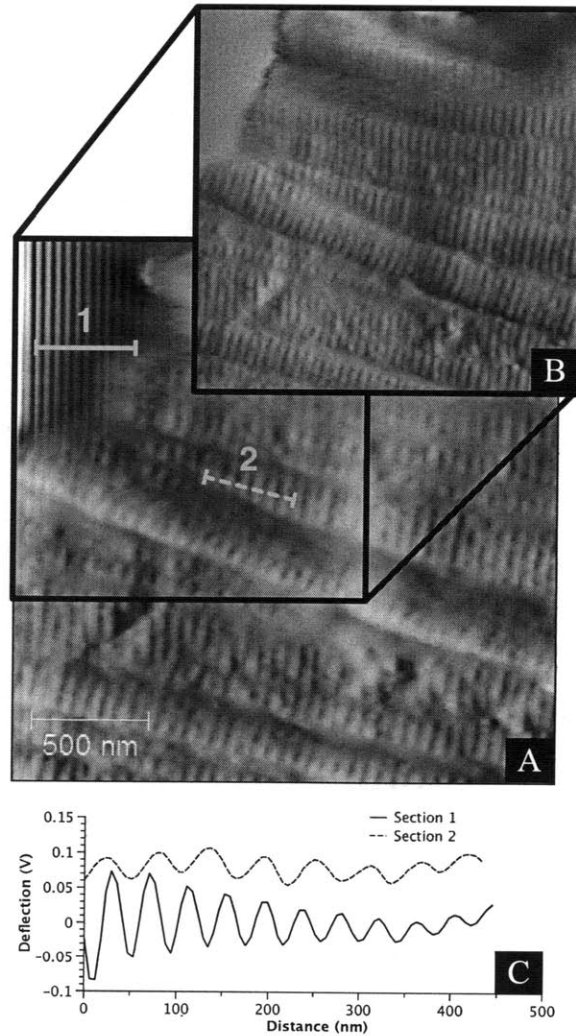
Figure 4-14: A. Collagen data imaged with Veeco E scanner at 10 Hz line rate with no-
ticeable disturbances (Section 1) and sample topography whose spatial frequencies appears
at the same periodicity as the scanner disturbance (Section 2), making unambiguous iden-
tification problematic. B: Same sample taken with an input shaper showing the effective
removal of disturbances without altering sample topography. C. Section traces of the scan-
ner resonance (Section 1) and 67 nm collagen banding pattern (Section 2).

is removed, revealing the underlying topography as shown in Figure 4-14B. The difficulty in designing an effective input shaper is successfully separating the correlated topography from the scanner disturbances in the identification step. A few potential approaches are discussed below.

In order to unambiguously separate topography from scanner disturbances in the unusual situation where periodic topography masks as scanner ringing, it is helpful to consider the source of the two signals. The scanner dynamics originate from a time-invariant (TI) dynamic process, while the topography comes from the spatially invariant (SI) property of the sample. These two signals get mapped into the sampled-time domain (the analog-to-digital conversion process for imaging) through the scan velocity. One promising approach is to vary this mapping while considering deflection signals in the temporal frequency domain. For example, if the scan velocity is varied from 10 Hz to 20 Hz and the temporal frequency response of the deflection signal is plotted, those features that are stationary can be attributed to the TI part and used for scanner characterization. Another way to vary the mapping is to take two images at the same scan speed, but with different orientations or scan directions and preform a similar temporal or spatial frequency response test for SI or TI properties.

However, the approach that holds the greatest promise for user-independence is one that separates the scanner disturbances from the spatial periods entirely. Recall from Section 4.4.2 that scanner ringing is excited even at low scan speeds (and do not corrupt the image at low speeds because the Q factor is low enough to damp out the ringing before imaging occurs). It is recognized that with fast sampling of the deflection while scanning at low speeds, the scanner dynamics can still be identified, and a compensator is designed informed by the model obtained at low speed. Because the scanner is time invariant over the range of imaging experiments, a single compensator can be designed using low speed information where troublesome topography does not confound the algorithm, and that compensator can be effectively applied at high speed.

As an example of this third approach, consider the collagen data of Figure 4-15 taken at high speed (20 Hz line rate, left column) and low speed (3 Hz line rate, right column). Image data highlighting the scan are used for identification is shown in Figure 4-15A and
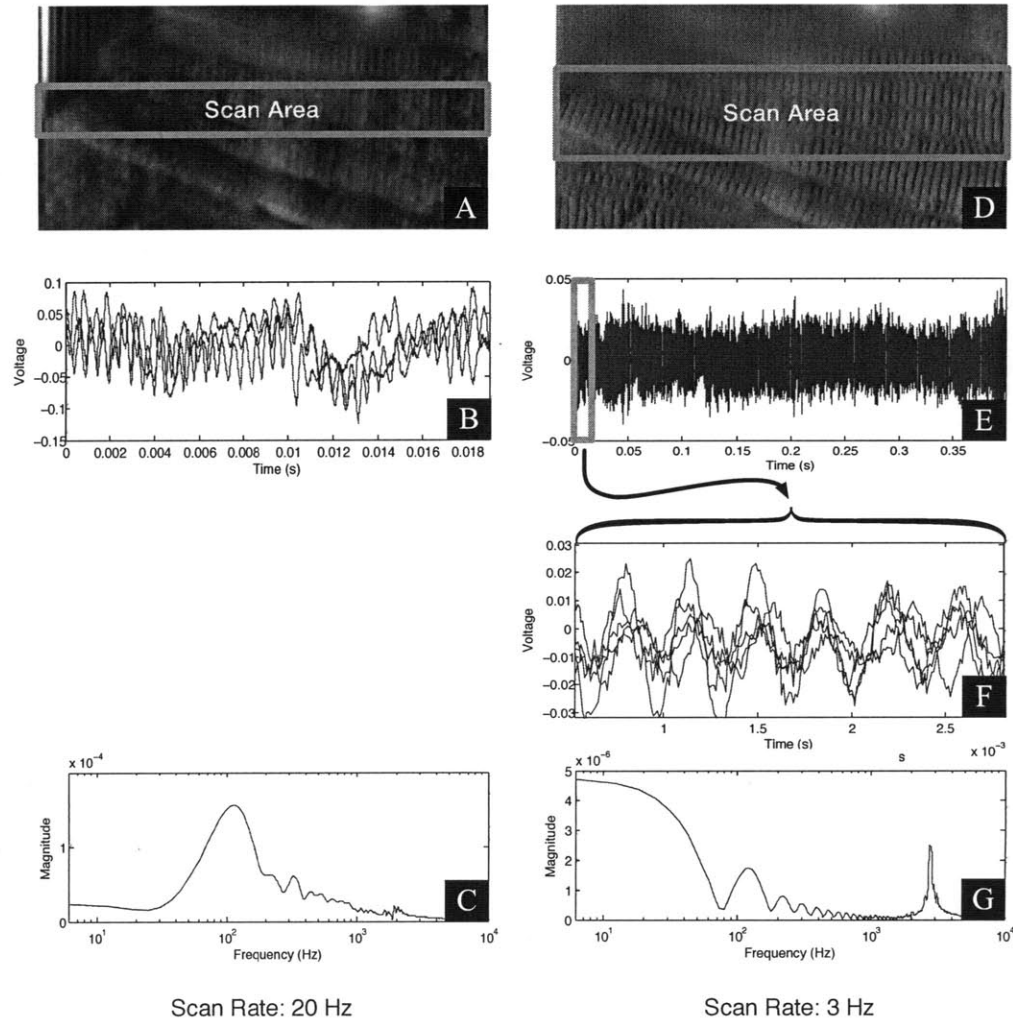
Figure 4-15: Samples that happen to have periodic features that are predominantly aligned with the fast scan axis can confound the indirect identification strategy when periodic topography scanner appears as scanner resonance disturbances. A. At 20 Hz line rate, collagen fibrils have periodic features that appear as scanner resonances. B. Deflection signals overlaid show an influence of both topography and scanner ringing. C. Frequency domain plot of B. showing that identification of the scanner resonance at 3 kHz is obfuscated by spatial frequencies around 100 Hz. D. However, at low speed sample topography is separated from scanner dynamics. E. Deflection trace of the overall image. F. Deflection trace zoomed in to the beginning showing scanner ringing without topographic influence. G. A discrete time Fourier transform of F showing energy from the scanner resonance around 3 kHz, which is used to design an effective feedforward compensator.

Figure 4-15D for high and low speed, respectively. At high speed, scanner resonance is difficult to distinguish from sample topography as shown in the deflection traces of Fig. 4-15B. A frequency response plot of these deflection traces (Fig. 4-15C) show a nebulous region of large energy around 100 Hz from the collagen spatial periods mapped into the sampled time domain, which overwhelm the scanner resonance at 3 kHz. For this imaging situation, the indirect identification method would not converge to the correct scanner dynamic properties.

However, at low speed spatial frequencies from the sample do not overlap the scanner resonance. When the deflection trace of Figure 4-15E is sampled with high speed A/D converters, scanner resonance properties are detected at the beginning of the deflection trace (Fig. 4-15F) and a frequency response clearly shows the scanner resonance at 3 kHz. From this information, the indirect identification method of Section 4.3.2 converges to the correct information about the scanner resonance and an effective feedforward compensator is designed. Because the scanner dynamic properties are time-invariant, the feedforward filter designed at low speed effectively avoids excitation of the scanner resonances at high speed, and high quality imaging at fast scan rates is achievable even in the presence of periodic topography.

4.7 Summary

It is shown that because the lateral scanner dynamics which often limit AFM imaging rates couple into the z direction, dynamic properties of the scanner can be identified. From this indirect measurement of the scanner resonances, a feedforward input shaper can be designed. This compensator is effective at suppressing the scanner resonances, while allowing for high speed scanning. Moreover, because this detection scheme requires no special system identification experiment with exotic inputs or external sensors, scanner characterization can occur immediately before imaging, which allows aggressive compensation without the traditional susceptibility to modeling errors. Further, once the primary source of disturbance is eliminated from the image, a second iteration of indirect identification and compensation can be performed.

Because it is sensor-less, this approach has the potential to be implemented on existing AFMs as a software update and provide a fully automated means for realtime scanner characterization and compensation without user involvement. Therefore, this method has the potential to unlock new experimental scenarios from existing microscopes, and is available to many researchers not otherwise trained in the compensation of dynamic systems.

Chapter 5

MIT High Speed AFM

While dramatic improvements in the performance of conventional AFMs are realized with self-actuated and sensed cantilevers (Chapter 3) and suppression of the lateral resonances of the piezo tube scanner (Chapter 4), an increase in scan speed of three orders of magnitude is possible by re-engineering all of the components of the AFM. The goal of this fundamental redesign of the AFM is to obtain high imaging rates (up to 1000 lines/second) while maintaining suitable image quality and, importantly, large scan areas.[1]

The system described in this chapter is an extension of the work by Hansma, *et al.* [38, 46, 37, 87, 53], with the present work providing improvements to the scanner, and application of the indirect system ID and resonance compensator of Chapter 4. The indirect method for identifying lateral resonances of the scanner is applied to this prototype scanner to achieve an additional order-of-magnitude improvement in the scan speed. Components of the high speed AFM are described and compared to conventional AFMs, with special attention paid to the scanner. Additional components necessary to obtain the high imaging rates are described, and data is presented from the AFM at 1000 lines/sec (8 images/second) with a scan area of several microns.

---

[1]While high speed AFMs have been built that image nanoscale features at up to 30 frames/second, these microscopes have scan areas on the order of a few hundred nanometers and are not capable of imaging biological specimen larger than macromolecules [8, 7, 56, 4]. The high speed AFM described in this chapter has a scan volume of $15\,\mu m \times 15\,\mu m \times 4\,\mu m$, which is large enough to image many types of cells.

5.1   Components of the MIT High Speed AFM

With the ultimate goal of high speed, high quality imaging in mind, the components of conventional AFMs are considered and their typical bandwidths are identified (Figure 5-1). Each component critical to image generation is examined, and a higher bandwidth version that performs the same function is used in the MIT High Speed AFM (Figure 5-2).

The rest of this section will discuss the components of the MIT High Speed AFM, with particular attention paid to the prototype scanner and resonance identification and compensation strategy of Chapter 4.

5.1.1   Scanner and Resonance Compensator

In order to design an AFM to be capable of high speed imaging, the fundamental limits of scan speed explored in Chapter 2 must be considered. In particular, recall that small cantilevers (Section 2.1.2) scanned with constant velocity (Section 2.3) are preferred. However, as noted in Chapter 4, the Fourier components associated with the sharp turnaround of the scan command signals can excite resonances of the scanner. In this work, the scanner is redesigned to have its first resonant frequency be very high (12 kHz, or more than 10 times higher than most piezo tubes), and even when the very fast scan command signals would excite the resonance, the indirect system ID and feedforward compensation strategy from Chapter 4 is applied to this scanner with similar successful results. The design philosophy of the prototype scanner is discussed below to illustrate how the necessary high resonance frequencies are obtained.

Scanner Design Philosophy

Piezo tubes tend to have low resonances and poor tracking capabilities due to the tradeoffs made in their electrical and mechanical design. In particular, piezo tubes actuators often used in SPM applications are constructed of an active part (a cylindrical tube of a piezo-electric crystal, often lead zirconate titanate (PZT)) and a passive component that serves as an extender to amplify the displacement of the active part. This construction allows the larger imaging area that are desired (approximately 120 μm × 120 μm), and keeps the
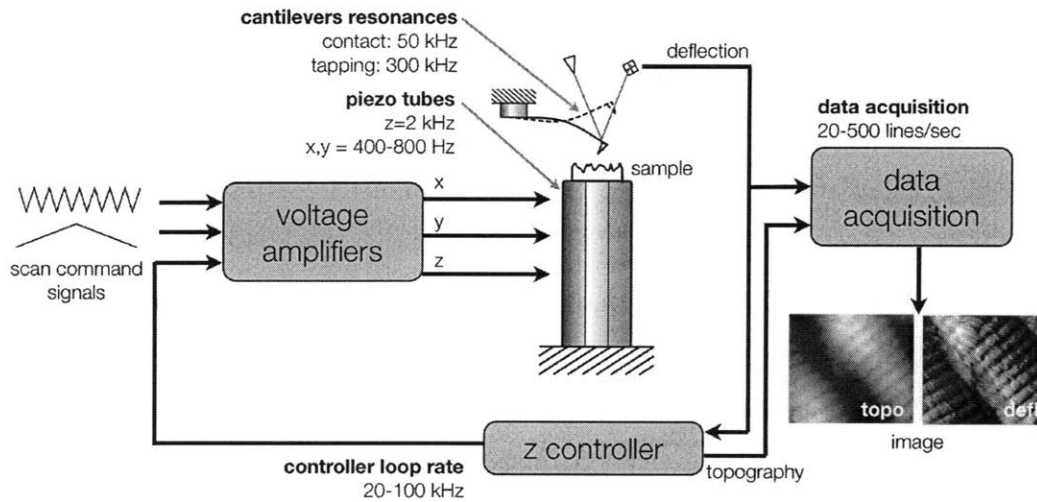
Figure 5-1: Typical component bandwidths for a commercial AFM.
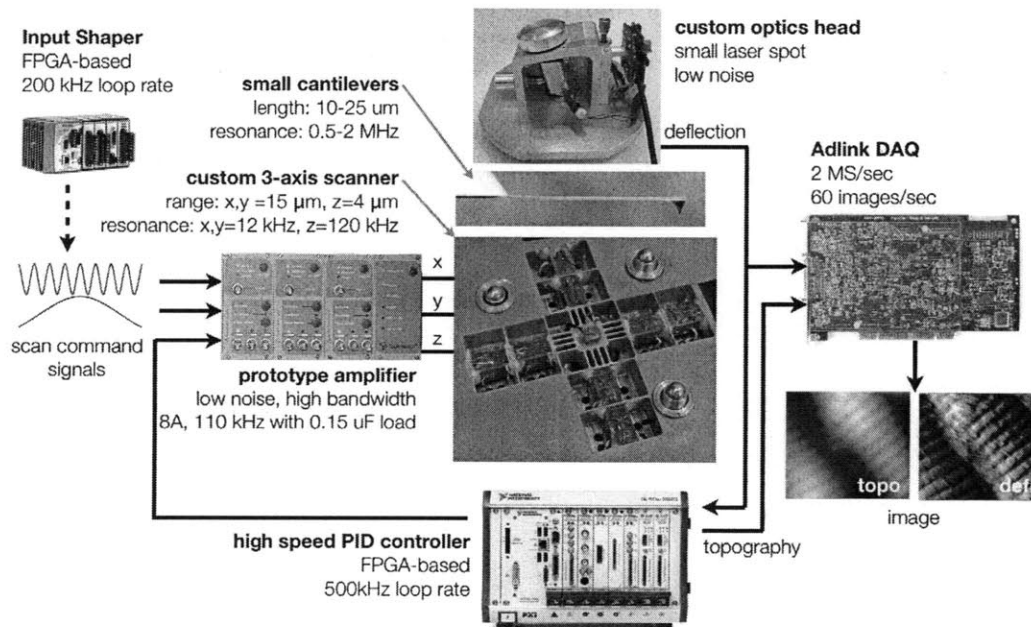
Figure 5-2: Replacement components and associated bandwidths for the MIT High Speed AFM.

electrical capacitance of the piezo low for use with inexpensive voltage amplifiers. However, using the extender tube dramatically increases the scanned mass, and leads to low resonance frequencies. Recognizing the deficiencies in piezo tube actuators, a redesigned scanner based on [88], allows for much higher resonant frequencies, as explained below.

Briefly, the MIT high speed scanner is not made with a single piezo tube, but with a plurality of piezo stack actuators arranged in a symmetric cartesian flexure mechanism (section view of the flexure shown in Figure 5-3). Piezo stacks are capable of generating much higher forces (800 N each for the 8 piezo stacks used in the x, y part of high speed scanner). Using high force actuators allows reasonable ranges from a high stiffness flexure mechanism. By keeping the scanner's lateral stiffness large ($\uparrow k_{\text{struct}}$), and the scanned mass small ($\downarrow m_{\text{scanned}}$), high resonant frequencies are obtained ($\omega_n = \sqrt{k_{\text{struct}}/m_{\text{scanned}}}$). This design approach has yielded a scanner that features a 15 μm range in the x and y axes with the first resonance at 12 kHz—more than 10 times higher than piezo tubes. It should also be noted that the symmetric construction of the x, y axes makes no assumption about a preferred fast scan axis as is characteristic of other high speed AFMs [4, 56]. In this manner, the MIT High Speed AFM can image with arbitrary orientation simply by transforming the scan command signals.
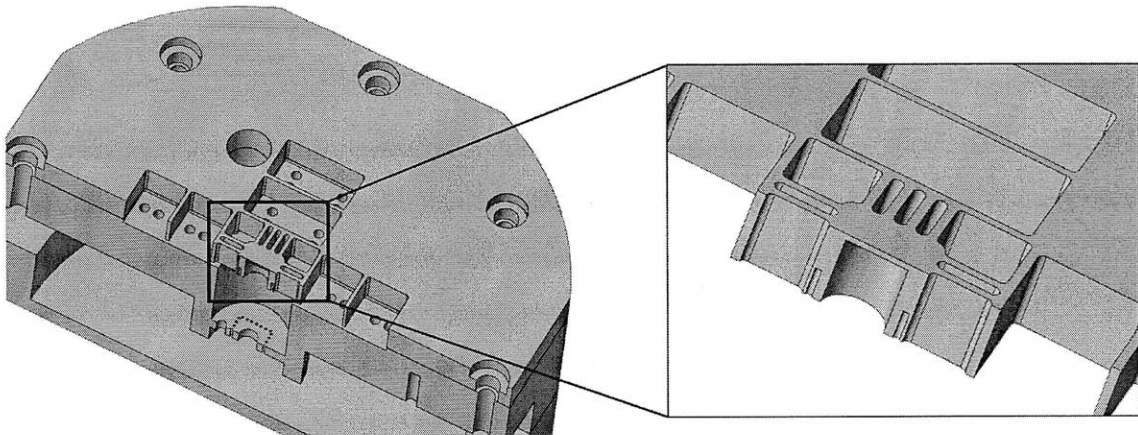
Figure 5-3: The scanner designed for the MIT High Speed AFM. (left) Section view of the scanner showing the three main pieces: the flexure plate used for x, y positioning, an anchor plate for supporting the flexure and securing the z axis vibration, and the lower housing to contain and shield supporting components. (right) Close-up section of the flexure plate showing the central x, y, z positioning stage.

Figure 5-3(left) shows the three main pieces of the high speed scanner: the top plate is the flexure used for x, y positioning, the middle plate is an anchor for supporting the flexure and securing the z axis vibration, and the lower piece is housing to contain and shield supporting components (gears, approach screws, circuit card, etc.). Figure 5-3(right) shows a close-up section of the flexure plate, highlighting the central x, y, z positioning stage. The stage is moved in x and y by 10 mm long stack piezos, and a pair of z piezo stacks are mounted the central stage to provide vertical motion. The sample is mounted on the z piezos.

Two strategies are employed to suppress resonances in the vertical direction, the first uses passive mechanical elements to increase the z stiffness while still allowing x, y translation, and the second uses active elements to balance the momentum introduced from the z piezo actuators. Specifically, the former uses thin steel wires that are secured from the underside of the flexure to the anchor plate and bend to allow motion in x, y, but are stiff in extension. The latter requires an additional stack of two piezos that are mounted underneath the central stage and excited with the same input signal as the main z piezos to counteract the momentum introduced by moving the sample in the z direction in order to constrain the central stage from vibrating out-of-plane like a drum head. By making the z axis of the scanner as stiff as possible, the feedback controller gains can be increased without suffering from instabilities in the feedback loop, and faster topography tracking is achieved.

Resonance Compensation with the High Speed Scanner

Even with the high resonant frequencies that are enabled with piezo stacks and stiff flexures, high speed scanning at constant velocity will still excite these resonances, and a method is required for identifying their characteristics and avoiding their excitation. The novel indirect system ID algorithm of Section 4.3.2 and feedforward compensation of Section 4.4 is successfully used with this experimental scanner. In Chapter 4, this method demonstrated a 40× scan rate increase in conventional piezo tube scanners (from 1 line/second to 40 lines/second), and it achieves a similar factor of improvement on the high speed scanner. Using this compensation method, scanner operation of over 1000 lines/second have yielded good quality images, and even higher speed scanner operation is routinely obtained before

other components in the high speed microscope reduce image quality. See Figure 5-4 for an image taken at 1000 lines/second with and without feedforward compensation. These images show topography (left) and deflection (right) of 25 nm high silicon features, and take less than 125 ms to obtain the full image. Without resonance compensation (top), the image is corrupted by lateral scanner resonance and the expected linear features appear distorted. However, the feedforward resonance compensator identifies and avoids the excitation of the lateral resonances, providing undistorted imaging at 8 images/second.

Reduced quality images have been obtained at 1400 lines/second, but topography tracking is reduced due to limited z feedback bandwidth, and produces images with lower spatial frequency details. (This is discussed further in the section on the z feedback controller.) However, experiments on the scanner subsystem indicate that x, y triangle wave tracking with the feedforward compensator is possible at faster than 2000 lines/second, indicating that if the z tracking bandwidth can be improved, even higher speed imaging is possible.

Resolution Limitations at High Speed

Additionally, it should be noted that the z axis in the nanopositioner used for AFM imaging has the most stringent requirements. For each of the high speed scan lines traced by the x axis, the z axis must track topography within that scan line. For example, if the sample topography has features with 25 periods in the scan area (which would originate from a smooth sample and represents a lax constraint), then for each scan line (which consists of a left-to-right trace and a right-to-left retrace), the z feedback controller and actuator must track 50 periods (2 lines × 25 periods/line = 50 periods). When scanning at 1,000 lines/second, this requires a 50 kHz tracking bandwidth, which is very high for a mechanical system. For the silicon samples in Figure 5-4 with step changes in topography, only spatial periods within the tracking bandwidth of the z feedback system are imaged, with higher spatial frequencies not recorded. We conclude that resolution in these images is limited by the z feedback bandwidth.
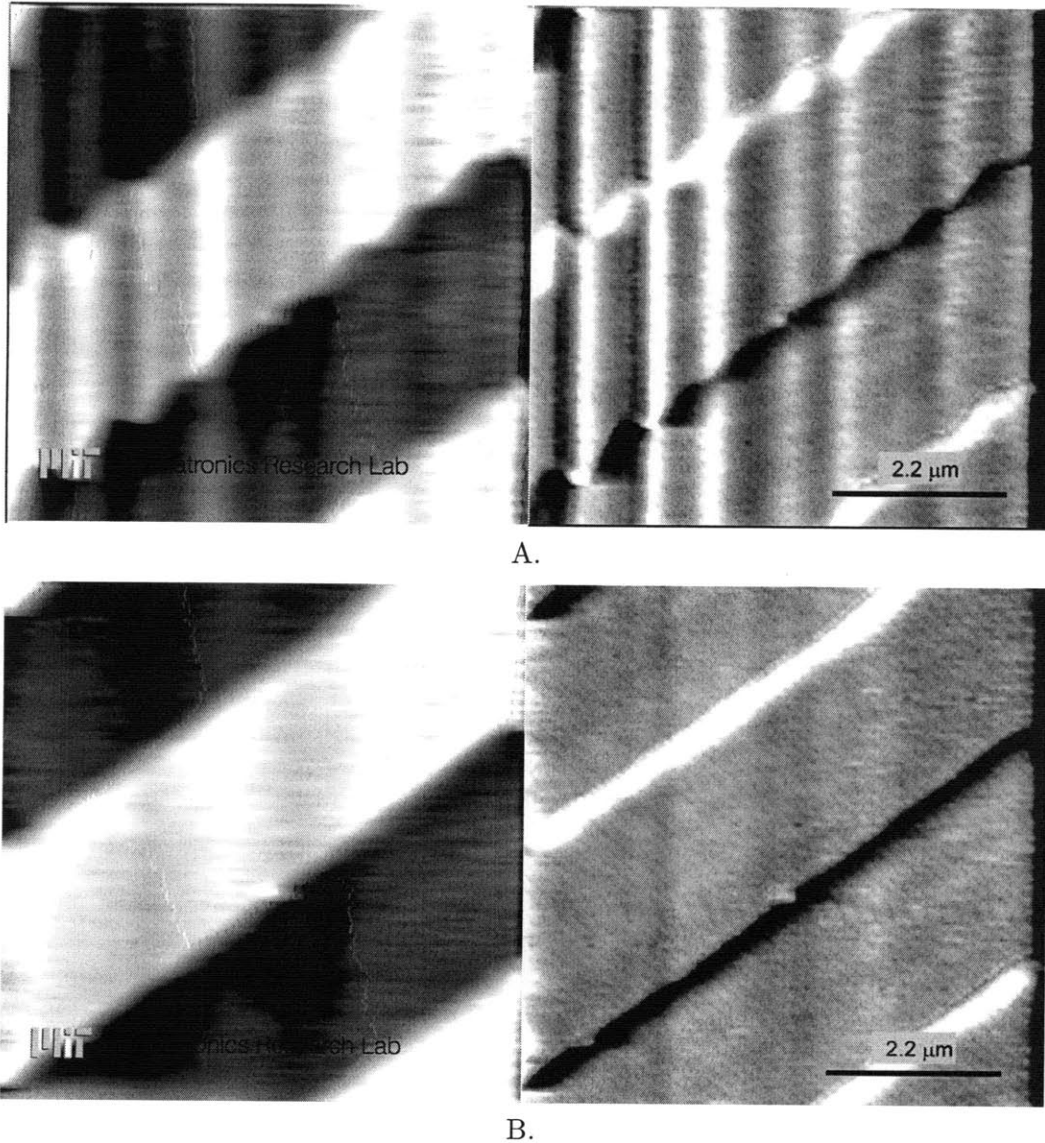
Figure 5-4: Images taken from the MIT High Speed AFM demonstrate the effectiveness of the indirect system ID and compensation method even at high speed. These topography (left) and deflection (right) images of 25 nm high silicon steps are taken at 1000 lines/second, or a full image in less than 1/8th of a second. A. An image is obtained with the resonance compensator off showing ringing of the scanner corrupting both topography and deflection. B. With the resonance compensator on, the lateral scanner resonance is not excited. The spatial resolution is expected to be improved with faster z feedback bandwidth.

5.1.2   Additional Components

In addition to the scanner and resonance compensator discussed previously, several other components must be redesigned for higher speed operation. Refer again to Figure 5-2 and note that the following section briefly discusses (i) small cantilevers, (ii) the optics for small cantilevers, (iii) high performance voltage amplifiers, (iv) the z feedback controller and (v) the data acquisition system. More details of these components can be found in [38].

Small Cantilevers As discussed in Section 2.1.2, small cantilevers are required for high speed imaging. The high resonant frequencies and relative low Q factors make for a sensor with high detection bandwidth that is still gentle to delicate samples. The cantilevers used in the MIT High Speed AFM are 10 μm long, 5 μm wide and a few hundred nm thick (SCL-SensorTech GmbH, Vienna, Austria). Although these cantilevers have high resonant frequencies (up to 1.9 MHz), current construction of the cantilever holder assembly requires operation of the High Speed AFM in contact mode. Because these cantilevers are shorter and narrower than conventional cantilevers, a more tightly focused laser spot is required for adequate optical lever detection.

Optics The optical assembly is custom built to interface to the bolt pattern of high speed scanner (three 1/4" − 80 screws used to lower the cantilever and optical assembly onto the sample). An assembly consisting of a 650 nm wavelength laser, collimating lens and an objective lens is aimed onto the cantilever with adjustment screws. The objective lens has a numerical aperture of 0.4, a focal length of 3.3 mm, and a depth of focus of 250 μm, making alignment and focusing of the laser more challenging than with conventional AFM systems. A four channel photodiode is mounted on sliding rails for balancing the optical signal used for feedback, and the top two quadrants (V_T) and bottom two quadrants (V_B) are wired to a custom current-to-voltage conversion and subtraction circuit ($V_o = V_T − V_B$) to output a signal proportional to cantilever deflection.

Amplifiers While the use of high force actuators has enabled higher scanner stiffnesses and therefore faster scanning, the tradeoff is the large capacitive loads associated with these actuators that must be driven by the voltage amplifiers. The piezo stacks

used in the MIT High Speed AFM can have a capacitance as large as 0.7 μF for the x, y piezos, which can difficult to drive at high frequencies.

The high performance amplifier (Techproject Company, Vienna, Austria) is designed around a PA93 MOSFET op-amp (Apex Microtechnology, Tuscon, AZ) and can source 8A of continuous current at 150V. Series output resistors and short circuit protection are omitted in favor of high bandwidth operation. Each of the three outputs per channel (six channels total) is tested with the specific piezo stacks used in the scanner to ensure stability and tune the bandwidth or step response for maximum performance and low noise. The measured RMS noise at the output is less than 1 mV_{pp} over the full $0 - 150$ V range, which translates to unloaded x, y piezo displacement of less than 0.07 nm RMS uncertainty due to amplifier noise.

Feedback Controller The z feedback controller used to track the topography based on the cantilever deflection is implemented with a high speed FPGA (PXI-7851R, National Instruments, Inc., TX, USA). A custom written PI controller is programmed for this FPGA and executed at 500 kHz loop rate (*i.e.,* the analog-to-digital conversion, and digital-to-analog conversion occurs at 500 kHz). Using a well-known rule-of-thumb, the tracking bandwidth is expect to be about a decade below the sample rate, or 50 kHz. As discussed in the previous section, the limit of resolution of the high speed images in Figure 5-4 is due to the controller's limited bandwidth. When a higher speed PI or PID controller can be substituted, better quality and faster imaging is expected from the MIT High Speed AFM.

Data Acquisition Data from the high speed AFM is collected with a DAQ-2010 (Adlink Technology, CA, USA). This high speed data acquisition card is programmed in Lab-VIEW, and collects two analog input channels (AI 0: topography or PI controller output, AI 1: deflection or controller error). This incoming data is synchronized with the card's two analog outputs (AO 0: x scan command signal, AO 1: y scan command signal).

The data acquisition card can collect data at rates up to 2 MS/s, which can equate to 60 images/second, depending on the number of samples used to create an image. The

details of the data acquisition system are available in previously published articles [37].

Using these components, the high speed AFM is capable of recording high quality images at more than 8 frames/second. High speed images are presented in the next section.

5.2 Imaging Results

The MIT High Speed AFM is used to image 25 nm high features in silicon. Data is recorded at 1000 lines/second in contact mode and using 128 lines/image, the resulting image rate is nearly 8 frames/second. Six frames from the data stream are shown in Figure 5-5 recorded during zooming in on debris. The sequence takes place over 3 seconds.

Data recorded here represents about three orders of magnitude improvement in speed performance compared to conventional AFM. Many interesting experimental scenarios are enabled and new phenomena are observable with the instrument described herein. Section 6.3 describes potential experiments that could be performed with this new instrument in the future and would reveal new information about physics and biology at small length scales and short time scales.

5.3 Summary

The high speed AFM described in this chapter is capable of imaging nanoscale features three orders of magnitude faster than conventional AFM. In order to achieve these results, each component of the microscope is redesigned to perform at higher speeds. In particular, the high speed scanner is engineered to have high resonant frequencies, large range, and a symmetric x, y configuration. This allows large imaging volumes suitable for studying biological structures such as cells and viruses, and since there is not one assumed fast scan axis, an arbitrary image rotation can be used as the application demands.

These high speed results are also only possible with application of the novel lateral system identification and feedforward compensation strategy of Chapter 4. Automatic characterization and compensation is especially critical for this scanner where the scanned mass is designed to be minimized and its value is largely dependent on the sample. In other words,
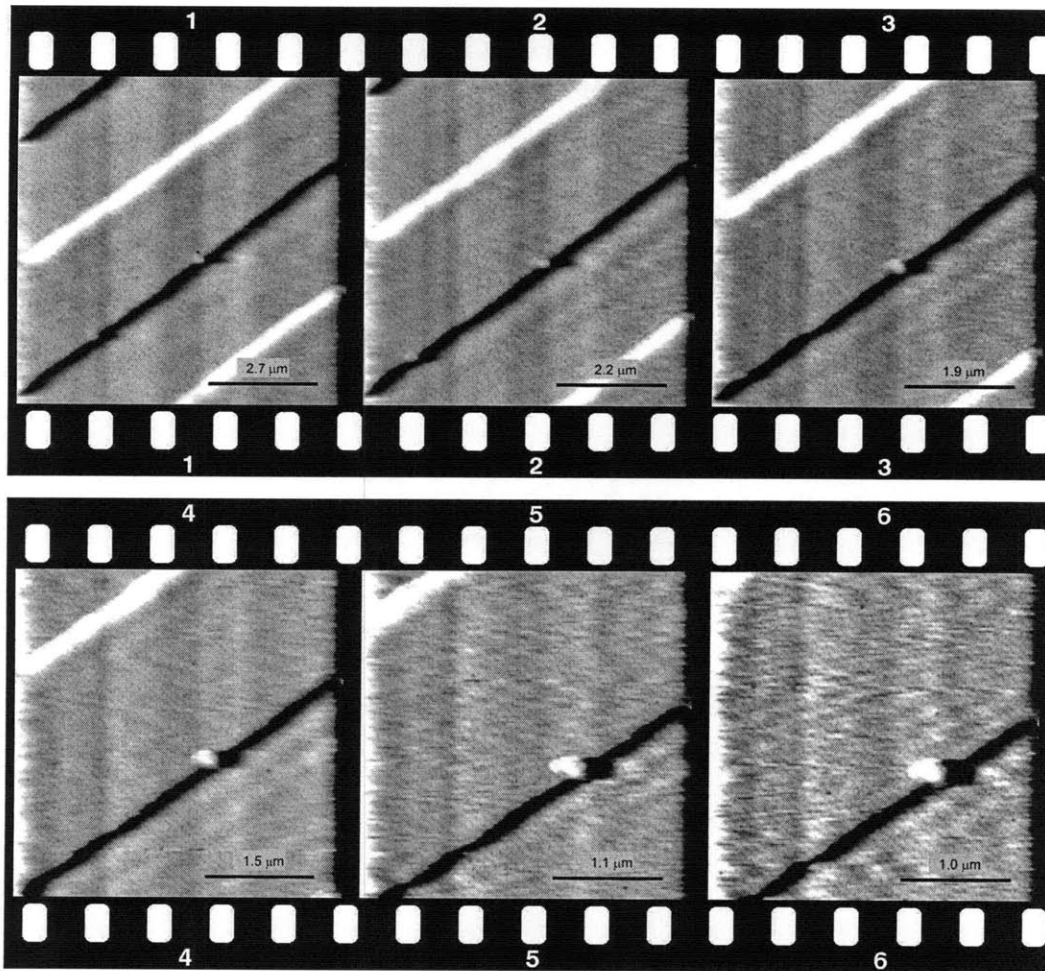
Figure 5-5: Deflection image sequence showing a zoom operation on debris for 3 seconds. Data is taken at 1000 lines/sec with 128 lines/frame. Each frame represents about 1/8th of a second and every 4th frame from the sequence is shown.

since the high resonant frequency requires a low scanned mass ($\omega_n = \sqrt{k/m}$), the scanner is designed to minimize m, as a result, very little mass is used as part of the microscope supporting structure, and a large fraction of the scanned mass originates from the sample itself. Therefore, changes in sample mass will have a large effect on the scanned mass, and will strongly influence the resonance that must be avoided in scanning. One benefit of the automatic identification and compensation strategy described previously is a just-in-time characterization that identifies the resonant frequency of the scanner immediately before imaging.

The high speed AFM developed here is expected to enable new observations and exper-

imental situations. While nanoscale resolution is maintained or only slightly reduced, the imaging rate is dramatically increased, and should permit the observation of phenomena not previously recorded, such as cellular dynamics, polymer relaxation, and chemical etching. These potential experiments and more are described in a section on future opportunities in the next chapter.

Chapter 6

Conclusions and Recommendations

6.1 Research Summary

The resolving power and versatility of the atomic force microscope (AFM) has established it as an essential tool for nanotechnology, biological studies and semiconductor process characterization. Its unique ability to image nanoscale features in air, vacuum or liquid, and on conductive or insulating samples, makes the AFM often the only instrument capable of certain observation modalities. Its precision force detection capability merged with functionalization of the force probe has opened new fields of study (*i.e.*, molecular force spectroscopy, magnetic force microscopy, and topography and recognition imaging) and new and exciting uses of the AFM continue to produce dramatic results.

However, the primary disadvantage in AFM continues to be the limited speed at which images can be obtained. Scan speeds fundamentally limit most observations to static or quasi-static samples, which restrict the scientific observations that can be made. The thesis contributions here are aimed at addressing the speed limitations of AFM, and doing so in a way that reduces to the demands of the researcher or microscope operator. Toward that end, an effort is made to understand the fundamental limitations of scanning speed in Chatper 2. Using insight gained from the analysis, research is conducted on two primary bottlenecks in high speed operation: cantilevers and scanners. Regarding the former, a novel kind of cantilever that integrates actuation and sensing promises to eliminate many auxiliary components of the AFM infrastructure, including the (often slow) z actuator

115

used for topography tracking, and the cumbersome optics assembly. Work presented in Chapter 3 detailed a thorough characterization of these cantilevers, with the ultimate aim of improving their bandwidth and understanding and eliminating potential obstacles to routine use with, for example, a half-frequency drive system that avoids undesirable low frequency–high frequency actuator coupling. Using the results of this work, routine use of these cantilevers will enable higher speed operation of the AFM and imaging in new situations (*i.e.,* AFM inside an STM) with the goal that these cantilevers be useful without additional demands placed on the microscope operator.

Effort on the latter focused on the resonances that are excited when operating piezo tube scanners at higher speed. Chapter 4 described a novel algorithm that extracts information about the lateral scanner dynamics from the deflection signal. In this manner, the ultimate metric of observation quality, the image, is used to judge whether lateral resonances are large enough to corrupt the image, and if so, a method is described to extract sufficient parameters to identify the scanner dynamics and design a compensator. This compensator successfully increases the imaging bandwidth from 1 line/second to 40 lines/second. This method has the important feature of enabling a just-in-time scanner characterization that circumvents the previously required tradeoff between compensator performance and robustness to scanner dynamics variation—the performance benefits of an aggressive compensator are realized without the susceptibility to parameter variation. This ability to immediately identify the scanner dynamics can be done automatically and without modification to most commercial microscopes, providing a user-independent path to rapid imaging for most of the 15,000 AFMs installed worldwide. Further, this method is shown to be robust to even the most challenging topographies where sample periodicity could be mistaken for scanner artifacts. Recognizing that the scanner resonance is excited even at slow speeds, and using the time between scan lines to acquire information about the scanner dynamics, a method is discovered to separate spatial features from scanner resonances.

Finally, a state-of-the-art high speed microscope is constructed by replacing all the components of a conventional AFM with high speed versions in Chapter 5. Special attention is paid toward the design of the scanner, and by using large force actuators, a stiff flexure-based nanopositioner is constructed that achieves imaging rates of several frames per second. How-

ever, this high speed scanning requires the indirect identification and compensation of the Chapter 4. The effectiveness of this compensator is demonstrated in Section 5.2 and shows images of nanoscale features resolved at speeds of 1000 lines/second, or 8 images/second. This enhanced imaging capability is expected to enable new scientific observations.

Specific contributions and outcomes are highlighted in the next section.

6.2 Contributions

6.2.1 Active Cantilever

- Identified crosstalk between the cantilever's integrated thermal actuator and strain gage signals, and verified with simulation. This has resulted in a redesigned cantilever with additional signal separation and grounded interstitial traces. (Section 3.3)

- Identified undesirable coupling in the actuator between the low frequency commands used to track topography, and the high frequency commands used to oscillate the cantilever. A phyics-based model explained the source of the coupling and suggested a method to eliminate the coupling using a half-frequency drive approach. Researchers have since used this method to image with these active cantilevers in liquid demonstrating improved results compared to conventional cantilevers [39]. (Section 3.3.4)

- Developed model of cantilever dynamics suitable for model-based control. (Section 3.4.1)

- Increased cantilever tracking bandwidth from 0.4 kHz to 11 kHz using model-based compensator, resulting in speeds that are faster than piezo tubes in the z direction. (Section 3.4.2)

- Demonstrated imaging with these cantilevers where topography is tracked with a combination of z actuators: using the piezo tube for slower, larger displacements, and the integrated thermal actuator for faster, smaller displacements. (Section 3.5)

6.2.2 Indirect Identification and Compensation of Scanner Dynamics

- Recognized deflection signal includes a source that can be used to characterize the scanner dynamics. (Section 4.2)

- Modeled the scanner dynamics to understand the source of the coupling and prove that it is observable through the deflection signal. (Section 4.3.1)

- Developed an algorithm to extract scanner dynamics from the deflection signal that otherwise includes other sources of information (topography, sensor noise, controller artifacts, etc.) (Section 4.3.2)

- Analysis to understand why the indirect identification algorithm works and note the limitations where it fails (Section 4.3.2)

- Addressed an anticipated situation where the algorithm could fail due to correlated topography (Section 4.6)

- Described a novel compensation strategy that considers the image quality to determine if a higher scanner mode continues to corrupt the image after the first mode has been compensated (Section 4.4)

- The main result is an automated way to identify the primary cause of high speed imaging distortion, and design and implement a compensator without user involvement or microscope modification.

6.2.3 MIT High Speed AFM

- Demonstrated sensor-less detection of lateral dynamics and automatically compensated at state-of-the-art speeds. (Section 5.1.1)

- Extended high speed AFM instrumentation to accommodate large-range, video-rate nanoscale imaging. (Section 5.2)

6.3 Recommendations for Future Work

While this work represents advancements in imaging speed and ease-of-use in atomic force microscopy, many opportunities exist for further work. These opportunities are explored in the context of (i) active cantilevers, (ii) conventional scanner characterization and control, and (iii) high speed instrument development.

6.3.1 Future Work in Active Cantilevers

In Chapter 3, significant effort is placed at understanding and characterizing a new kind of cantilever. While substantial fundamental progress is made, and modest improvements in bandwidth are demonstrated, the realization of truly high speed AFM will require advancements in microfabrication techniques. The large size of these active cantilevers set the time constants that fundamentally limit the relatively low resonant frequency. With improvements to fabrication, these cantilevers are expected to be made smaller, and increases in resonant frequency and hence scan speed will scale proportionally.

A feedback loop structure (Figure 3-11) is employed in Section 3.5 where the tracking signal is separated in parallel to both a high-bandwidth, low-displacement actuator (thermal actuator), and the converse (z piezo tube). A more preferred structure may be one developed in the hard disk drive industry where the position commands are sent in serial, where a high bandwidth actuator in an inner loop handles high frequency commands, and the large range actuator is used for large displacements with an outer loop. The structure used in Chapter 3 demonstrates an improvement in imaging speed compared to conventional AFM, a more dramatic result may be available with a more carefully considered feedback structure.

In Section 2.2.3, the tradeoff between high speed imaging and high sensitivity imaging was described as it related to the Q factor of the cantilever. With the active cantilevers of Chapter 3, the additional actuator authority opens the possibility to active control of the Q factor of the cantilever, with the goal of using Q control to alter the properties of the cantilever for either high speed or high sensitivity. As an extension, it may be possible to use Q control strategies to shape the resonance of both the fundamental frequency and higher harmonics, so that both high speed and sensitive imaging can occur from a single

cantilever at the same time. This work has yet to be done and could represent fertile ground for new research.

6.3.2 Future Work in Scanner Characterization and Control

The vision for indirect scanner characterization and control is one that enables researchers focused on their disciplines to achieve higher scanning speeds without onerous modification to their microscopes. While the work of Chapter 4 demonstrates that an automatic identification and controller implementation is feasible, much engineering work remains to adapt the approach to a wide number of existing AFMs. A detailed survey of existing microscopes would reveal how to access the necessary deflection signal and how to filter the scan command signals for an aftermarket product.

As described in Section 4.4.2, too little attention is paid in scanner design to the Q factor. If AFM scanners were designed with higher damping, much of the present work on mitigating scanner resonances would not be necessary. One avenue for broad impact includes incorporating damping and energy dissipation in SPM scanners, and falls under the active research area of "Design for Controllability."

6.3.3 Future Work in High Speed AFM

While there exists many challenges in development of high speed AFM, the most exciting opportunities for future work arise in the context of the new experiments it enables. For this thesis, much effort is devoted to the design, construction and troubleshooting of this new instrument, and operation to date has focused on the demonstration of scanner ID and control. However, now that the instrument is shown to operate at previously unattained speeds, many new experiment opportunities exist—experiments that are interesting and exciting for a broad range of researchers. Collaboration with materials scientists, biologists or physicists with traditional AFM experience is strongly recommended. Several experimental ideas are presented here, but it is stressed that consultation with other researchers will lead to innovative ideas that exploit the new capabilities of this instrument.

Potential new experiments with the MIT High Speed AFM described in Chapter 5 are detailed below.

Recovery of polymer nano-indentation: Recently, much attention has been paid to reducing part variation in high volume fabrication of microfluidic devices. These devices are increasingly made with polymers like Polydimethylsiloxane (PDMS) and understanding their material properties when deformed at the very small scale will help enable repeatability and may improve fundamental models of these materials and inform fabrication processes parameters [61, 28].

The high imaging speeds provided by the experimental AFM would enable visualization of the recovery process of PDMS immediately subsequent to nano-indentation. Recovery to the undeformed shape is expected to occur over the course of seconds—to fast for conventional AFMs to image. The AFM cantilever can be pressed into the surface, held for several seconds, then used to immediately image the surrounding area. This experiment could be repeated for other types of polymers such as polyethylene, and it is suspected that the timescale of the recovery will depend on material stiffness.

Characterization of high volume manufacturing: In addition to understanding the material properties of PDMS at the nanoscale, high volume fabrication requires understanding the forming process variation on these kinds of parts. To date, no single inspection technique provides the simultaneous high resolution and large area required for high volume inspection over large areas of the formed part. Whereas early approaches to this problem attempt to fuse data from disparate sources (*i.e.* merge data from a conventional AFM and an optical interferometer [16]), an alternate approach is one that leverages the high imaging speed of the experimental AFM together with a larger positioning stage to rapidly image critical dimensions of the formed part with high resolution.

Binding of streptavidin to biotin-functionalized surface: Other experiments are more speculative, but have the potential to lead to new scientific discoveries. The goal for this experiment is to record, with high time resolution, the process of binding and dissociation of streptavidin molecules and biotin molecules immobilized on a flat surface (biotin is immobilized on a surface and streptavidin, a larger molecule, is added to a solution). This experiment would attempt to quantify the time constants associated

with binding of these important ligands, which are extensively used as markers or linkers in molecular biology.

Action of an acid on bone tissue: Visualization of the rapid etching process of acid attacking bone may lead to new understanding of osteoporosis or tooth decay. In this experiment, calcite or bone fragments are imaged in aqueous solution and acid is added during imaging. Removal of material is will occur quickly, but the etching process is expected to be observed within the imaging rate of the MIT High Speed AFM.

Appendix A

Recursive AFM Image Smoothing with Acausal Kalman Filtering

This appendix describes a novel model-based algorithm for post-processing AFM image data to remove a particularly troublesome resonance in the z feedback system. The algorithm is based on Kalman filtering, which is an optimal state estimator, that is, it attempts to reconstruct a signal within a dynamic process (in this case the AFM z resonance) by mixing two sources of information: (i) from a noisy sensor output (the cantilever) and (ii) an uncertain model of the dynamics. This appendix extends the online Kalman filter algorithm, which is traditionally used in realtime controls applications, to an acausal version that post-processes AFM image data to remove the influence of the resonance more effectively that with traditional methods. The material from this appendix was first published by this author in [15].

A.1 Background

Many biological processes of interest occur on time scales faster than the imaging capability of conventional AFMs [5, 96], which are typically limited to image acquisition rates on the order of minutes. Operating standard AFMs at high speed when imaging compliant molecules excite resonances that lead to image artifacts, and controller performance becomes critical. Addressing these concerns demand an increased understanding of the influence of
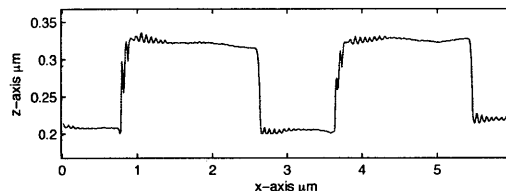
Figure A-1: Individual scanlines of a square-channel periodic grating are shown. When this $6\mu m \times 6\mu m$ area is imaged with linear scan rate of 36 $\mu m/s$ and tuned PID gains, ringing occurs as seen near large changes in amplitude. The ringing is not observed when imaged at 24 $\mu m/s$ (not pictured), illustrating that fast image acquisition is limited by dynamic performance of the microscope. These artifacts observed in fast scanning operation may be dramatically reduced with the proposed Kalman filtering technique.

actuator and controller dynamics on image quality [30]. A specific challenge unique to AFM imaging is the artifacts generated from lightly-damped modes associated with the piezoelectric actuator when scanning too quickly (see Fig. A-1).

The artifacts in AFM images stem from the microscope's underlying dynamics, and these dynamics have been shown to be highly dependent on operating conditions such as sample stiffness, controller gains, probe characteristics and other parameters [33]. And because these operating conditions vary from scan to scan, simple approaches such as notch filters must be manually tuned for each scan, and may even eliminate important topographical information. However, if the applied filter is based on a process model that captures the operating conditions, automatic elimination of artifacts could be performed while preserving sample topography. The result is that an AFM could be operated at faster scan rates and maintain high image quality.

In this section, a discrete fixed-interval smoothing algorithm based on Kalman filtering (but extended to acausal filtering) is applied to noisy images generated by an atomic force microscope. The performance of the smoothing filter is compared to the conventional Kalman filter and a notch filter. Simulated and experimental results are used to verify the filter's performance. The application of this filter allows the AFM to be operated at higher speeds while still producing high quality images.

A.2 Smoothing Algorithm

The discrete fixed-interval smoothing algorithm is similar to the standard discrete Kalman filter (KF) algorithm—both require a model of the process and a characterization of the model confidence and sensor noise—however this smoothing algorithm is adapted to permit acausal filtering (as is appropriate for image processing) through the addition of a backward sweep. The discrete KF equations are widely available and not reprinted here. The augmentation to standard KF algorithm is described below following Brown and Hwang [11].

A model for the AFM dynamics can be cast in the form

$$\mathbf{x}_{k+1} = \mathbf{\Phi}_k \mathbf{x}_k + \mathbf{w}_k \tag{A.1}$$

$$\mathbf{y}_k = \mathbf{H}_k \mathbf{x}_k + \mathbf{v}_k \tag{A.2}$$

where $\mathbf{x}_k$ is the state vector at time t_k, $\mathbf{\Phi}_k$ is the state transition matrix, $\mathbf{H}_k$ maps the states to the measured outputs $\mathbf{y}_k$, and $\mathbf{w}_k$ and $\mathbf{v}_k$ are white vectors representing process and measurement noise, respectively. Common states associated with $\mathbf{x}_k$ may include piezo tube bending angles and angular rates, cantilever deflection angle, and higher order piezo modes (see [30, 33, 32] for details).

Each scanline in an AFM image (Fig. A-1) consists of $N + 1$ evenly-spaced data points that are processed in a forward recursive sweep and backward recursive sweep. Using $\hat{\mathbf{x}}_0^-$ and $\mathbf{P}_0^-$ as an initial *a priori* state estimate and its error covariance (and with the standard KF assumptions on process and measurement models) the forward sweep is processed using a discrete KF filter (see [11] for details), with the additional requirement that the *a priori* and *a posteriori* estimates and the error covariance from each step be saved for the backward sweep.

The backward sweep begins using the last data from the forward sweep, $\hat{\mathbf{x}}(N|N)$ and $\mathbf{P}(N|N)$, as initial conditions. The saved forward-swept filter estimate $\hat{\mathbf{x}}(k|k)$ is updated with data from the backward sweep to provide an improved estimate. The backward sweep recursive equations are

$$\hat{\mathbf{x}}(k|N) = \hat{\mathbf{x}}(k|k) + \mathbf{A}(k)[\hat{\mathbf{x}}(k+1|N) - \hat{\mathbf{x}}(k+1|k)] \tag{A.3}$$

with smoothing gain $\mathbf{A}(k)$ given by

$$\mathbf{A}(k) = \mathbf{P}(k|k)\mathbf{\Phi}^T(k+1,k)\mathbf{P}^{-1}(k+1|k) \tag{A.4}$$

and with k decrementing,

$$k = N - 1, N - 2, ..., 0. \tag{A.5}$$

The error covariance matrix for the backward sweep is given by the following recursive equation

$$\mathbf{P}(k|N) = \mathbf{P}(k|k) + \mathbf{A}(k)[\mathbf{P}(k+1|N) - \mathbf{P}(k+1|k)]\mathbf{A}^T(k) \tag{A.6}$$

Because the final estimated state is processed from both a forward sweep and a backward sweep, data from the current time step and the next time step are required for estimation (*i.e.*, estimating $\hat{\mathbf{x}}_k$ requires $\mathbf{y}_k$ and $\mathbf{y}_{k+1}$). This is the source of the acausal nature of the smoothing filter. Fortunately, for image processing applications where the image generation process can be modeled, acausal filters are preferred and applied in a batch operation after the image has been collected (post processing).

This smoothing algorithm requires an understanding of the process that generated the data, and therefore a model of the AFM dynamics is required. Details of the models used in the following simulations can be found in [30, 33, 32]. In order to validate the selected model and its parameters, a step change in topography (as with a square silicon grating) is simulated and shown in Fig. A-2. Here, the input is to the simulation is a topographic profile, and the output is the resulting controller output (representing the reconstructed image). Compare the response of the real AFM in Fig. A-1 to the simulated response in Fig. A-2 and identify the ringing that occurs when the piezo tube is scanned too quickly. Although there exists a discrepancy in overshoot, the frequency of the ringing is comparable, and as will be shown in the following section, the substantial simulated overshoot is eliminated by the smoothing filter.
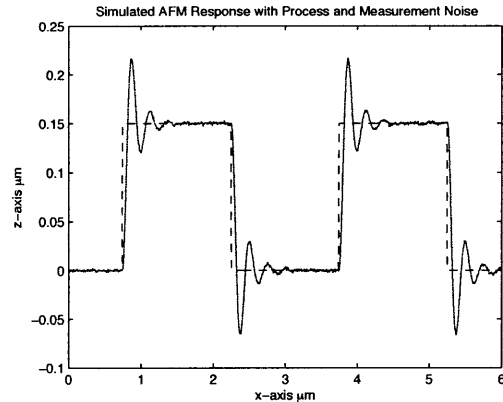
Figure A-2: In order to validate the derived model, the step response is computed. The topographic profile reported by the AFM is shown as a solid line and the true topography is represented by the dashed line. Ringing that occurs in real AFM systems is reproduced here with comparable settling time. These types of artifacts often occur when the control bandwidth exceeds the bending mode frequency, and are difficult to eliminate without sacrificing image fidelity.

A.3 Simulation Results and Discussion

In order to eliminate ringing associated with high speed AFM imaging, the recursive smoothing algorithm is applied to the model. Additionally, because the acausal (two-pass) smoothing algorithm is similar to the traditional realtime Kalman filter, both filters are applied to the data for comparison. The underdamped AFM image signal with process and measurement noise in Fig. A-2 is processed by the Kalman filter and the smoothing algorithm and the results are shown in Fig. A-3. Note that identical process and measurement covariances are used for both filters, and initial state estimates and initial process error covariance matrices are chosen to be identically zero for convenience. Because both filters incorporate model information including the resonance properties of the system that generated the image, the characteristic oscillations can be eliminated. The lightly-damped bending mode is removed from the response, and the topographical information is faithfully reproduced. Importantly, we note the smoothing filter's improvement over the standard Kalman filter. Due to the two-pass nature of the algorithm (the forward sweep and the backward sweep), additional minimization of noise is achieved. In fact, the minimal amount of noise in the smoothing filter's response allows for the characterization of small amplitude signals repre-

sentative of surface roughness properties, a task more difficult with the noise content in the Kalman filter response as will be demonstrated later in this section.
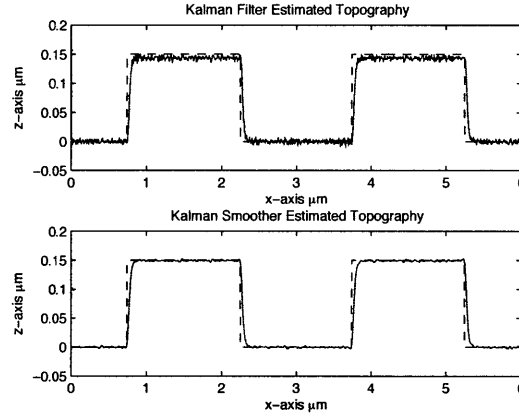

Figure A-3: Simulated AFM topographical data from Fig. A-2 is processed by a standard causal Kalman filter (top) and the acausal smoothing algorithm (bottom). While both algorithms eliminate the oscillations associated with the piezo tube bending mode, the two-pass smoothing algorithm decreases the noise more, which allows for surface roughness studies. Note that identical noise and measurement covariances were used in the two experiments.

In order to compare the proposed method to alternate filtering techniques, a standard notch filter is applied to the same source data from Fig. A-2. The filter must be designed with a bandstop at the resonance frequency to eliminate oscillations in the image. A 100th order FIR filter is applied to the simulated AFM response and the results are shown in Fig. A-4 (with the smoothing filter also shown for comparison).[1]

While the ringing has been eliminated, the resulting signal remains noisy, which obscures characterization of the underlying surface properties. We note that because no model is used in the notch filter, important signal information with the frequency content in the stopband has also been eliminated, making the notch filter somewhat indiscriminate in the parts of the signal it discards. Additionally, the stopband in the notch filter is manually tuned here to match the oscillations of the unprocessed AFM signal, however, it is well known that the resonance properties of an AFM vary greatly from scan to scan and would require that the notch filter be manually tuned each time new data is obtained. Therefore,

---

[1] An FIR filter is chosen for comparison due to its linear phase properties. Preservation of the waveform of the signal is important for correctly representing the topography. The frequency of the notch is selected to remove the mode associated with the large amplitude ringing of Fig. A-2
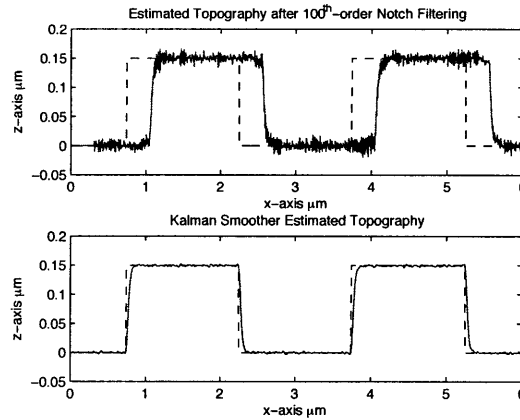
Figure A-4: Simulated AFM topographical information is processed by a notch filter with bandstop centered at the bending mode resonance (top) and by the Kalman smoothing algorithm for comparison (bottom). The shift in the notch filter-processed signal is due to group delay of the FIR filter.

the notch filter should not be considered robust to parameter variation.
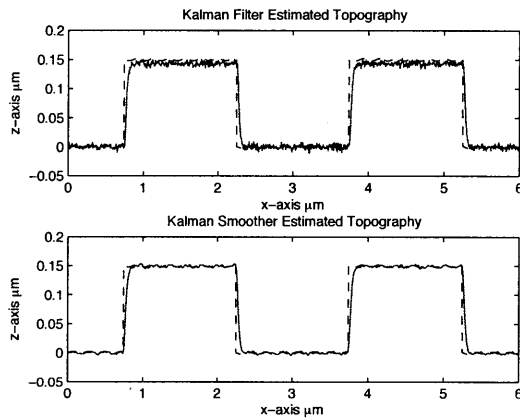
Figure A-5: A topographic sample with surface roughness is processed by the standard Kalman filter (top) and the smoothing algorithm (bottom). Due to the decreased noise in the results of the smoothing algorithm, low amplitude surface roughness properties can be observed.

As previously mentioned, AFMs are frequently used for surface characterization studies, and small amplitude signals often contain the most useful information. Experimental results are presented here recreate a silicon grating with surface roughness by adding a low amplitude sinusoid to the topography. The additional signal is designed to occur at the same spatial frequency as the underdamped piezo bending mode, making retention of this

information difficult. This new signal is processed by the standard Kalman filter and the acausal smoothing algorithm, and the results are shown in Fig. A-5. The smoothing algorithm removes more of the noise content allowing identification of the underlying periodic surface roughness, despite occurring at the same frequency of the rejected oscillations—this type of selective disturbance rejection is facilitated by a model-based filter and not possible with a simple notch filter.

It is important to note that because the results presented here originate from a simulation, we have access to the process and measurement noise covariances. However, when the smoothing filter is applied to real AFM data, model uncertainty becomes a larger contributor and must be reflected in the the process error covariance matrix. These considerations are taken into account in the next section, which evaluated the acausal Kalman smoother on experimental AFM data taken at a high scan rate.

A.4   Experimental Results and Discussion

In order to tolerate ringing induced by high speed AFM operation, data is collected from an AFM scanning a square periodic silicon grating and operated with a 3 Hz line scan rate, which is sufficient to induce ringing for this particular sample, and then processed by the acausal Kalman smoother. Sensor and process covariance matrices required for Kalman filtering are determined by examining the sensor noise output for constant cantilever deflection, and scaling the process covariance to reflect model uncertainty.

Silicon gratings are used to match the simulated results of the previous section and provide step inputs to the AFM piezo scanner. The AFM is operated at a linear scan speed of 36 $\mu m/s$ and tuned PID gains and ringing in the topography signal is observed near large changes in amplitude (the ringing is not present when imaged at 24 $\mu m/s$). This signal is filtered by the acausal Kalman filter and results are shown for two representative traces in Fig. A-6 (note that the unfiltered signal is shifted from the smoothed signal for clarity). The Kalman filter successfully removes oscillatory artifacts from the images and allows data to be obtained at a higher rate.

In order to begin processing, the algorithm requires initial estimates of the state and
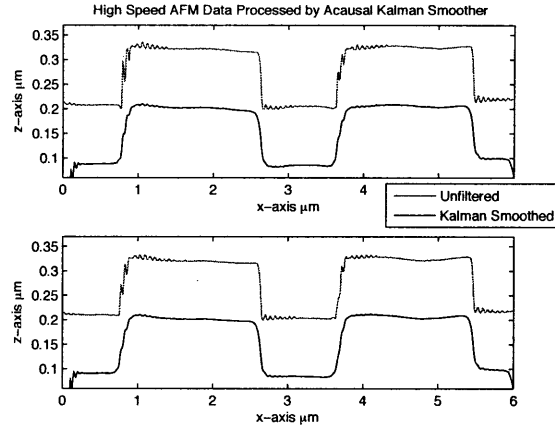
Figure A-6: Data collected from an AFM operated at 36 $\mu m/s$ is filtered by an acausal Kalman smoother and compared to the original (unfiltered) data. Excessive oscillation associated with underdamped poles in the piezo tube actuator introduce image artifacts when the AFM is operated too quickly. This ringing can be removed by an acausal Kalman filter and underlying topography is revealed, permitting higher speed operation of the AFM. The convenient choice of zero-valued initial conditions for the state estimate $\hat{x}_0^-$ lead to incorrect estimates for the first few data points, but the filter quickly converges and a more appropriate initial condition can be selected in future implementations.

its error covariance matrix. For convenience, these values are set to zero, and account for the deviation of the first few samples of the Kalman smoothed signal in Fig. A-6, and quickly converge to the topography. A more appropriate initial value could be used in future refinements perhaps using the data from the previous scanline.

While the filter removes dominant oscillation from the trace, residual noise is apparent. This may be eliminated with further tuning of the filter gains or with the use of a higher order model. In fact, automation of the algorithm could be achieved in conjunction with a system identification approach that identifies an appropriate model for use in the Kalman filter based on the current scan conditions [34] (as mentioned earlier, interaction forces and therefore system dynamics depend on AFM operating conditions such as cantilever setpoint, scan speed and sample stiffness). This identified model could be incorporated into the Kalman filter and applied to the data after image acquisition as part of the common AFM post-processing operations (*e.g.,* tilt and smudge removal). This approach is suitable and could permit high speed operation of the AFM provided that substantial tip-sample separation (liftoff) does not occur.

The quality of the image obtained by scanning at 36 $\mu m/s$ and processed by the acausal Kalman filter is comparable to that obtained at more conservative speeds (the algorithm was observed to break down and substantially higher scan speeds, perhaps due to data corruption from unmodeled dynamics). This algorithm permits faster-than-normal operation of the microscope without sacrificing image fidelity, and further may be accomplished with knowledge of a few system parameters that can be determined online via system identification algorithms, and does not require extensive tuning and indiscriminate data removal characteristic of notch filters.

Appendix B

Filter Preparation Example

The following describes the procedure used to convert a continuous time model of the scanner to a controller in the form suitable for implementation on the FPGA described in Section 4.2. The compensator is designed as per Section 4.4, yielding a continuous time transfer function of order 6 or less.

As an example, assume the plant is identified to have a resonance frequency at $f = 1000\ Hz$ and a damping parameter of $\zeta = 0.05$. The model transfer function is then given by

$$P(s) = \frac{3.948e007}{s^2 + 628.3s + 3.948e007}.$$ (B.1)

The continuous time desired controller is found from model inversion with the addition of rolloff. For this example, the desired controller is

$$G_1(s) = \frac{2.494e016s^2 + 1.567e019s + 9.845e023}{3.948e007s^4 + 1.984e012s^3 + 3.741e016s^2 + 3.134e020s + 9.845e023}$$ (B.2)

where the complex zeros in the numerator match the poles of $P(s)$ with an additional requirement that $G_1(s)$ be made with a DC gain of unity.

The next step requires converting the continuous time domain controller into discrete

time using a bilinear transformation. The resulting difference equation is

$$G_1(z^{-1}) = \frac{0.0034947 + 0.0000144z^{-1} - 0.0069716z^{-2} - 0.000075z^{-3} + 0.0034838z^{-4}}{1.0000 - 3.7563z^{-1} + 5.2912z^{-2} - 3.3126z^{-3} + 0.7777z^{-4}}$$

(B.3)

As described in Section 4.2, direct implementation of this difference equation would result in loss of precision due to the finite memory storage capability of FPGA systems. A more preferred approach requires factoring Equation (B.3) into second order sections into the general form:

$$G(z^{-1}) = K \prod_{j=1}^{3} 2^{g_j} \frac{b_{0j} + b_{1j}z^{-1} + b_{2j}z^{-2}}{1 + a_{1j}z^{-1} + a_{2j}z^{-2}}$$

(B.4)

which, for this example, results in the equation

$$G_1(z^{-1}) = 0.2236 \left(2^{-5} \frac{1 + 2z^{-1} + 1z^{-2}}{1 - 1.8779z^{-1} + 0.8817z^{-2}} \right) \left(2^{-1} \frac{1 + 2z^{-1} + 1z^{-2}}{1 - 1.8784z^{-1} + 0.8821z^{-2}} \right)$$

(B.5)

Note that this factoring can be done multiple ways and there are extra parameters than strictly necessary when expressed in the form of Equation (B.3). This additional freedom is used to enforce additional constraints on the resulting equation. For example, the numerator is selected to be constrained to integers to reduce the memory storage requirements and simplify multiplication operations (multiplication by 1 is trivial, and multiplication by 2 is simply a fast bit shift operation). The denominator is chosen to arrange the poles such the overall filter has minimum L_2 norm.

Bibliography

[1] S. Akamine, R. C. Barrett, and C. F. Quate. Improved atomic force microscope images using microcantilevers with sharp tips. *Applied Physics Letters*, 57(3):316–318, 1990. 1.1.3, 3.1

[2] T. Akiyama, S. Gautsch, N. de Rooij, U. Staufer, P. Niedermann, L. Howald, D. Muller, A. Tonin, H. Hidber, W. Pike, and M. Hecht. Atomic force microscope for planetary applications. *Sensors And Actuators A-Physical*, 91(3):321–325, JUL 15 2001. Solid-State Sensors and Actuators Workshop, Jun 04-08, 2000. 1.1.3

[3] T. R. Albrecht and C. F. Quate. Atomic resolution with the atomic force microscope on conductors and nonconductors. *Journal Of Vacuum Science & Technology A-Vacuum Surfaces And Films*, 6(2):271–274, 1988. 1.1.3, 3.1

[4] T. Ando, N. Kodera, Y. Naito, T. Kinoshita, K. Furuta, and Y. Y. Toyoshima. A high-speed atomic force microscope for studying biological macromolecules in action. *ChemPhysChem*, 4(11):1196–1202, Nov 2003. 1.2, 1.3, 1, 5.1.1

[5] T. Ando, N. Kodera, E. Takai, D. Maruyama, K. Saito, and A. Toda. A high-speed atomic force microscope for studying biological macromolecules. *Proceedings of the National Academy of Sciences of the United States of America*, 98(22):12468–12472, Oct 2001. 1.2, 1-2, 1.3, 3.1, 4.1, A.1

[6] T. Ando, T. Uchihashi, and T. Fukuma. High-Speed Atomic Force Microscopy For Nano-Visualization Of Dynamic Biomolecular Processes. *Progress In Surface Science*, 83(7-9):337–437, Nov 2008. 2.1.1

[7] T. Ando, T. Uchihashi, N. Kodera, A. Miyagi, R. Nakakita, H. Yamashita, and M. Sakashita. High-speed atomic force microscopy for studying the dynamic behavior of protein molecules at work. *Japanese Journal of Applied Physics Part 1-Regular Papers, Brief Communications, Review Papers*, 45(3B):1897–1903, Mar 2006. 1.2, 1

[8] T. Ando, T. Uchihashi, N. Kodera, D. Yamamoto, M. Taniguchi, A. Miyagi, and H. Yamashita. High-speed atomic force microscopy for observing dynamic biomolecular processes. *Journal of Molecular Recognition*, 20(6):448–458, Nov-Dec 2007. 1

[9] G. Binnig, C. F. Quate, and C. Gerber. Atomic Force Microscope. *Physical Review Letters*, 56(9):930–933, 1986. 1.1.1, 4.1

[10] G. Binning, H. Rohrer, C. Gerber, and E. Weibel. Surface studies by scanning tunneling microscopy. *Physical Review Letters*, 49(1):57–61, Jul 1982. 1.1.1

[11] R. G. Brown and P. Y. C. Hwang. *Introduction to Random Signals and Applied Kalman Filtering*. Wiley, New York, 3rd edition, 1997. A.2, A.2

[12] J. Brugger, N. Blanc, P. Renaud, and N. F. Derooij. Microlever with combined integrated sensor actuator functions for scanning force microscopy. *Sensors And Actuators A-Physical*, 43(1-3):339–345, 1994. 3.1, 3.1

[13] D. J. Burns. *On Single-Molecule DNA Sequencing with Atomic Force Microscopy using Functionalized Carbon Nanotube Probes*. Master's thesis, Massachusetts Institute of Technology, 2004. 4.1

[14] D. J. Burns, G. E. Fantner, A. M. Belcher, I. W. Rangelow, and K. Youcef-Toumi. In Depth Characterization and Control of AFM Cantilevers With Integrated Sensing and Actuation. *Journal of Dynamic Systems, Measurement, and Control*, 131(6):061104, Nov 2009. 2.2.3

[15] D. J. Burns, V. Shilpiekandula, B. D. Aumond, and K. Youcef-Toumi. Keynote Presentation: On Imaging at the Nanoscale. In *5th International Workshop on Signal Processing and its Applications*, 2008. A

[16] D. J. Burns, V. Shilpiekandula, S. G. Li, Z. G. Xu, S. F. Yoon, H. K. Taylor, and K. Youcef-Toumi. Fusion of Metrology Data for Large-Scale High-Volume Manufacturing of Polymer-Based Microfluidic Devices. *International Journal of Nanomanufacturing*, 3(4):312–336, 2009. 2.1.1, 6.3.3

[17] D. J. Burns and K. Youcef-Toumi. Shortening carbon nanotube-tipped afm probes. In *4th International Symposium on Nanomanufacturing*, 2006. 1.2, 4.1

[18] D. J. Burns and K. Youcef-Toumi. Measuring, shortening and functionalizing carbon nanotube tipped afm probes for dna sequencing. In *7th Singapore-MIT Alliance Annual Symposium*, 2007. 1.2, 4.1

[19] H. Butt, P. Siedle, K. Seifert, K. Fendler, T. Seeger, E. Bamberg, A. Weisenhorn, K. Goldie, and A. Engel. Scan Speed Limit In Atomic Force Microscopy. *Journal of Microscopy-Oxford*, 169(Part 1):75–84, Jan 1993. 3

[20] H. J. Butt and M. Jaschke. Calculation of thermal noise in atomic force microscopy. *Nanotechnology*, 6(1):1–7, 1995. 2.1

[21] G. M. Clayton and S. Devasia. Conditions for Image-Based Identification of SPM-Nanopositioner Dynamics. *IEEE-ASME Transactions On Mechatronics*, 14(4):405–413, Aug 2009. 4.3.2

[22] G. M. Clayton, S. Tien, K. K. Leang, Q. Z. Zou, and S. Devasia. A Review of Feedforward Control Approaches in Nanopositioning for High-Speed SPM. *Journal of Dynamic Systems, Measurement, and Control*, 131(6):061101, Nov 2009. 1.2, 4.1, 4.1, 4.4.1, 4.5

[23] T. Corman, K. Noren, P. Enoksson, J. Melin, and G. Stemme. "Burst" Technology with Feedback-Loop Control for Capacitive Detection and Electrostatic Excitation. *Electron Devices*, Jan 2000. 3.3.3, 3.5

[24] D. Croft and S. Devasia. Vibration Compensation For High Speed Scanning Tunneling Microscopy. *Review of Scientific Instruments*, 70(12):4600–4605, Dec 1999. 4.1

[25] S. Devasia. Should model-based inverse inputs be used as feedforward under plant uncertainty? *IEEE Transactions On Automatic Control*, 47(11):1865–1871, Nov 2002. 4.1, 4.4.1, 4.6.1

[26] S. Devasia, D. G. Chen, and B. Paden. Nonlinear Inversion-Based Output Tracking. *IEEE Transactions On Automatic Control*, 41(7):930–942, Jul 1996. 4.1

[27] S. Devasia, E. Eleftheriou, and S. Moheimani. A survey of control issues in nanopositioning. *Control Systems Technology, IEEE Transactions on*, 15(5):802–823, Sept. 2007. 3.4.3

[28] M. Dirckx, A. D. Mazzeo, and D. E. Hardt. Production of micro-molding tooling by hot embossing. In *Proceedings Of The Asme International Conference On Manufacturing Science And Engineering - 2007*, pages 141–149, 2007. ASME International Conference on Manufacturing Science and Engineering, Atlanta, GA, OCT 15-18, 2007. 6.3.3

[29] K. El Rifai, O. El Rifai, and K. Youcef-Toumi. On robust adaptive switched control. In *Proceedings of the 2005 American Control Conference*, pages 18–23 vol. 1, 2005. 4.1, 4.4.1

[30] O. El Rifai and K. Youcef-Toumi. Dynamics of contact-mode atomic force microscopes. In *Proceedings of the 2000 American Control Conference.*, volume 3, pages 2118–2122 vol3, 2000. 4.1, A.1, A.2, A.2

[31] O. M. El Rifai. *Modeling and Control of Undesirable Dynamics in Atomic Force Microscopes*. PhD thesis, Massachusetts Institute of Technology, 2002. 4.1

[32] O. M. El Rifai and K. Youcef-Toumi. Coupling in piezoelectric tube scanners used in scanning probe microscopes. In *Proceedings of the 2001 American Control Conference*, volume 4, pages 3251–3255 vol.4, 2001. 4.3.1, A.2, A.2

[33] O. M. El Rifai and K. Youcef-Toumi. Design and control of atomic force microscopes. In *Proceedings of the 2003 American Control Conference*, volume 5, pages 3714–3719 vol.5, 2003. A.1, A.2, A.2

[34] O. M. El Rifai and K. Youcef-Toumi. On automating atomic force microscopes: an adaptive control approach. In *43rd IEEE Conference on Decision and Control*, volume 2, pages 1574–1579 Vol.2, 2004. A.4

[35] Y. Fang, T. Spisz, T. Wiltshire, N. D'Costa, I. Bankman, R. Reeves, and J. Hoh. Solid-state dna sizing by atomic force microscopy. *Analytical Chemistry*, 70(10):2123–2129, 1998. 1.2

[36] G. E. Fantner, R. J. Barbero, D. S. Gray, and A. M. Belcher. Kinetics Of Antimicrobial Peptide Activity Measured On Individual Bacterial Cells Using High-Speed Atomic Force Microscopy. *Nature Nanotechnology*, advance online publication, 03 2010. 1.2, 4.1

[37] G. E. Fantner, P. Hegarty, J. H. Kindt, G. Schitter, G. A. G. Cidade, and P. K. Hansma. Data acquisition system for high speed atomic force microscopy. *Review of Scientific Instruments*, 76(2):026118, 2005. 1.3, 5, 5.1.2

[38] G. E. Fantner, G. Schitter, J. H. Kindt, T. Ivanov, K. Ivanova, R. Patel, N. Holten-Andersen, J. Adams, P. J. Thurner, I. W. Rangelow, and P. Hansma. Components For High Speed Atomic Force Microscopy. *Ultramicroscopy*, 106(8-9):881–887, 2006. 1.3, 2-2, 2.1.2, 3.1, 4.3.1, 5, 5.1.2

[39] G. E. Fantner, W. Schumann, R. J. Barbero, A. Deutschinger, V. Todorov, D. S. Gray, A. M. Belcher, I. W. Rangelow, and K. Youcef-Toumi. Use of self-actuating and self-sensing cantilevers for imaging biological samples in fluid. *Nanotechnology*, 20(43):434003, 2009. 6, 6.2.1

[40] V. Ferrari, A. Ghisla, D. Marioli, and A. Taroni. Silicon resonant accelerometer with electronic compensation of input-output cross-talk. *Sensors & Actuators: A. Physical*, Jan 2005. 3.3.3, 3.5

[41] R. P. Feynman. *The Feynman Lectures on Physics*, volume 1. Addison Wesley, 1963. 3

[42] M. Fritz, M. Radmacher, J. P. Cleveland, M. W. Allersma, R. J. Stewart, R. Giesel-
     mann, P. Janmey, C. F. Schmidt, and P. K. Hansma. Imaging globular and filamentous
     proteins in physiological buffer solutions with tapping mode atomic-force microscopy.
     Langmuir, 11(9):3529–3535, 1995. 1.1.3

[43] S. Gautsch, T. Akiyama, R. Imer, N. de Rooij, U. Staufer, P. Niedermann, L. Howald,
     D. Brandlin, A. Tonin, H. Hidber, and W. Pike. Measurement Of Quartz Particles
     By Means Of An Atomic Force Microscope For Planetary Exploration. *Surface And
     Interface Analysis*, 33(2):163–167, FEB 2002. SXM 4 Conference, Munster, Germany,
     2000. 1.1.3

[44] S. Gautsch, U. Staufer, T. Akiyama, H. Hidber, A. Tonin, L. Howald, D. Muller,
     P. Niedermann, and N. de Rooij. Miniaturized Atomic Force Microscope for Planetary
     Exploration. In Harris, RA, editor, *9th European Space Mechanisms And Tribology
     Symposium*, volume 480 of *ESA Special Publications*, pages 11–16, 2001. 9th European
     Space Mechanisms and Tribology Symposium, Sep 19-21, 2001. 1.1.3

[45] J. H. Hafner, C. L. Cheung, A. T. Woolley, and C. M. Lieber. Structural and func-
     tional imaging with carbon nanotube afm probes. *Progress in Biophysics & Molecular
     Biology*, 77(1):73–110, 2001. 4.1

[46] P. K. Hansma, G. Schitter, G. E. Fantner, and C. Prater. Applied physics: High-speed
     atomic force microscopy. *Science*, 314(5799):601–602, 2006. 1.3, 5

[47] R. Hillenbrand, M. Stark, and R. Guckenberger. Higher-Harmonics Generation In
     Tapping-Mode Atomic-Force Microscopy: Insights Into The Tip-Sample Interaction.
     Applied Physics Letters, 76(23):3478–3480, Jun 5 2000. 2.2.3

[48] A. C. Hillier and A. J. Bard. AC-Mode Atomic Force Microscope Imaging in Air and
     Solutions with a Thermally Driven Bimetallic Cantilever Probe. *Review of Scientific
     Instruments*, 68(5):2082–2090, May 1997. 3.1

[49] A. D. L. Humphris, M. J. Miles, and J. K. Hobbs. A mechanical microscope: High-
     speed atomic force microscopy. *Applied Physics Letters*, 86(3):034106, 2005. 1-2, 1.3,
     2.1.1, 3

[50] T. Ivanov, T. Gotszalk, P. Grabiec, E. Tomerov, and I. Rangelow. Thermally driven micromechanical beam with piezoresistive deflection readout. *Microelectronic Engineering*, 67-8:550–556, Jun 2003. 3.1, 3.1, 3.2, 3.3.3

[51] T. Ivanov, T. Gotszalk, T. Sulzbach, I. Chakarov, and I. W. Rangelow. AFM cantilever with ultra-thin transistor-channel piezoresistor: quantum confinement. *Microelectronic Engineering*, 67-8:534–541, Jun 2003. 3.1

[52] S. Kasas, N. Thomson, B. Smith, H. Hansma, X. Zhu, M. Guthold, C. Bustamante, E. Kool, M. Kashlev, and P. Hansma. Escherichia coli rna polymerase activity observed using atomic force microscopy. *Biochemistry*, 36(3):461–468, 1997. 1.2

[53] J. H. Kindt, G. E. Fantner, J. A. Cutroni, and P. K. Hansma. Rigid design of fast scanning probe microscopes using finite element analysis. *Ultramicroscopy*, 100(3-4):259–265, Aug 2004. 1.3, 3.1, 4.4.2, 5

[54] M. Kobayashi and R. Horowitz. Track seek control for hard disk dual-stage servo systems. *IEEE Transactions On Magnetics*, 37(2, Part 1):949–954, Mar 2001. 3.4.3

[55] N. Kodera, T. Kinoshita, T. Ito, and T. Ando. High-resolution imaging of myosin motor in action by a high-speed atomic force microscope. In *Advances in Experimental Medicine and Biology*, volume 538, pages 119–127, 2003. 1.3

[56] N. Kodera, Y. Naito, A. Miyagi, T. Ando, H. Sakakibara, and K. Ooiwa. Dynamic behavior of motor proteins in action captured by high-speed atomic force microscope. *Biophysical Journal*, 86(1):154A–154A, Jan 2004. 1, 5.1.1

[57] N. Kodera, H. Yamashita, and T. Ando. Active damping of the scanner for high-speed atomic force microscopy. *Review of Scientific Instruments*, 76(5):053708, May 2005. 1.3

[58] J. Kokavecz, O. Marti, P. Heszler, and A. Mechler. Imaging bandwidth of the tapping mode atomic force microscope probe. *Physical Review B (Condensed Matter and Materials Physics)*, 73(15):155403, 2006. 2.2.2

[59] R. Lal and S. A. John. Biological Applications Of Atomic-Force Microscopy. *American Journal Of Physiology*, 266(1):C1, Jan 1994. 4.1

[60] P. P. Lehenkari, G. T. Charras, A. Nykanen, and M. A. Horton. Adapting Atomic Force Microscopy For Cell Biology. *Ultramicroscopy*, 82(1-4):289–295, Feb 2000. 4.1

[61] S. Li, Z. Xu, A. Mazzeo, D. J. Burns, G. Fu, M. Dirckx, V. Shilpiekandula, X. Chen, N. C. Nayak, E. Wong, S. F. Yoon, Z. P. Fang, K. Youcef-Toumi, D. Hardt, S. B. Tor, C. Y. Yue, and J.-H. Chun. Review Of Production Of Microfluidic Devices: Material, Manufacturing And Metrology - Art. No. 69930F. In Urey, H, editor, *MEMS, MOEMS, and Micromaching III*, volume 6993 of *Proceedings Of The Society Of Photo-Optical Instrumentation Engineers (SPIE)*, page F9930, 2008. Conference on MEMS, MOEMS and Micromachining III, Strasbourg, Apr, 2008. 6.3.3

[62] J. A. S. Lima and A. R. Plastino. On the classical energy equipartition theorem. *Brazilian Journal of Physics*, 30(1):176–180, 2000. 2.1.2

[63] H. Lin, D. O. Clegg, and R. Lal. Imaging real-time proteolysis of single collagen I molecules with an atomic force microscope. *Biochemistry*, 38(31):9956–9963, Aug 1999. 4.1

[64] R. Linnemann, T. Gotszalk, L. Hadjiiski, and I. W. Rangelow. Characterization of a cantilever with an integrated deflection sensor. *Thin Solid Films*, 264(2):159–164, Aug 1995. 3.1

[65] L. Ljung. *System Identification: Theory for the User*. Prentice Hall, 1999. 3.4.1, 4.3.1, 4.3.2

[66] J. Malo and J. I. Izpura. Simultaneous magnetic and electrostatic driving of micro-cantilevers. *Sensors And Actuators A-Physical*, 136(1):347–357, 2007. 3.1

[67] S. R. Manalis, S. C. Minne, and C. F. Quate. Atomic force microscopy for high speed imaging using cantilevers with an integrated actuator and sensor. *Applied Physics Letters*, 68(6):871–873, 1996. 1.3, 3.1, 3.1

[68] O. Marti, B. Drake, and P. K. Hansma. Atomic force microscopy of liquid-covered surfaces - atomic resolution images. *Applied Physics Letters*, 51(7):484–486, 1987. 1.1.3

[69] O. Marti, A. Ruf, M. Hipp, H. Bielefeldt, J. Colchero, and J. Mlynek. Mechanical and thermal effects of laser irradiation on force microscope cantilevers. *Ultramicroscopy*, 42:345–350, 1992. 3.1

[70] Y. Martin, D. W. Abraham, and H. K. Wickramasinghe. High-resolution capacitance measurement and potentiometry by force microscopy. *Applied Physics Letters*, 52(13):1103–1105, 1988. 1.1.3

[71] N. F. Martinez, J. R. Lozano, E. T. Herruzo, F. Garcia, C. Richter, T. Sulzbach, and R. Garcia. Bimodal atomic force microscopy imaging of isolated antibodies in air and liquids. *Nanotechnology*, 19(38):384011 (8pp), 2008. 2.1.1

[72] J. Mertz, O. Marti, and J. Mlynek. Regulation of a microcantilever response by force feedback. *Applied Physics Letters*, 62(19):2344–2346, 1993. 2.2.2

[73] S. C. Minne, S. R. Manalis, and C. F. Quate. Parallel atomic force microscopy using cantilevers with integrated piezoresistive sensors and integrated piezoelectric actuators. *Applied Physics Letters*, 67(26):3918–3920, 1995. 1.1.3, 1.2, 3.1, 3.1

[74] S. C. Minne, G. Yaralioglu, S. R. Manalis, J. D. Adams, J. Zesch, A. Atalar, and C. F. Quate. Automated parallel high-speed atomic force microscopy. *Applied Physics Letters*, 72(18):2340–2342, 1998. 1.1.3

[75] J. N. Newman. *Marine Hydrodynamics*. MIT Press, 1977. 2.1.1

[76] A. Noy, D. V. Vezenov, and C. M. Lieber. Chemical force microscopy. *Annual Review of Materials Science*, 27:381–421, 1997. 4.1

[77] A. V. Oppenheim, R. W. Schafer, and J. R. Buck. *Discrete-time signal processing.* Prentice Hall, Upper Saddle River, N.J., 2nd ed edition, 1999. 4.2

[78] R. Pedrak, T. Ivanov, K. Ivanova, T. Gotszalk, N. Abedinov, I. Rangelow, K. Edinger, E. Tomerov, T. Schenkel, and P. Hudek. Micromachined Atomic Force Microscopy Sensor with Integrated Piezoresistive, Sensor and Thermal Bimorph Actuator for High-Speed Tapping-Mode Atomic Force Microscopy Phase-Imaging in Higher Eigenmodes. *Journal Of Vacuum Science & Technology B*, 21(6):3102–3107, Nov-Dec 2003. 3.1, 3.1, 3.2

[79] A. Persaud, K. Ivanova, Y. Sarov, T. Ivanov, B. E. Volland, I. W. Rangelow, N. Nikolov, T. Schenkel, V. Djakov, D. W. K. Jenkins, J. Meijer, and T. Vogel. Micromachined piezoresistive proximal probe with integrated bimorph actuator for aligned single ion implantation. *Journal of Vacuum Science & Technology B: Microelectronics and Nanometer Structures*, 24(6):3148–3151, Nov-Dec 2006. 3.1

[80] M. A. Poggi, L. A. Bottomley, and P. T. Lillehei. Scanning probe microscopy. *Analytical Chemistry*, 74(12):2851–2862, 2002. 4.1

[81] A. Quist, I. Doudevski, H. Lin, R. Azimova, D. Ng, B. Frangione, B. Kagan, J. Ghiso, and R. Lal. Amyloid ion channels: A common structural link for protein-misfolding disease. *PNAS*, 102(30):10427–10432, 2005. 1.2

[82] J. Rissanen. Stochastic complexity and modeling. *The Annals of Statistics*, 14:1080–1100, 1986. 3.4.1

[83] A. Ruf, M. Abraham, J. Diebel, W. Ehrfeld, P. Guthner, M. Lacher, K. Mayr, and J. Reinhardt. Integrated fabry-perot distance control for atomic force microscopy. *Journal Of Vacuum Science & Technology B*, 15(3):579–585, 1997. 3.1

[84] O. Sahin. Time-varying tip-sample force measurements and steady-state dynamics in tapping-mode atomic force microscopy. *Physical Review B*, 77(11), MAR 2008. 2.2.3

[85] O. Sahin and N. Erina. High-resolution and large dynamic range nanomechanical mapping in tapping-mode atomic force microscopy. *Nanotechnology*, 19(44), NOV 5 2008. 2.2.3

[86] O. Sahin, G. Yaralioglu, R. Grow, S. Zappe, A. Atalar, C. Quate, and O. Solgaard. High-Resolution Imaging Of Elastic Properties Using Harmonic Cantilevers. *Sensors And Actuators A-Physical*, 114(2-3):183–190, SEP 1 2004. 12th International Conference on Solid-State Sensors, Actuators and Microsystems (Transducers 03), Boston, MA, Jun 08-12, 2003. 2.2.3

[87] G. Schitter, G. E. Fantner, J. H. Kindt, P. J. Thurner, and P. K. Hansma. On recent developments for high-speed atomic force microscopy. In *Proceedings of the 2005 IEEE/ASME International Conference on Advanced Intelligent Mechatronics*, pages 261–264, 2005. 1.3, 5

[88] G. Schitter, G. E. Fantner, P. J. Thurner, J. Adams, and P. K. Hansma. Design and characterization of a novel scanner for high-speed atomic force microscopy. In *4th IFAC-Symposium on Mechatronic Systems*, pages 819–824, 2006. 5.1.1

[89] G. Schitter, R. W. Stark, and A. Stemmer. Fast contact-mode atomic force microscopy on biological specimen by model-based control. *Ultramicroscopy*, 100(3-4):253–257, 2004. 3.1

[90] G. Schitter and A. Stemmer. Identification and open-loop tracking control of a piezoelectric tube scanner for high-speed scanning-probe microscopy. *Control Systems Technology, IEEE Transactions on*, 12(3):449–454, 2004. 4.1

[91] G. Schitter, A. Stemmer, and F. Allgower. Robust 2 dof-control of a piezoelectric tube scanner for high speed atomic force microscopy. In *Proceedings of the 2003 American Control Conference*, volume 5, pages 3720–3725 vol.5, 2003. 4.1, 4.4.1, 4.5

[92] G. Shmalz. *Uber Glatte und Ebenheit als Physikalisches und Physiologishes Problem*. Verein Deutscher Ingenieure, Oct 1929. 1.1.1

[93] T. Sulchek, G. G. Yaralioglu, C. F. Quate, and S. C. Minne. Characterization and optimization of scan speed for tapping-mode atomic force microscopy. *Review of Scientific Instruments*, 73(8):2928–2936, Aug 2002. 2.2.2, 2.2.2, 2.2.3, 3.1

[94] K. O. Vanderwerf, C. A. J. Putman, B. G. Degrooth, and J. Greve. Adhesion force imaging in air and liquid by adhesion mode atomic-force microscopy. *Applied Physics Letters*, 65(9):1195–1197, Aug 1994. 1.1.3

[95] P. Vettiger, M. Despont, U. Drechsler, U. Durig, W. Haberle, M. Lutwyche, H. Rothuizen, R. Stutz, R. Widmer, and G. Binnig. The "millipede"—more than one thousand tips for future afm data storage. *IBM Journal of Research and Development*, 44(3):323–40, 2000. 1.1.3

[96] M. B. Viani, L. I. Pietrasanta, J. B. Thompson, A. Chand, I. C. Gebeshuber, J. H. Kindt, M. Richter, H. G. Hansma, and P. K. Hansma. Probing protein-protein interactions in real time. *Nature Structural Biology*, 7(8):644–647, Aug 2000. 1.2, 4.1, A.1

[97] M. B. Viani, T. E. Schaffer, A. Chand, M. Rief, H. E. Gaub, and P. K. Hansma. Small Cantilevers For Force Spectroscopy Of Single Molecules. *Journal of Applied Physics*, 86(4):2258–2262, Aug 1999. 2.1.2

[98] Y. Wu and Q. Z. Zou. Robust Inversion-Based 2-DOF Control Design for Output Tracking: Piezoelectric-Actuator Example. *IEEE Transactions On Control Systems Technology*, 17(5):1069–1082, Sep 2009. 4.1, 4.5

[99] X. Xu, C. Carrasco, P. J. de Pablo, J. Gomez-Herrero, and A. Raman. Unmasking Imaging Forces on Soft Biological Samples in Liquids When Using Dynamic Atomic Force Microscopy: A Case Study on Viral Capsids. *Biophys. J.*, 95(5):2520–2528, 2008. 2.1.1

[100] L. Yuan and Q. Jian-Qiang. Higher Harmonics Generation in Tapping Mode Atomic Force Microscope. *Chinese Physics Letters*, 26(10), OCT 2009. 2.2.3

[101] Q. Zou, K. K. Leang, E. Sadoun, M. J. Reed, and S. Devasia. Control issues in high-speed AFM for biological applications: Collagen imaging example. *Asian Journal Of Control*, 6(2):164–178, Jun 2004. 4.1, 4.4.1